# ENGINEERING DEVELOPMENT OF SLURRY BUBBLE COLUMN REACTOR (SBCR) TECHNOLOGY

# Gamma-Ray Densitometry and Radioactive Tracer Studies of Fischer-Tropsch Synthesis in the Alternate Fuels Development Unit (AFDU), LaPorte, Texas

**Topical Report**
**July 31, 2002**

**Prepared for**

**Air Products and Chemicals, Inc.**

**for submission to the**

**U.S. Department of Energy**

**under**

**Cooperative Agreement No.: DE-FC22-95PC95051**

**Prepared by**

**Chemical Reaction Engineering Laboratory**
**Chemical Engineering Department**
**Washington University**
**Saint Louis, MO 63130**

**To Whom It May Concern**

This is to certify that the copyright of my D.Sc. thesis entitled "Churn Turbulent Bubble Columns - Experiments and Modeling" completed at Washington University in St. Louis in May 2002 provides for the following exceptions:

Due to the fact that the thesis was done with support from the U.S. Department of Energy (which is properly acknowledged in the thesis) I agree that the following statement applies:

"This paper was written with the support of the U.S. Department of Energy under Cooperative Agreement No. DE-FC22-95PC95051. The Government reserves for itself and others acting on its behalf a royalty free, nonexclusive, irrevocable, world wide license for governmental purposes to publish, distribute, translate duplicate, exhibit and perform this copyrighted paper."

Moreover, since the work on my thesis was performed in the Chemical Reaction Engineering Laboratory (CREL) of Washington University, I as the author of the thesis, grant the permission to CREL to reproduce it as part or as a whole for either government agencies and/or for the Chemical Reaction Engineering Laboratory (CREL) in form of reports to industrial sponsors addressing (slurry) bubble column hydrodynamics and modeling

Dr. Puneet Gupta
Dated: June 3, 2002

# ENGINEERING DEVELOPMENT OF SLURRY BUBBLE COLUMN REACTOR (SBCR) TECHNOLOGY

**Topical Report**

**Chemical Reaction Engineering Laboratory**
**Cooperative Agreement No.: DE-FC22-95PC95051**

## ABSTRACT

This report summarizes the procedures used and results obtained in determining radial gas holdup profiles, via gamma ray scanning, and in assessing liquid and gas mixing parameters, via radioactive liquid and gas tracers, during Fischer Tropsch synthesis. The objectives of the study were i) to develop a procedure for detection of gas holdup radial profiles in operating reactors and ii) to test the ability of the developed, previously described, engineering models to predict the observed liquid and gas mixing patterns.

It was shown that the current scanning procedures were not precise enough to obtain an accurate estimate of the gas radial holdup profile and an improved protocol for future use was developed. The previously developed physically based model for liquid mixing was adapted to account for liquid withdrawal from the mid section of the column.

The ability of our engineering mixing models for liquid and gas phase to predict both liquid and gas phase tracer response was established and illustrated.

# EXECUTIVE SUMMARY

Determination of liquid and gas flow and mixing as a function of operating conditions is essential for proper interpretation and design of bubble columns. In this report the ability of our engineering models, based on physical principles, to interpret liquid and gas phase tracer data during Fischer Tropsch (FT) synthesis, an important gas-to-liquid conversion process, is described. The success of the models in predicting the measured tracer responses during FT synthesis, at conditions that are vastly different from conditions of liquid phase methanol synthesis for which the models have been previously successfully tested, points out to their general applicability to all churn-turbulent bubble column flows.

Specific knowledge gained from this study includes, but is not limited to, the following:

- Excellent reproducibility is obtained for gas phase tracer runs at given set of operating conditions due to gas injection prior to the sparger which ensures high degree of cross-sectional uniformity. This means that in the future multiple gas tracer tests at a chosen condition are unnecessary. In contrast, due to the point nature of the liquid (catalyst) tracer injection multiple injections are needed to properly assess the liquid tracer response.
- The engineering models developed as part of this contract predict tracer responses without adjustable parameters very well for runs in churn turbulent flow (run 16.7 in this study). Model predictions are less accurate for flows that may not be churn turbulent (run 16.6) which is in line with the fact that the physics incorporated in the models assures churn-turbulent conditions.
- The differences in responses for the catalyst and fine powdered $MnO_3$ tracer injections are minimal indicating the validity of the pseudo homogeneous assumption for the liquid (FT-wax) plus solids (catalyst) phase. In contrast, the responses to injections of coarse $MnO_2$ tracer particles differ dramatically to the responses of the fine catalyst indicating settling of large particles.

- The current procedures used in the field for gamma ray scanning lead to significant uncertainties in the chordal average gas holdup estimates which make quantitative determination of gas holdup radial profiles difficult and highly inaccurate. A protocol for improved scanning that should lead to accurate assessment of the holdup profile is proposed and specified.

This study confirms that the gas-liquid recirculation and mixing model developed by Gupta in our Chemical Reaction Engineering Laboratory (CREL), which was described fully in the previous topical report, does indeed possess the ability to predict tracer responses in FT synthesis and presents a valuable engineering tool.

# TABLE OF CONTENTS

**Section No.** **Page No.**

## List of Tables



## List of Figures

# Nomenclature

| | |
|---|---|
| a | interfacial area, $cm^{-1}$ |
| C | concentration, moles/$cm^3$ |
| $C_D$ | drag coefficient |
| $C_{vm}$ | virtual mass coefficient |
| c | parameter in the hold-up profile to allow non-zero hold-up at the wall |
| $D_C$, $D_T$ | column diameter, cm |
| $D_{L,\ m}$ | molecular diffusivity, $cm^2/s$ |
| $D_{Lm,\ Argon}$ | molecular diffusivity of Argon in organic liquids, $cm^2/s$ |
| $\overline{D}_{rr}$ | radial turbulent diffusivity, $cm^2/s$ |
| $\overline{D}_{xx_1}$ | axial turbulent diffusivity of small bubbles and liquid going up, $cm^2/s$ |
| $\overline{D}_{xx_2}$ | axial turbulent diffusivity of small bubbles and liquid going down, $cm^2/s$ |
| $d_b$, $d_{be}$ | mean (effective) bubble diameter, cm |
| $d_{blarge}$ | bubble diameter of large bubbles, cm |
| $d_{vs}$ | Sauter mean bubble diameter, m |
| $E_G$, $E_L$ | gas and liquid axial dispersion coefficient, $cm^2/s$ |
| Eo | Eotvos number |
| Fr | Froude number |
| g | acceleration due to gravity, $cm^2/s$ |
| H | Henry's constant |
| $K_{SB1\text{-}LB}$ | mass exchange coefficient between upflowing "small" and "large" bubble phases, $sec^{-1}$ |
| k | mass transfer coefficient, cm/s |
| I | radiation intensity counts |
| $I_0$ | initial intensity counts |
| L | dispersion height between the end-zone CSTs, cm |
| Lc | characteristic turbulent length, cm |
| l | mixing length, cm |

| | |
|---|---|
| $l_{int}$ | length through the internals, cm |
| Mo | Morton number |
| m | power law exponent in the radial gas hold-up profile |
| n | Richardson-Zaki coefficient |
| P | operating pressure, dyne/cm$^2$ |
| Q | flow rate, cm$^3$/s |
| R | column radius, cm |
| Re | Reynolds number |
| $R_x$ | reaction rate, moles cm$^{-3}$ s$^{-1}$ |
| r | radial position in the column, cm |
| r', r'' | radii where the liquid and gas velocity profiles invert |
| t | time, sec |
| $t_{1/2}$ | half life, hours |
| $U_G$, $U_{G,sup}$ | gas superficial velocity, cm/s |
| $U_{gtrans}$ | transition superficial gas velocity, cm/s |
| $U_L$, $U_{L.sup}$ | liquid superficial velocity, cm/s |
| u | velocity, cm/s |
| $u_{b\infty}$ | terminal single bubble rise velocity, m/s |
| $u_0$ | centerline interstitial liquid velocity, cm/s |
| $\bar{u}$ | radially averaged mean velocity, cm/s |
| $\lvert u_w \rvert$ | absolute value of the interstitial axial liquid velocity near the wall, cm/s |
| $V_a$ | volume of the CST representing the distributor zone, cm$^3$ |
| $V_b$ | volume of the CST representing the disengagement zone, cm$^3$ |
| $V^0_{bsmall}$ | unhindered rise velocity of a small bubble, cm/s |
| $V_{bsmall}$ | rise velocity of dense bubble phase, cm/s |
| $V_{blarge}$ | rise velocity of large bubble phase, cm/s |
| x | axial position in the column, cm |

## Greek Symbols

| | |
|---|---|
| $\varepsilon$ | local phase hold-up |
| $\bar{\varepsilon}$ | radially averaged phase hold-up |
| $\bar{\varepsilon}_{g,chord}$ | chordal average gas holdup |
| $\bar{\varepsilon}_{G,Overall}$ | overall gas holdup |
| $\bar{\varepsilon}_{gtrans}$ | transition gas holdup |
| $\tilde{\varepsilon}_g$ | parameter in the gas holdup profile related to $\bar{\varepsilon}_g$ |
| $\bar{\varepsilon}'_{g1}$ | mean hold-up of up-flowing gas with down-flowing liquid |
| $\mu_i$ | total linear attenuation coefficient of the $i^{th}$ material in the $\gamma$-ray path |
| $\mu_l^m$ | liquid/slurry viscosity, cP |
| $\phi$ | fraction of the column diameter |
| $\rho$ | density, $g/cm^3$ |
| $\sigma$, $\sigma_l$ | surface tension of the liquid, dyne/cm |
| $\tau^m$ | viscous shear stress, $dyne/cm^2$ |
| $\tau^t$ | turbulent shear stress, $dyne/cm^2$ |
| $\nu^m$, $\nu_m$ | kinematic viscosity, $cm^2/s$ |
| $\nu^t$ | turbulent viscosity, $cm^2/s$ |
| $\xi$ | dimensionless radius |
| $\xi'$ | dimensionless radius where the liquid velocity profile inverts |
| $\xi''$ | dimensionless radius where the gas velocity profile inverts |
| $\Delta P$ | pressure drop, $dyne/cm^3$ |

## Subscripts

| | |
|---|---|
| ASE | after slurry exit |
| BSE | before slurry exit |
| b | bubble |

| | |
|---|---|
| bs | small bubble |
| CST | well mixed distributor and disengagement zones, a and b |
| c | contact |
| DP | differential pressure measurement |
| f | column full of liquid |
| g, Gas | gas |
| ga | gas phase in the distributor zone, CST a |
| gb | gas phase in the disengagement zone, CST b |
| g,small | gas in small bubbles |
| g,large | gas in large bubbles |
| g,trans | gas phase at transition |
| g1 | up-flowing gas |
| g2 | down-flowing gas |
| gulu | gas flowing upwards with liquid going up as well |
| guld | gas flowing upwards with liquid going down |
| gdld | gas going down with liquid down as well |
| i | inside |
| in | reactor inlet |
| l, L | liquid |
| la | liquid phase in the distributor zone, CST a |
| lb | liquid phase in the disengagement zone, CST b |
| l1 | up-flowing liquid |
| l2 | down-flowing liquid |
| mt | empty column |
| NDG | nuclear density gauge measurement |
| o | outside |
| out | reactor outlet |
| Slurry | slurry |
| Slurry+Gas | slurry and gas phases |
| tp | column with two-phase flow |

# Gamma-Ray Densitometry and Radioactive Tracer Studies of Fischer-Tropsch Synthesis in the Alternate Fuels Development Unit (AFDU), LaPorte, Texas

With the recent trends and emphasis on employing clean alternate fuels for the automotive industry along with an aggressive search for commercially viable technology to convert abundantly available Natural Gas reserves into desirable value-added chemicals via the Synthesis Gas, the Fischer-Tropsch (FT) synthesis, effected in a slurry bubble column reactor, has emerged as one of the most promising alternatives (Wender, 1996; Sie and Krishna, 1999). As a result, development of a slurry-phase FT process has become of considerable interest to the U.S. Department of Energy (DOE) as part of the Indirect Liquefaction program, which in turn is part of the Coal Liquefaction program sponsored by the Federal Energy Technology Center (FETC). The overall objective of the Coal Liquefaction program is to develop economically competitive and environmentally friendly advanced technology to manufacture synthetic liquid fuels from coal (Bhatt, 1999). In addition, the industrial participants in this program have an interest in developing this technology for remote gas conversion.

Towards this goal, the technology for Fischer-Tropsch (FT) synthesis of desirable hydrocarbons from SynGas (a mixture of hydrogen ($H_2$) and carbon monoxide (CO) gases in a regulated molar ratio) was demonstrated in a pilot-scale slurry bubble-column reactor at the Alternate Fuels Development Unit (AFDU) in LaPorte, Texas (Bhatt, 1999). This study, which was a continuation of earlier studies that had established the "proof-of-concept", was co-sponsored by the U.S. Department of Energy (DOE), Air Products & Chemicals, Inc. (APCI) and Shell Synthetic Fuels, Inc. (SSFI). As mentioned previously, gas holdup and catalyst distributions, as well as liquid and gas backmixing, are the result as well as the cause of many complex hydrodynamic interactions that occur in a slurry bubble-column operation and provide the key information in reactor design for

a given chemistry. Therefore, in addition to providing the much needed pilot-scale data for potential future commercialization of the technology, some additional objectives of the study were to conduct selected experiments in an effort to improve the overall understanding of slurry bubble-column hydrodynamics under reaction conditions. This is the only part of the study that the Chemical Reaction Engineering Laboratory (CREL) was involved with. Towards this effect, gamma-densitometry scans were obtained under actual reaction conditions to non-invasively establish some measure of the radial profiles of gas holdup. In addition, tracer experiments using radioactive liquid, gas and catalyst tracers were conducted to assess the degree of mixing in the three phases respectively. ICI Tracerco, Inc. executed the actual field measurements during these experiments in LaPorte.

The Chemical Reaction Engineering Laboratory (CREL) at Washington University in Saint Louis, Missouri has emerged as one of the primary university-partners in the U.S. Department of Energy's endeavor to continually improve the understanding of slurry bubble column hydrodynamics. A research grant (DE FC22-95 95051) via Air Products and Chemicals, Inc has financially supported CREL efforts which include the analysis of pilot scale tracer and densitometry data from the AFDU. Given the experience with handling such data since 1995, it was a natural choice for CREL to be an active participant in the FT-IV tracer and densitometry studies at the AFDU.

In the first part of this report, results from gamma-densitometry scans are analyzed for reproducibility to assess the reliability of the measured information and suggest improvements for future scanning of pilot-scale reactors at the AFDU. The second half of the report provides the analysis of the radioactive tracer data that includes

- A protocol for processing of the tracer data
- Refinement of the liquid-mixing model (Degaleesan, 1997; Gupta, 2002) to properly account for the slurry exit from the middle portion of the reactor
- Comparison of experimental tracer data with simulation results from gas-liquid mixing models.

# 1. Gamma-Ray Densitometry Studies During FT-IV Runs at the Alternate Fuels Development Unit (AFDU) in LaPorte, Texas

As mentioned earlier, γ-ray scans were performed during the demonstration runs of the slurry phase Fischer-Tropsch technology at the Alternate Fuels Development Unit (AFDU), LaPorte, Texas, to evaluate the technique as a future non-invasive diagnostic for measurement of cross-sectional gas holdup distribution. The following sections provide some theoretical background in analyzing densitometry data. However, the focus is on evaluating the robustness and reliability of the measurement technique, which has been accomplished using statistical analysis of the measured data. Assumptions made in executing the data processing steps have been clearly stated wherever appropriate.

## 1.1. Analysis of Gamma-Scan Data

Prior to the commencement of the study, an experimental matrix of operating conditions was designed such that it would satisfy the requirements of all the involved parties. The ***plan*** included operating the reactor at essentially three different ***inlet*** superficial gas velocity conditions (0.41 ft/sec (12.5 cm/s), 0.62 ft/sec (18.9 cm/s) and 0.72 ft/sec (21.9 cm/s)) with varying ratios of hydrogen and carbon monoxide in the fresh feed gas. The operating pressure for all runs was 710 psig (4.99 MPa). Due to operating constraints, the superficial inlet gas velocity conditions finally employed were 0.41 ft/sec (12.5 cm/s), 0.46-0.48 ft/sec (14.0-14.6 cm/s) and 0.60 ft/sec (18.3 cm/s). To assess the distribution of gas volume fraction in a cross-sectional plane somewhere in the middle of the reactor, where the flow is essentially well-developed, Gamma Densitometry Tomographic (GDT) scans were conducted using a single radioactive source (43 mCi $Co^{60}$) and a 2" NaI (Tl) scintillation detector. Since this was the first time that tomography experiments were being carried out at AFDU in an effort to establish it as a non-invasive tool for monitoring phase distributions, the objectives of the study were modest. Therefore, the scans were executed only at one operating condition (Run AF R16.3B) that corresponded to the highest inlet superficial gas velocity employed of 0.6 ft/sec (18.3 cm/s). Other details are provided in Table 1.

Table 1. Details of the reactor geometry and operating conditions during GDT scans.

| | |
|---|---|
| Reactor Inside Diameter | 22.5 inches (57.15 cm) |
| Insulation Outside Diameter | 28.0 inches (71.12 cm) |
| Reactor Total Length | 28.3 feet (862.58 cm) |
| Height of Dispersed Slurry | 20 feet (609.6 cm) |
| Slurry Concentration | 24-25 wt % |
| Internals as Heat Exchangers | 22 vertical U-tubes of 0.75 inch SCH 80S pipe with an internal header<br>• 12 U tubes near the wall<br>• 10 U tubes near the center<br>• Tubes occupy 9.6% of the reactor cross-section |
| Average Reactor Temperature | 502.1 $^{o}$F (261.2 $^{o}$C) |
| Average Reactor Pressure | 710.1 psig (4.99 MPa) |
| Inlet Gas Superficial Velocity | 0.6 ft/sec (18.3 cm/s) |
| Sparger | Proprietary |

Figure 1 shows the details of the scanning assembly along with the source and detector collimators in a plane along the reactor cross-section. In this scanning configuration, the source and detector are placed diametrically opposite to each other at a fixed axial elevation and move simultaneously from one end to the other of the reactor cross-section to acquire projection measurements along several chords. From these projection measurements, the chordal gas holdup can be obtained using the Beer-Lambert's law for radiation attenuation (Kumar, 1994). It should be noted that the quality of the projection measurements is critically dependent on the degree of source and detector collimation as well as on the precision in positioning the source and detector with respect to each other. The reader is referred to Kumar (1994) for an in-depth discussion on the sources of error in a $\gamma$-ray tomographic scan.

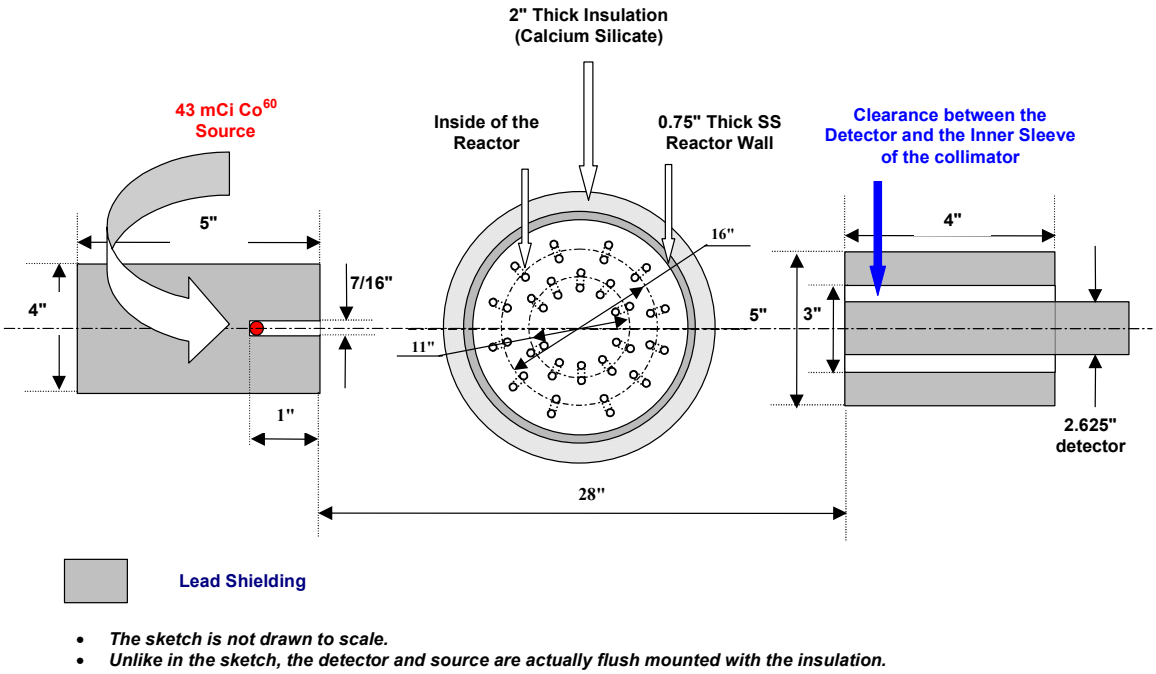


Figure 1. Schematic (not to scale) of the reactor cross-section with the collimated source and detector placed on diametrically opposite sides of the column.

Stated concisely, to estimate the chordal average gas holdup from such projection data, the following information is required along each measured chord:

1. Intensity counts ($I_{Gas}$) with the reactor cross-section filled with just the gas phase (*Base scan in the gas phase*)
2. Intensity counts ($I_{Slurry}$) with the reactor cross-section filled with just the suspended homogeneous slurry (*Base scan in the slurry phase*)
3. Intensity counts ($I_{Slurry+Gas}$) with the reactor cross-section filled with both the gas and suspended homogeneous slurry under actual operating conditions

From the above three measurements, the chordal average gas holdup can be estimated as:

$$\bar{\varepsilon}_{g,chord} = \frac{ln\left(I_{Slurry+Gas} / I_{Slurry}\right)}{ln\left(I_{Gas} / I_{Slurry}\right)} \quad (1)$$

Due to practical limitations arising from the flow of SynGas through an empty reactor, the base scans for the gas phase were conducted using Nitrogen flowing through the reactor at ambient conditions instead of the required process gas at operating pressure and temperature. Similarly, the base scans for the suspended homogeneous slurry were substituted for by scans conducted using Durasyn-164 oil at two different temperatures instead of the actual slurry. This oil was used as the liquid phase at start-up when there is no FT wax present in the reactor. Therefore, one needs to correct the radiation intensity counts obtained from the base scans in Nitrogen and Durasyn-164 to get the equivalent base scans in the reactor filled with process gas and reactor filled with slurry, both at the operating conditions at which the three-phase (pseudo two-phase) scans were performed. The procedure for this correction is presented subsequently.

The gamma-densitometry scans were conducted at two angular orientations $90^{o}$ apart (relative to the reactor cross-section) as shown in Figure 2, which also reveals the identities (from -8 to 12 in each direction) of the various chords along which measurements were made. These two scan orientations are referred to as "Section B" and "Section A" in this study to be consistent with the notation provided with the raw data from these experiments. The scans were repeated once for each of the reactor media investigated. Thus, ***for each scanning orientation*** (Section B and Section A), the following data was collected:

1. Scan 1 and Scan 2 with Nitrogen (at atmospheric condition) as the reactor medium.
2. Scan 1 and Scan 2 with cold Durasyn-164 oil as the reactor medium.
3. Scan 1 and Scan 2 with hot Durasyn-164 oil as the reactor medium.
4. Scan 1 and Scan 2 under the actual operating conditions.

For each measurement along a given chord, the source and the detector were manually positioned on diametrically opposite sides of the reactor. However, due to severe space limitations, and given the precision of the mechanical mounting devices for the source and the detector, uncertainties in position and complexities in the analysis of

the data collected from these scans were anticipated. Given below is a list of the possible sources of error in the acquired data (in order of their importance).

- Misalignment between the source and detector from one scan to another at a given chord
- Imprecise re-positioning of the source-detector assembly along a given chord from one scan to another
- Presence of numerous (and possibly non-stationary) heat exchanger tubes in the reactor

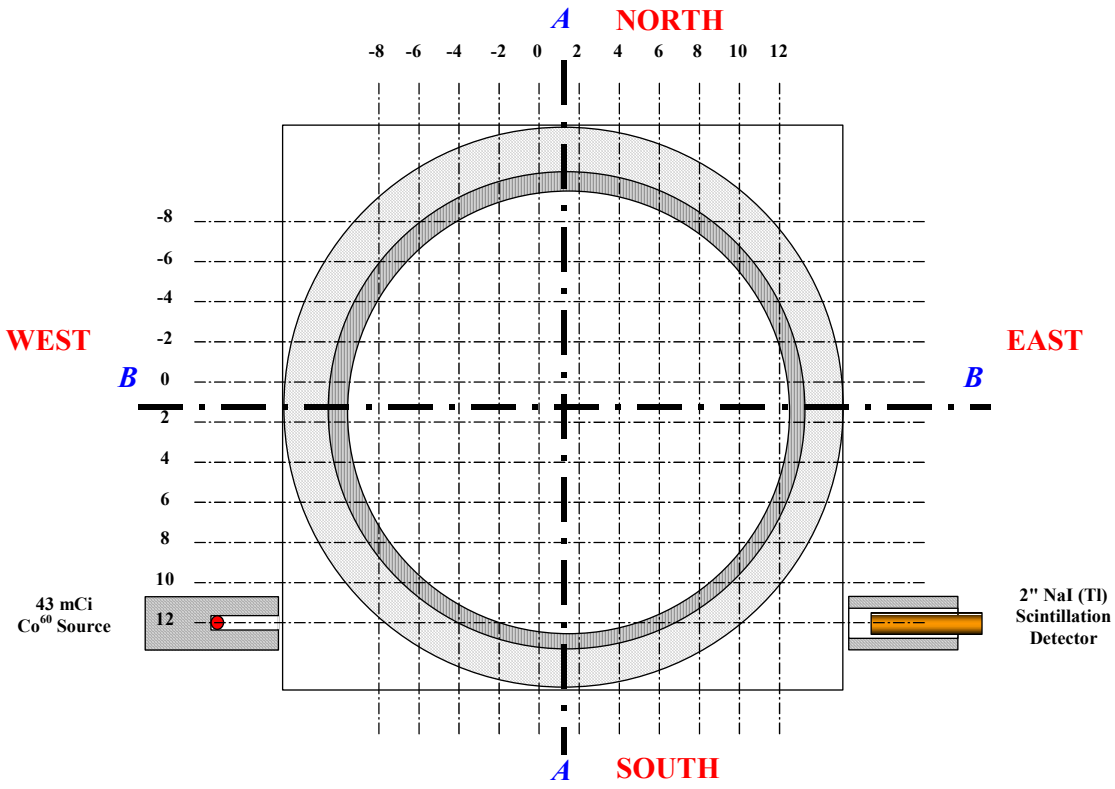


Figure 2. Distribution of the chords in the reactor cross-section at which measurements were made along directions A-A and B-B.

A brief and illustrative description is provided of a few of the several possibilities of misalignment of the source and detector collimators during gamma scans at the AFDU.

From Figure 1, one can calculate the maximum offset (calculated to be ± 2.7° from Equation 2) in the orientation of the source-collimator assembly relative to the scanning frame (given that the detector-collimator is perfectly aligned relative to the frame) for the radiation beam to be completely missed by the detector. Since the source strength is large, and no negligible counts are reported for data along any chord, one can say with some certainty that the offset in the angular placement of the source and detector assemblies was less than 2.5° (ICI Tracerco claims the offset to be within ± 1°). However, an angular offset of even a degree or so could cause vastly different attenuation length through the numerous internal heat exchanger tubes. A numerical example is being presented here to illustrate the point in discussion.

$$\theta_{offset} = \tan^{-1}\left(\frac{\pm 2.625/2}{28}\right) = \pm 2.7^{\circ} \tag{2}$$

Let us consider the case of the central chord of the reactor where no internals were present, and let the counts which one would get when the radiation beam is perfectly passing along this central chord be represented by $I_{no\ offset}$. Now, let us consider the case when there was a slight angular offset in the source collimator assembly which caused the radiation beam to pass through several of the internal heat exchanger tubes. Let us denote the length through the internals to be $l_{int}$, and the counts obtained in this scenario be represented by $I_{offset}$. Therefore, for the case of the nitrogen scan, the ratio of counts obtained when there is offset to the one when there is no offset is given by Equation 3.

$$\frac{I_{offset}}{I_{no\ offset}} = \exp\left\{-l_{\text{int}}\left(\rho_{\text{int}}\mu_{\text{int}} - \rho_{N_2}\mu_{N_2}\right)\right\} \tag{3}$$

The worst case scenario for $I_{offset}$ to be significantly different from $I_{no\ offset}$ would be that this offset causes $l_{int}$ to be equal to several internal HX tube diameters. If we assume that the offset causes the beam to pass through four heat exchanger tubes, then $l_{int}$ would be roughly 3". Using appropriate density and absorptivity values for the internals and nitrogen, one gets from Equation 3 the ratio to be 0.72. Thus, a small offset can cause a variability as large as 25-30 %. Additional specific numerical examples can be analyzed based on geometrical arguments for specific misaligned configurations of the source and

detector assemblies. However, the potential for inaccuracies in measurements is immediately evident from this example.

Therefore, in view of the given aforementioned sources of possible errors in the measured data, it becomes necessary to ascertain bounds on the accuracy of these measurements. This has been achieved by several combinatorial evaluations of the experimental data to mimic misalignments resulting from re-positioning of the source detector assemblies. Provided below is a brief description of the analysis of the data from these scans.

## 1.2. Statistical Analysis of the Measured Data

As already mentioned, to get an estimate of the gas holdup along a chord, one measurement is required in the gas phase, one in the slurry phase, and one in the gas-slurry mixture at operating conditions of interest, all executed precisely along the same chord! For a given gas-slurry measurement, the ***base*** scans in the gas and slurry phases can be chosen from one of the eight ($2^3$) possible combinations available from the scans in Nitrogen and cold & hot Durasyn-164 as shown in Table 2. In other words, for the base scan in the gas phase, one has the choice to either use Scan1 in Nitrogen or use Scan 2 in Nitrogen. Similarly, for the base scan in the slurry phase, one has four choices – Scan 1 or Scan 2 in either hot or cold oil. Therefore, one has a total of eight (two times four) ways in which to choose a set of base scans for the gas and the slurry phases. Then for a projection measurement along a chord under gas-slurry flow conditions, one can employ any of these eight combinations to estimate the chordal average holdup along that particular chord. If the base scan measurements were reproducible; the estimated chordal average gas holdup should be fairly independent of the combination that was used to represent the base scans. Alternatively, if the variation in the estimated chordal average gas holdup (characterized here by two standard deviations implying 95% confidence) is significant, it indicates the poor confidence in the measured data thereby pointing to developmental needs to make this technique reliable.

Table 2. Combinations of base scans in gas and liquid employed for statistical study.

| Combination Number | Basis for Gas Phase Scan | Basis for Slurry Phase Scan |
|---|---|---|
| 1 | Scan 1 in Nitrogen | Scan 1 in cold Durasyn-164 |
| 2 | Scan 1 in Nitrogen | Scan 1 in hot Durasyn-164 |
| 3 | Scan 1 in Nitrogen | Scan 2 in cold Durasyn-164 |
| 4 | Scan 1 in Nitrogen | Scan 2 in hot Durasyn-164 |
| 5 | Scan 2 in Nitrogen | Scan 1 in cold Durasyn-164 |
| 6 | Scan 2 in Nitrogen | Scan 1 in hot Durasyn-164 |
| 7 | Scan 2 in Nitrogen | Scan 2 in cold Durasyn-164 |
| 8 | Scan 2 in Nitrogen | Scan 2 in hot Durasyn-164 |

Therefore, to test for reproducibility, each of these combinations for base scans in Nitrogen and Durasyn-164 was used to estimate the chordal average gas holdup along each chord. In order to estimate this however, the Nitrogen and Durasyn-164 need to be corrected for density so that one obtains the scans representative of the reactor gas and reactor slurry, respectively. The following procedure describes the methodology that was adopted for correction of the base scan data in Nitrogen and Durasyn-164.

- Choose a particular combination (from the possible eight shown in Table 2) of the base scans in Nitrogen and in Durasyn-164. A "scan" stands for the intensity counts measured along various chords in one direction (either A-A or B-B).
- For a given chord, let the intensity counts acquired with Nitrogen as the reactor medium be $I_{N_2}$ and those acquired with Durasyn-164 as the reactor medium be $I_{D_{164}}$. Therefore, from Beer-Lambert's law, one has the following relations

$$I_{N_2} = I_0 \, exp\left\{ - \rho_{ins}\mu_{ins}d_{ins} - \rho_{wall}\mu_{wall}d_{wall} - \rho_{N_2}\mu_{N_2}d_{chord} \right\} \tag{4}$$

$$I_{D_{164}} = I_0 \, exp\left\{ - \rho_{ins}\mu_{ins}d_{ins} - \rho_{wall}\mu_{wall}d_{wall} - \rho_{D_{164}}\mu_{D_{164}}d_{chord} \right\} \tag{5}$$

- From Equations (4) and (5), obtain an estimate of the chord length by Equation (6).

$$d_{chord} = \frac{ln\left(I_{N_2}/I_{D_{164}}\right)}{\left(\rho_{D_{164}}\mu_{D_{164}} - \rho_{N_2}\mu_{N_2}\right)} \tag{6}$$

- Knowing the chord length from Equation (6), use Equations (7) and (8) to correct for the medium density and estimate the chordal-average counts for the cases when the reactor medium is the process gas and the slurry, respectively at the same operating conditions as the two-phase scan:

$$I_{Gas} = I_{N_2}\, exp\left\{ -(\rho_{Gas}\mu_{Gas} - \rho_{N_2}\mu_{N_2})\, d_{chord} \right\} \quad (7)$$

$$I_{Slurry} = I_{D_{164}}\, exp\left\{ -(\rho_{Slurry}\mu_{Slurry} - \rho_{D_{164}}\mu_{D_{164}})\, d_{chord} \right\} \quad (8)$$

- In Equations (4) to (5), subscripts "ins" and "wall" refer to the reactor insulation and reactor wall, respectively, $\mu$ is the mass attenuation coefficient ($cm^2/g$) for the specific material under consideration and is estimated by the computational tool (http://physics.nist.gov/PhysRefData/Xcom/html/xcom1.html). The estimation procedure requires as input the chemical composition of the material, which is simply the chemical formula in case of pure elements or compounds. For mixtures consisting of more than one compound, the input consists of the chemical formulae of the constituting compounds and elements along with their weight fractions. The mass attenuation coefficients were therefore readily estimated for Nitrogen, Durasyn-164 (assuming its molecular weight to be that of a compound with 80% by weight of $C_{30}$ alkane and 20% by weight of $C_{40}$ alkane) and for the process gas (by evaluating the average chemical composition of the gas in the reactor from the measured inlet and outlet compositions). The mass attenuation coefficient of the slurry was estimated for the $Cs^{137}$ source. However, since a $Co^{60}$ source was employed for the γ-scans, the mass attenuation coefficient of the slurry needs correction to be representative of a $Co^{60}$ source. It was assumed that this correction is given by Equation 9 since mass attenuation coefficients are known to depend mainly on photon energy (Tsoulfanidis, 1983).

$$\left(\mu_{Slurry}\right)_{Co^{60}} = \left(\mu_{Slurry}\right)_{Cs^{137}} \left\{ \left(\mu_{N_2}\right)_{Co^{60}} / \left(\mu_{N_2}\right)_{Cs^{137}} \right\} \quad (9)$$

- All this information was subsequently used for generating the base scans for the process gas and the slurry at the operating conditions of the two-phase scan by Equations (7) and (8).

- Once $I_{Gas}$ and $I_{Slurry}$ are known for a given chord by the procedure outlined above, the chordal average gas holdup is estimated by Equation (1) knowing the intensity counts registered along the same chord when the reactor medium is a gas-slurry mixture ($I_{Slurry+Gas}$). In this manner, the eight combinations of the base scan data for each chord in both the directions were evaluated against each of the two scans performed under the actual operating conditions to obtain the bounds in the chordal gas holdup estimates.

Figures 3 through 6 show the range of estimated variations in the chordal average gas holdup from the various combinations of the base scans as outlined above. Along each section (B-B and A-A), two scans were acquired under actual process conditions and are referred to as "Online Scan" in the figures. The chord identity (ID) notation is the same as reported along with the original data and the relative placement of the various chords in these two sections have been shown earlier in Figure 2. In addition to the chordal averaged gas holdup estimated from the γ-scan measurements at each chord, the dashed lines in the above figures show the chordal averaged gas holdup estimated from the combination of the Differential Pressure (DP) and Nuclear Density Gauge (NDG) measurements. Details of estimating the parameters of the assumed radial gas holdup profile (Equation 10) using the DP and NDG measurements are presented later in Section 2. Following are the main observations that emerge from these figures:

1. The variations/uncertainties in the chordal averaged holdups estimated from γ-scan measurements are significant. Except for a few central chords, these variations are significantly higher for chords near the walls in Section A-A as compared to those in Section B-B.
2. The expected trend of higher gas holdup in the center of the reactor, as shown by the chordal averaged gas holdups estimated from DP-NDG measurements, is captured by the γ-scan measurements only in Section A-A with the chordal averaged gas holdups from Section B-B being relatively uniform.
3. If results from these two scans are taken at face value, the gas distribution and consequently the flow in the plane of the scans doesn't appear to be axisymmetric

which is contrary to most of the evidence from more precise laboratory scale experiments in a similar size vessel (Chen *et al*., 1998). However, given the inherent uncertainties in these measurements, any conclusions regarding the asymmetry of long-time averaged gas holdup distribution would be far-fetched.

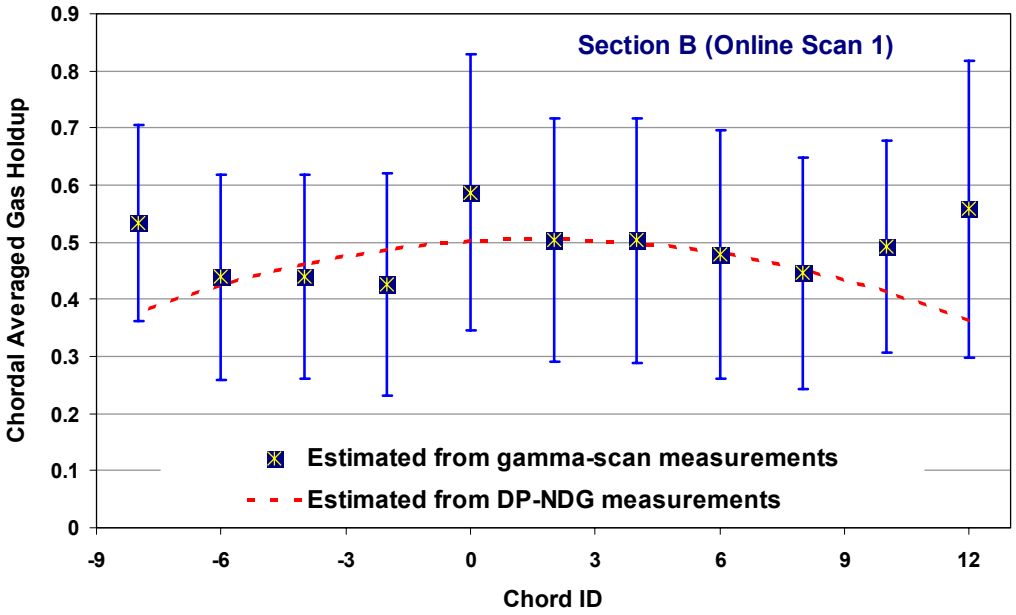


Figure 3. Mean chordal averaged gas holdup for Scan 1 along Section B (bounded by two standard deviations).

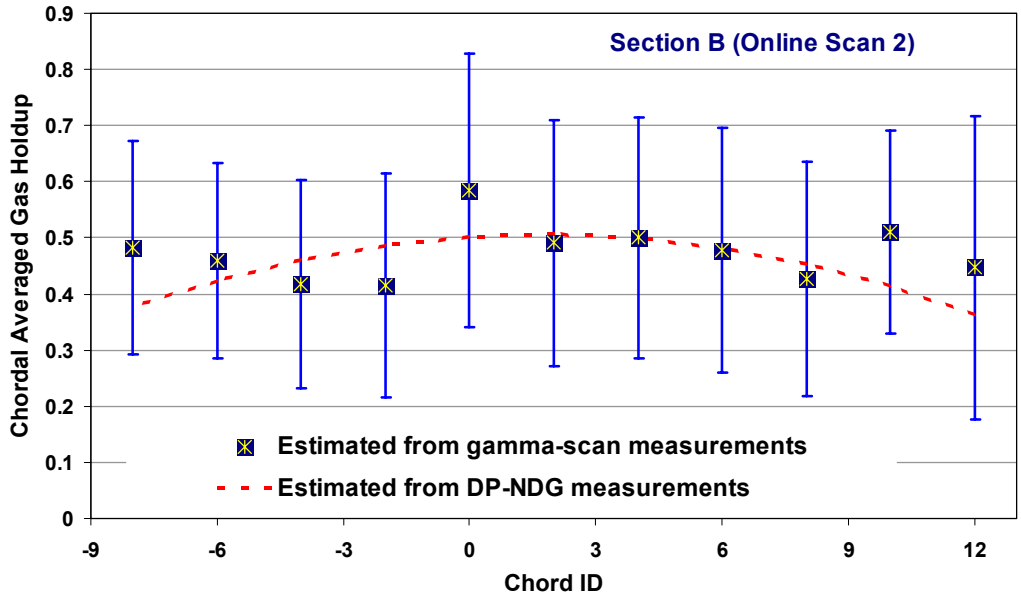


Figure 4. Mean chordal averaged gas holdup for Scan 2 along Section B (bounded by two standard deviations).

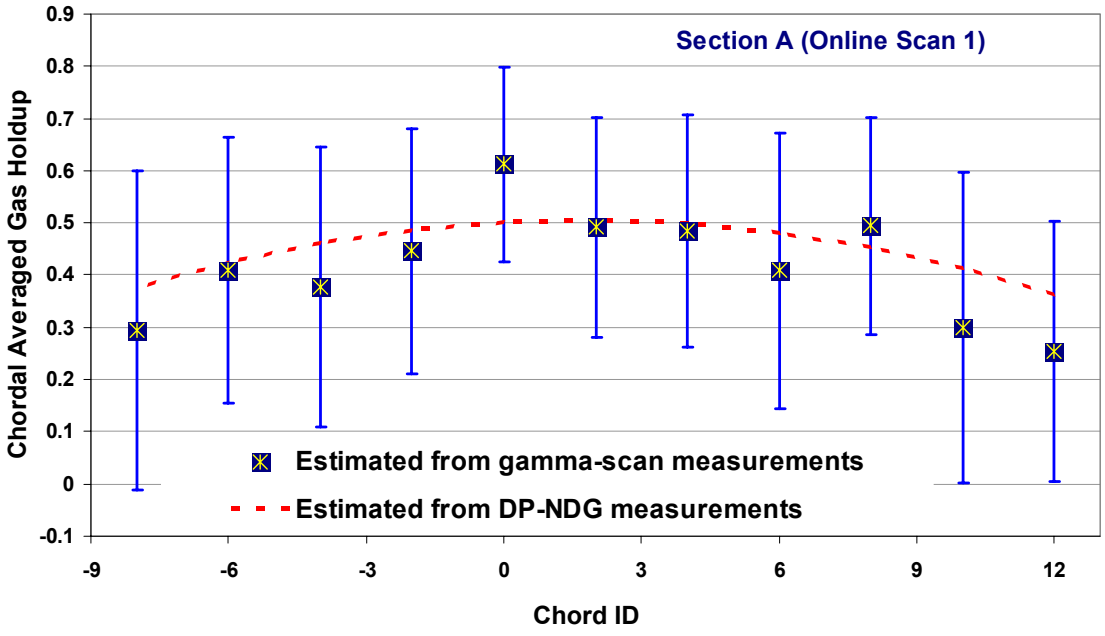


Figure 5. Mean chordal averaged gas holdup for Scan 1 along Section A (bounded by two standard deviations).

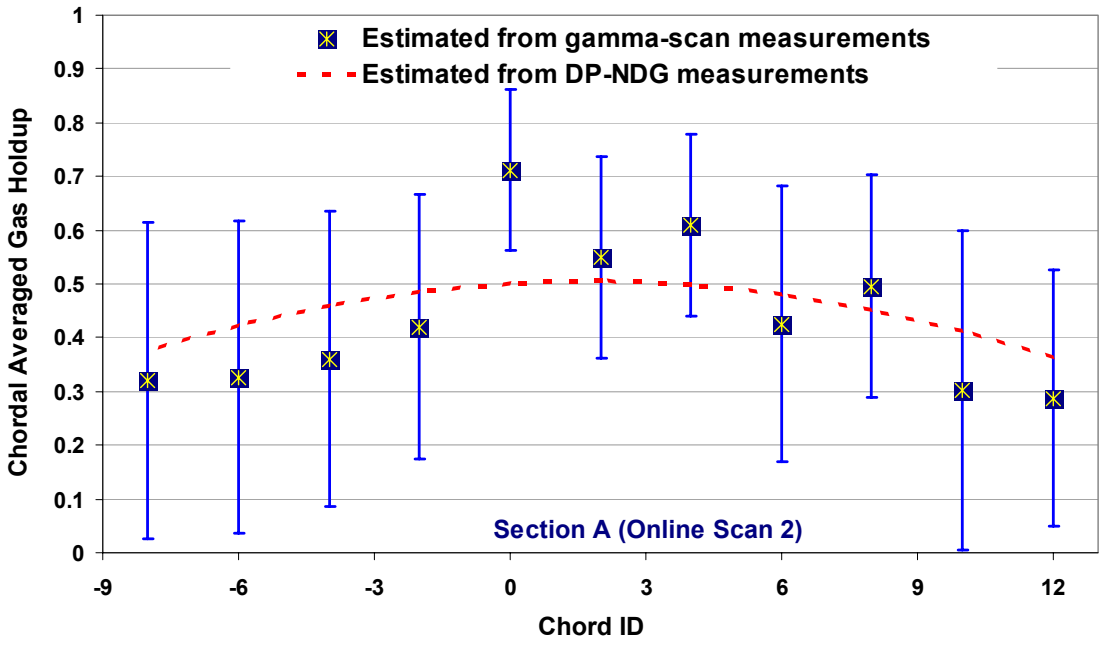


Figure 6. Mean chordal averaged gas holdup for Scan 2 along Section A (bounded by two standard deviations).

In view of this analysis, the accuracy and reproducibility of the existing gamma scan technique applied at LaPorte appears suspect and no firm conclusions can be drawn regarding the radial gas holdup distribution in the column. Having identified previously the potential sources of errors associated with the current scanning protocol, a few precursory measurements offline become an obvious necessity in order to do better in the future. Presented in the following sub-sections are some suggestions for improving the quality of acquired data from such measurements; and if adherence to a strict protocol is followed based on these suggestions, densitometry measurements hold the potential to become routine for all pilot scale studies at the AFDU.

### 1.3. Suggestions for Improving Data Quality from Future Gamma Scans

To properly execute the densitometry scans on the pilot units at AFDU, the following protocol is recommended and should be followed to improve data quality:

1. Conduct tests on mock-ups of known cross-sections and of known density variations using the same scanning assembly as employed during the previous scans on the LaPorte reactor, in order to better understand the effects of source-detector misalignment on the quality of the acquired data.
2. Conduct mockup tests to examine the utility of base scans obtained by using several different fluids and at least two different radioactive sources ($Co^{60}$, $Cs^{137}$) and to check the validity of the linear correction schemes (Equations 5 to 7).
3. Identify axial locations along the reactor where least movement of the internals is expected as the scanning locations. Alternatively, mechanisms to support the tubes inside the reactor could be improved. Currently, the internal heat exchanger U-tubes are mounted on a manifold very near the top of the reactor. At some location in the middle portion of the reactor, they are strapped again. As a result, due to the vigorous flow of the gas and slurry during operation, they sway and move because of the energy of the contacting fluids. Therefore, if locations where the movements are minimal could be identified, the uncertainties resulting from the movement of internal HX tubes could be reduced.
4. Position detector and source with increased accuracy with respect to the reactor.

## 1.4. Suggested Mock Experiments

To estimate the inaccuracies due to source-detector misalignment and re-positioning of the source-detector assembly at a given chord from scan-to-scan, the following experiments are suggested. With the same assembly that was used for the gamma scans at LaPorte for FT-IV runs, the following scans should be conducted:

- An empty transparent column (maybe made of Plexiglas) should be scanned several times and the reproducibility in counts checked.
- The same column should then be scanned filled with water. This procedure should also be repeated several times and criterion for reproducibility should be established.

- From these two scans, one should calculate the absorptivity coefficient for water and check it against the theoretical value for the employed radioactive source.
- In the next set of experiments, several repeated scans should be acquired with an empty glass cylinder placed at a known location inside the column filled with water, and the acquired data should be checked for reproducibility in counts. This procedure will enable the assessment of the equipment's ability to measure data capable of capturing the presence of the empty glass cylinder inside the column (which is representative of the internals in the pilot-scale reactors).
- The experiments should also be conducted by performing base scans with fluids other than the one of interest to test the assumptions made in correcting the base scans as done in the current analysis.

***In all these scans, one should absolutely ensure that the relative position of the column with respect to the source-detector assembly is never compromised.*** It is our experience with the tomography setup in our laboratory that even a millimeter or so of misalignment in the column with respect to the scanning assembly causes large variations in the measured gas holdup distributions. In CREL, using a different tomography system, gas holdup profiles are obtained with reproducibility better than ± 3% (Kumar 1994).

To summarize, given the accuracy and reproducibility of the existing gamma scan technique applied at AFDU, no firm conclusions could be drawn regarding the radial holdup distribution in the reactor. Therefore, incorporation of the holdup profile information from these scans in the liquid and gas phase mixing models for prediction of tracer responses cannot be reliably accomplished. However, given the difficult nature of these experiments and numerous constraints due to space and safety, this was a remarkable achievement. It should be evident then that with some dedicated efforts and from the lessons learned during this study, the reliability of the data from this invaluable diagnostic tool could be significantly improved for future pilot scale experiments.

## 2. Radioactive Tracer Studies During FT-IV Runs at the Alternate Fuels Development Unit (AFDU) in LaPorte, Texas

The second part of the hydrodynamic study at AFDU during FT-IV trial runs was the estimation of backmixing in the gas, liquid and catalyst phases using tracer techniques. Given the hostile operating conditions prevalent in a slurry bubble column reactor, tracing methods using off-the-shelf probes provide little hope. Even if robust probes could be identified, one needs ports to install them at the desired measurement locations. This could be a task that could become very challenging or expensive and is not usually a preferred method. Tracer experiments using radioactive tracers provide a significant advantage in this regard. Being completely non-intrusive, the measurement probes (scintillation detectors) could be positioned at any desired location outside the reactor. The radioactive tracing technique, however, does suffer from the fact that interpretation of the acquired data is not straightforward and requires assumptions about the relationship of the measured signal (radiation counts from the tracer) to the tracer concentration. In standard tracer techniques where there is a linear relationship between the tracer concentration and the tracer property that is actually measured, there is little ambiguity regarding data interpretation. Such, unfortunately, is not the case with radioactive tracer methods because of the complex interactions that a radiation photon undergoes in its sojourn from its source (tracer particles) to its destination (scintillation detectors) as described by Gupta (2002). It was shown in his study that in the absence of a perfect collimation, the response registered by a scintillation detector is broadened as a result of the counting process and can in principle be modeled if a description of reactor and collimation geometry as well as distribution of the radioactive tracer is known. This, unfortunately, calls for extensive computing capabilities and is not reasonably simple and realistic to implement. Therefore, the simulated normalized responses are compared with equivalent normalized experimental responses (Gupta, 2002).

With the advantages far outweighing the disadvantages, radioactive tracer experiments were conducted at the AFDU, LaPorte using gas, liquid and solid radiotracers to assess the degree of backmixing in the three phases. Figure 7 shows the

schematic representation of the reactor and the array of 2" NaI (Tl) scintillation crystals used for monitoring the temporal tracer distributions at various locations in the reactor. Given the expensive nature of these measurements as well as the time constraints, only two of the three superficial gas velocities were employed for tracer studies. The operating conditions for these two runs (Run 16.6 and Run 16.7) are provided in Table 3. The gas tracer was Argon-41 ($Ar^{41}$) whereas catalyst particles doped with Manganese-56 ($Mn^{56}$) were used as solid tracer. The "liquid tracer" was a fine powdered oxide of $Mn^{56}$ ($Mn_2O_3$) suspended in the heat transfer oil, and therefore, was actually a *liquid-like* tracer as opposed to being a true liquid tracer. This tracer was unfortunately employed only for liquid tracer experiments during Run 16.7, since for Run 16.6 a coarser oxide of $Mn^{56}$ ($MnO_2$) was accidentally used that resulted in tracer plugging in the slurry outlet.

The gas holdup values measured by Nuclear Density Gauge (NDG) and Differential Pressure (DP) also reported in Table 3. NDG gives the gas holdup along the central chord of the reactor while DP gives the average (overall or volumetric) gas holdup between the two ports where the differential pressure is measured. For a uniform gas holdup, both of these values are the same. However, when there is a radial distribution of gas holdup with higher holdups in the central region and lower near the reactor walls, gas holdup from NDG is always higher than that measured by DP (Degaleesan, 1997). A frequently employed radial distribution of gas holdup is given as (Kumar, 1994)

$$\varepsilon_g(\xi) = \bar{\varepsilon}_g \left( \frac{m+2}{m+2-2c} \right) \left( 1 - c\xi^m \right) \tag{10}$$

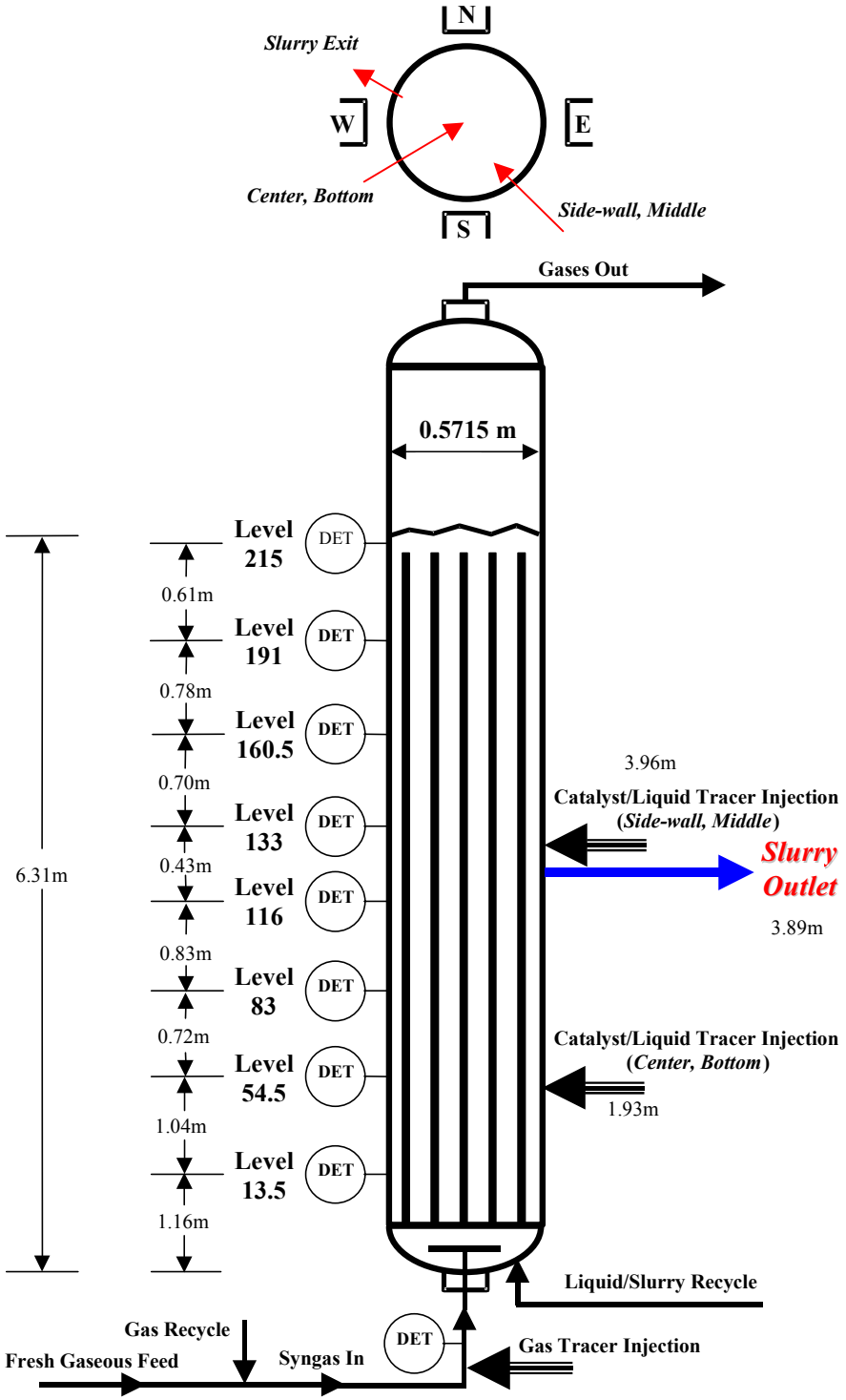


Figure 7. Schematic of the slurry bubble column reactor at the AFDU along with the scintillation-detector placement for measuring tracer responses.

In Equation 10, $\bar{\varepsilon}_g$ is the cross-sectional average gas holdup, the parameter "c" controls the gas holdup near the wall and can range anywhere from 0 to 1, while parameter "m" can be anything greater than zero. The gas holdup distribution in Equation 10 assumes that the long-time averaged gas holdup distribution in the reactor cross-section is axisymmetric. From the results of the densitometry scans presented in Section 1, the assumption of axisymmetry of gas holdup cannot be ascertained. However, for a column of 18" diameter and with internal tubes similar to those in the AFDU reactor, CT measurements in CREL established that the distribution of gas holdup was reasonably axisymmetric (Chen *et al*., 1998). Therefore, in the absence of any better information, the best choice is to assume the validity of the conclusions reached by Chen *et al*. (1998). Consequently, the NDG and DP measured holdups could be related to the gas holdup profile in Equation 10 as

$$\bar{\varepsilon}_G\big|_{DP} = \bar{\varepsilon}_g; \qquad \bar{\varepsilon}_G\big|_{NDG} = \bar{\varepsilon}_G\big|_{Chord} = \bar{\varepsilon}_g \left(\frac{m+1-c}{m+2-2c}\right)\left(\frac{m+2}{m+1}\right) \tag{11}$$

Table 3. Reactor operating conditions during tracer tests.

| **Operating/Measured Parameters** | **Run 16.6** | **Run 16.7** |
|---|---|---|
| Temperature ($^o$K) | 532.0 | 534.2 |
| Pressure (MPa) | 4.996 | 4.997 |
| Inlet Superficial Gas Velocity (cm/s) | 12.81 | 18.23 |
| Outlet Superficial Gas Velocity (cm/s) | 9.89 | 15.21 |
| Average Superficial Gas Velocity (cm/s) | 11.35 | 16.72 |
| Liquid (Slurry) Superficial Velocity (cm/s) | 0.727 | 0.722 |
| Height of Dispersed Media (cm) | 631 | 633 |
| $U_{gtrans}$ (cm/s) – Krishna (2000) | 9.08 | 9.63 |
| $\bar{\varepsilon}_G$ – Krishna (2000) | 0.437 | 0.512 |
| $\bar{\varepsilon}_G = \bar{\varepsilon}_G\big\|_{DP}$ | 0.494 | 0.464 |
| $\bar{\varepsilon}_G\big\|_{Chord} = \bar{\varepsilon}_G\big\|_{NDG}$ | 0.529 | 0.507 |
| m (assumed as suggested by Degaleesan, 1997) | 2 | 2 |
| c, estimated from $\bar{\varepsilon}_G\big\|_{Chord}$ | 0.351 | 0.435 |
| $\overline{\lvert d\varepsilon_g / d\xi \rvert}$ | 0.280 | 0.344 |

One immediately notes an apparent anomaly that in spite of the operating pressure in Runs 16.6 and 16.7 being the same, Run 16.7, which has a higher gas superficial velocity, recorded a lower gas holdup as compared to that in Run 16.6, which has a lower gas superficial velocity. One cannot suspect inaccuracies in gas holdup measurement since the same trend is recorded by both DP as well as NDG techniques (see Table 3). Therefore, the remaining explanation is that the operating conditions of Run 16.6 are close to transition (known to produce a local maximum in the variation of gas holdup with superficial gas velocity), while Run 16.7 is truly churn-turbulent.

Given that three parameters in Equation 10 need to be estimated with only two independent measurements (gas holdup from NGD and DP) one is left with no choice but to guess one of them. Degaleesan (1997) suggests to fix "m" as "2" and then use Equation 11 to estimate "c". This reasoning is based on laboratory scale measurements. Therefore, a comparison for various values of "m" on the estimated radial gas-holdup profiles is shown in Figure 8 for both Runs 16.6 and 16.7. It can be readily seen that "m = 2" provides the most reasonable description of the gas holdup profile as observed from the scans along Section A-A as presented earlier. With increasing "m", the profiles in the central portion of the reactor become flatter. However, to honor the fixed $\bar{\varepsilon}_g$ and $\bar{\varepsilon}_g\big|_{Chord}$ obtained experimentally, the gas holdup near the wall becomes increasingly lower and results in steeper gradients in that region. Generally, one thinks of parameter "m" as the primary controller of the gradient of the radial gas holdup profile, with higher values of this parameter resulting in flatter profiles. However, such would be the case only for fixed values of "c" and $\bar{\varepsilon}_g$. To examine the dependence of the cross-sectional mean gradient of the radial gas holdup profile, which is known to be the primary driver for liquid recirculation in bubble columns (Chen *et al*., 1998) on "m" and "c", one can derive $\overline{d\varepsilon_g / d\xi}$ using Equation 10 as

$$\overline{\frac{d\varepsilon_g}{d\xi}} = -2c\bar{\varepsilon}_g\left(\frac{m}{m+2-2c}\right)\left(\frac{m+2}{m+1}\right) \tag{12}$$

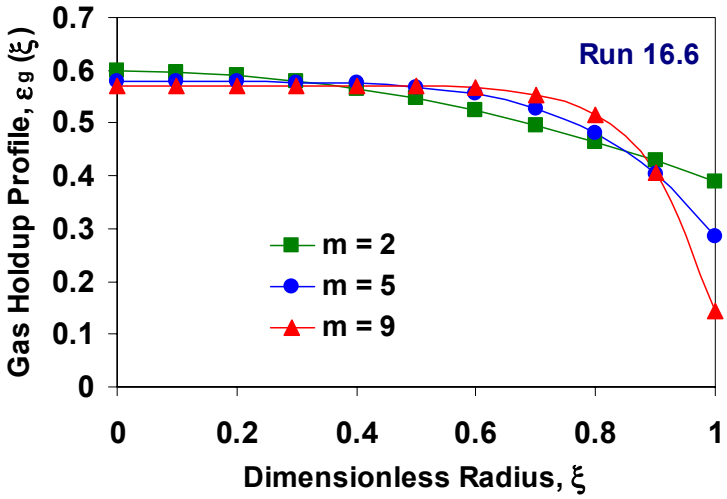


(a)

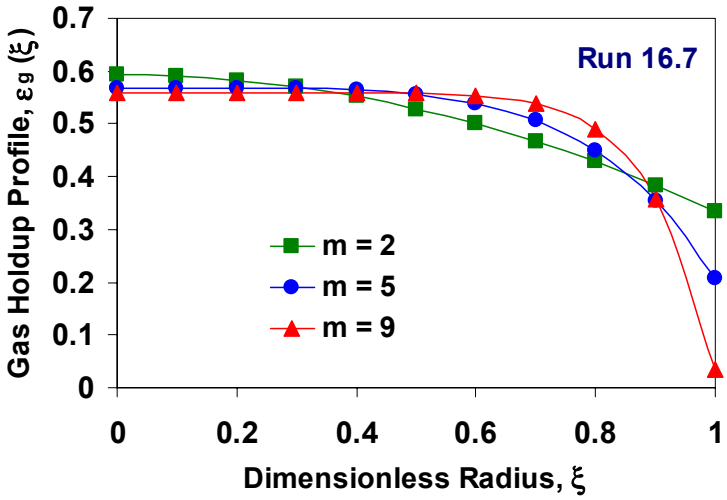


(b)

Figure 8. Effect of parameter "m" on the radial gas holdup profile for fixed $\bar{\varepsilon}_g$ and $\bar{\varepsilon}_g\big|_{Chord}$ a) Run 16.6 b) Run 16.7.

Figure 9 shows the effect of the parameter "m" on the cross-sectional mean gradient of the radial gas holdup profile estimated from Equation 12. In spite of the profiles being flatter in the central region for higher values of "m", the overall gradient in the profile increases with "m" which is contrary to the common belief that larger values

of "m" result in lower gradients. As mentioned previously, increased holdup gradient with decreasing values of "m" happens only when the parameter "c" is also fixed which is not the case here. The second interesting result is that in spite of the measured holdups being lower for Run 16.7 (the higher superficial gas velocity condition) as compared to Run 16.6, and irrespective of the value of the parameter "m", the holdup profile gradient for Run 16.7 is consistently higher than that for Run 16.6. Since it is known that higher superficial gas velocities result in greater liquid recirculation driven by larger gas holdup gradients (Chen *et al*., 1998), this is in line with such observations.

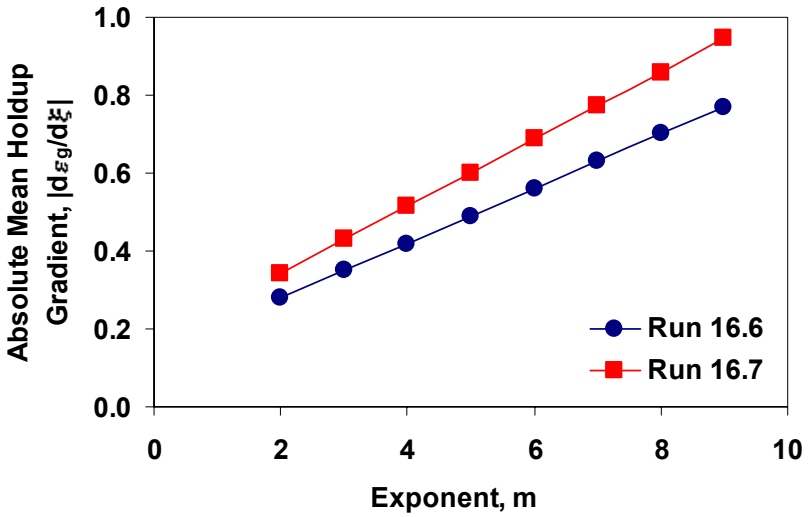


Figure 9. Effect of the parameter "m" on the absolute value of the cross-sectional mean gradient of the radial gas holdup profile for fixed $\bar{\varepsilon}_g$ and $\bar{\varepsilon}_g\big|_{Chord}$.

Table 3 also lists the estimate of the superficial gas velocity at each of the two operating conditions at which transition from bubbly to churn-turbulent flow is assumed to take place. These values have been calculated using the methodology proposed by Krishna (2000) as described by Gupta (2002). One can see that the superficial gas velocity at the outlet for Run 16.6 is reasonably close to the transition velocity while in Run 16.7 the superficial gas velocity is well above the transition value everywhere in the reactor. Since Run 16.6 is operated close to the transition superficial gas velocity and Run 16.7 well into churn-turbulent flow, this provides the most likely explanation of lower

gas holdup in Run 16.7 than Run 16.6. Since the temperature and pressure conditions during the two runs were nearly identical, one would have expected a very similar transition superficial gas velocity. However, because of the differences in the inlet gas feed concentration, the average molecular weight of the gas is different during the two runs resulting in different gas density and consequently slightly different transition superficial gas velocity. Krishna (2000) recommends that transition velocity be actually obtained experimentally by operating the reactor at several different gas superficial velocities. However, this is something that cannot be easily achieved under reaction conditions since variation in gas superficial velocity may not be possible for a stable reactor operation and due to difficulties associated with the measurement of overall gas holdup.

## 2.1. Protocol for Data Processing

The data acquired from radioactive tracer experiments needs to be processed in order to make it suitable for comparison with various flow and mixing models as well as for analysis of flow patterns and mixing in the AFDU reactor during FT synthesis. Since the mixing models are essentially one-dimensional in nature and capture the transient evolution of the tracer responses along the reactor length, it makes sense to average the data from the four detectors in a reactor cross-section at every monitoring plane. However, before that is done, the responses at several axial locations from representative gas and ”liquid” tracer tests are examined to address the radial non-uniformity of the tracer distribution. Figure 10 shows the detector responses at three different axial levels for the “liquid” tracer test during Run 16.7. Since the tracer is injected slightly below the axial level 54.5 (see Figure 7), as marked on the outside tape, using an injection port located southwest in relation to the reactor cross-section, the “South” and “West” detectors located at that axial level record higher intensity counts as compared to the “East” and “North” detectors. However, as one moves away from the injection point, the tracer gets more and more radially mixed and results in uniformity of the counts registered by the four detectors at a given reactor plane. Note however, that the four responses would not become identical since each detector has a slightly different

efficiency and therefore responds differently to the same tracer concentration distribution. Another factor that could result in different intensity counts for detectors having the same efficiencies is the differences in the wall (insulation) thickness and the internal heat exchanger tubes seen by each individual detector, since intensity counts are dependent on the intervening media in a complex manner described by Gupta (2002).

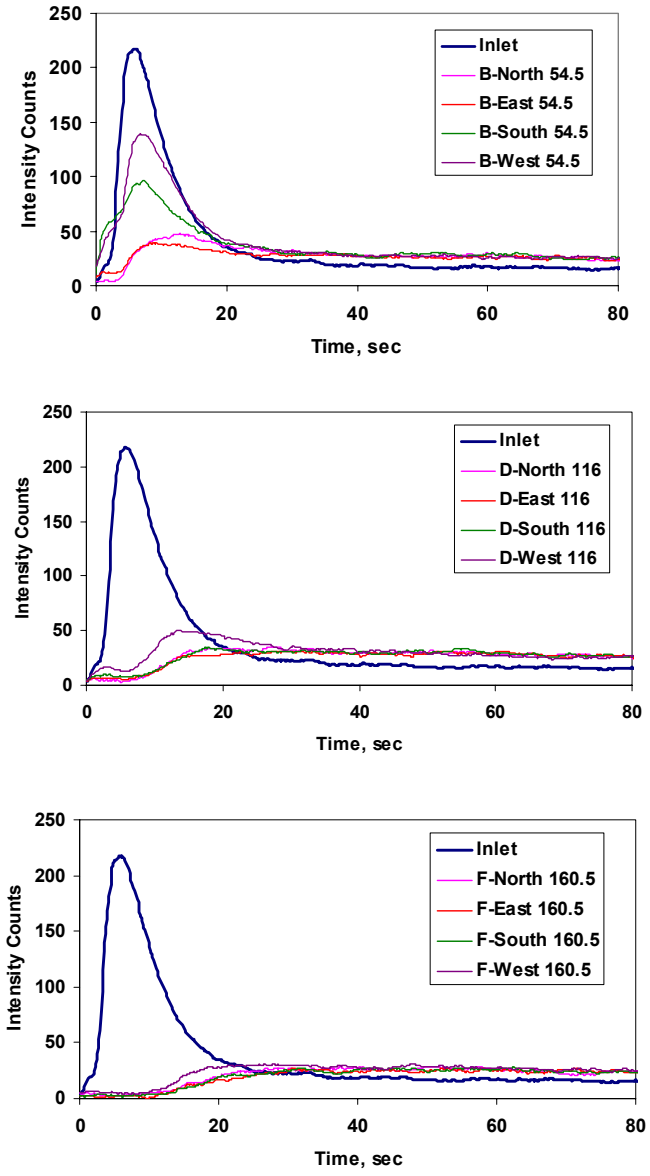


Figure 10. Radial mixing of "liquid" $Mn_2O_3$ tracer for Run 16.7 with tracer injected at the bottom center location.

For the gas tracer responses (see Figure 11), the tracer is actually injected before the sparger. As a result of the relatively high pressure-drop across the sparger, the gas tracer gets a chance to get completely mixed before entering the reactor. Therefore, gas tracer responses at a given axial elevation of the reactor are significantly more aligned as compared to "liquid" tracer responses resulting from a point injection of the tracer. The remaining differences are due to variation in detector efficiencies, variation in wall thickness and possibly non-uniform and asymmetric holdup distribution during part of the data record.

Therefore, the assumption of tracer responses being axisymmetric is reasonably good for the gas tracer tests, while the responses resulting from point tracer injection of the liquid/catalyst tracers are significantly asymmetric near the tracer injection point and become more uniform as one moves away from the injection location. However, the mixing models considered in this work are not three-dimensional, and one would require a fully coupled momentum and scalar transport solver to have a chance of capturing the asymmetry in tracer responses. Therefore, the responses at each axial location have been averaged for the purposes of this work. Here we present the various steps involved in pre-processing of the experimental data.

**Step 1**

The first step in the processing of the data measured in response to tracer injection is to average the responses of the four detectors at a given axial location. The average of the measured intensity counts for each detector is subsequently corrected for the radioactive decay of the tracers (as shown by Equation (13)).

$$I_{Corrected} = I_{Measured}\ exp(\lambda t) \qquad \lambda = \frac{ln\,2}{t_{1/2}} \tag{13}$$

The half-lives ($t_{1/2}$) of $Ar^{41}$ and $Mn^{56}$ radioisotopes are 1.8223 and 2.5785 hours, respectively (Source: http://www.dne.bnl.gov/CoN/index.html).

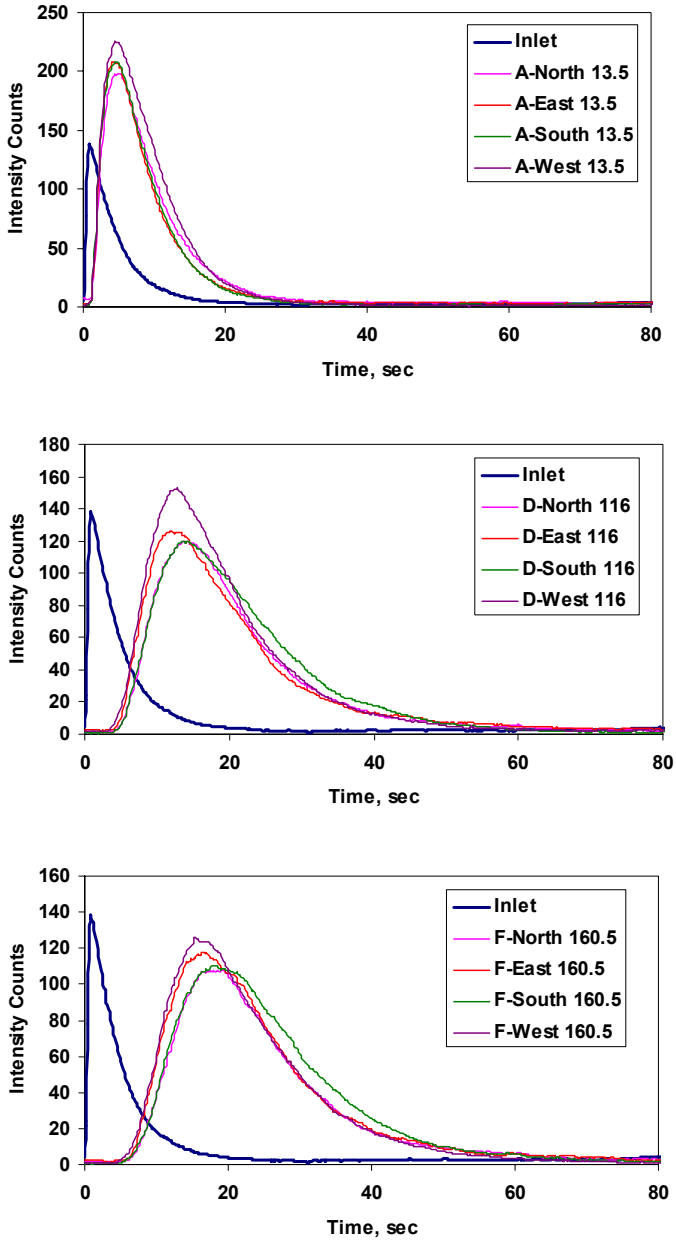


Figure 11. Radial mixing of gas tracer for Run 16.7 with tracer injected below the sparger.

**Step 2**

The next step involves the subtraction of the background counts from the corrected intensity counts obtained from step 1. For the gas tracer experiments, since the

tracer injection vial is sufficiently far from any of the detectors for them to pick-up any spurious radiation, the background count is simply taken as the average of the intensity counts measured prior to the start of tracer injection. This information is available since for all tracer measurements, the data acquisition system is triggered roughly 30-60 seconds before initiating the tracer injection. However, for injections of liquid-like (fine $Mn_2O_3$ and coarse $MnO_2$) and catalyst tracers, since some of the detectors are close to the injection vial and can, therefore, pick-up spurious radiation simply due to their proximity to concentrated radioactivity, the background is taken as the minimum counts registered during the entire length of the tracer measurement. This still leaves the spurious pick-up early radiation peak in several detector responses (as shown in Figures 14 to 17). These spurious peaks can be removed by visual inspection, although a more scientifically based method to accomplish this task may be possible by complete three-dimensional modeling of radiation interaction with the crystal. This is, however, marred by the fact that both the distribution of the radioactive tracer as well as the effective density of the reactor medium between the radioactive tracer source and the detectors are ***temporally varying*** spatial functions which are unknown, but which are required to accurately implement radiation modeling. Thus, subtraction of pick-up radiation based on visual inspection is a practical solution to this problem.

**Step 3**

The time series of tracer responses obtained from step 2 can be further processed using simple low-pass Butterworth filters in Matlab™. This step is particularly crucial if one is to employ the Axial Dispersion Model (ADM) to the measured tracer responses in an effort to extract the effective dispersion coefficient. This is because the ADM tries to fit a tracer response curve to the experimental data by iteratively adjusting the effective dispersion coefficient. Presence of noise in the experimental responses could lead to erroneous results from the optimizer or unusually long computational times during regression. This is not an issue in the current study because the models are completely predictive and nothing is fitted to experimental data. Therefore, this data processing step has not been performed on the tracer responses presented subsequently.

**Step 4**

Each time series obtained either from step 2 or from step 3, is normalized by the maximum intensity counts in that time-series to obtain the normalized detector responses presented in Figures 12 to 17. It should be remembered that while comparing these normalized experimental responses with simulation results, the simulated tracer concentration in various portions of the reactor could in principle be related to equivalent scintillation counts via a model for radiation detection as described by Gupta (2002).

## 2.2. Reproducibility of the Measured Tracer Data

Figures 12 and 13 show the tracer responses from repeated gas tracer injections for Runs 16.6 and 16.7, respectively. From these figures one can see that the reproducibility is very good suggesting that it is not necessary to have many repeated gas tracer injections. However, it is advisable that one repeat injection still be done for each operating condition as a check in future gas tracer studies. The reason for good reproducibility is the fact that the gas tracer is injected into the gas feed line prior to the gas sparger. The high pressure-drop across the sparger ensures a uniform and reproducible distribution of the tracer in the reactor cross-section at the point of tracer entry into the column, and hence the excellent reproducibility.

For the catalyst and $Mn_2O_3$ ($MnO_2$) tracers, however, a point tracer injection is made at the two tracer injection locations shown in Figure 7. The flow at these points of tracer entry into the column is continuously changing with time, and therefore, the likelihood of the tracer to encounter the same flow conditions at the instant of tracer injection from repeated tracer injections is small. Therefore, this variable local flow condition at the point of tracer introduction into the system results in a different initial spread of the tracer in the reactor cross-section, and one expects some difference in the recorded tracer responses from repeated tracer injections at the same operating conditions. This is illustrated in Figure 14 for $Mn_2O_3$ tracer injections in the reactor center for Run 16.7. Thus, for point tracer injections, one needs several repeat trials (a minimum of five is recommended) to estimate the ensemble-averaged tracer responses

(refer to Equation (14)) for comparison with mixing models which themselves simulate ensemble-averaged quantities.

$$\bar{I}(t)_{Ensemble-Averaged} = \frac{1}{N_{Tracer\ Injections}} \sum_{i=1}^{i=N_{Tracer\ Injections}} I_i(t) \tag{14}$$

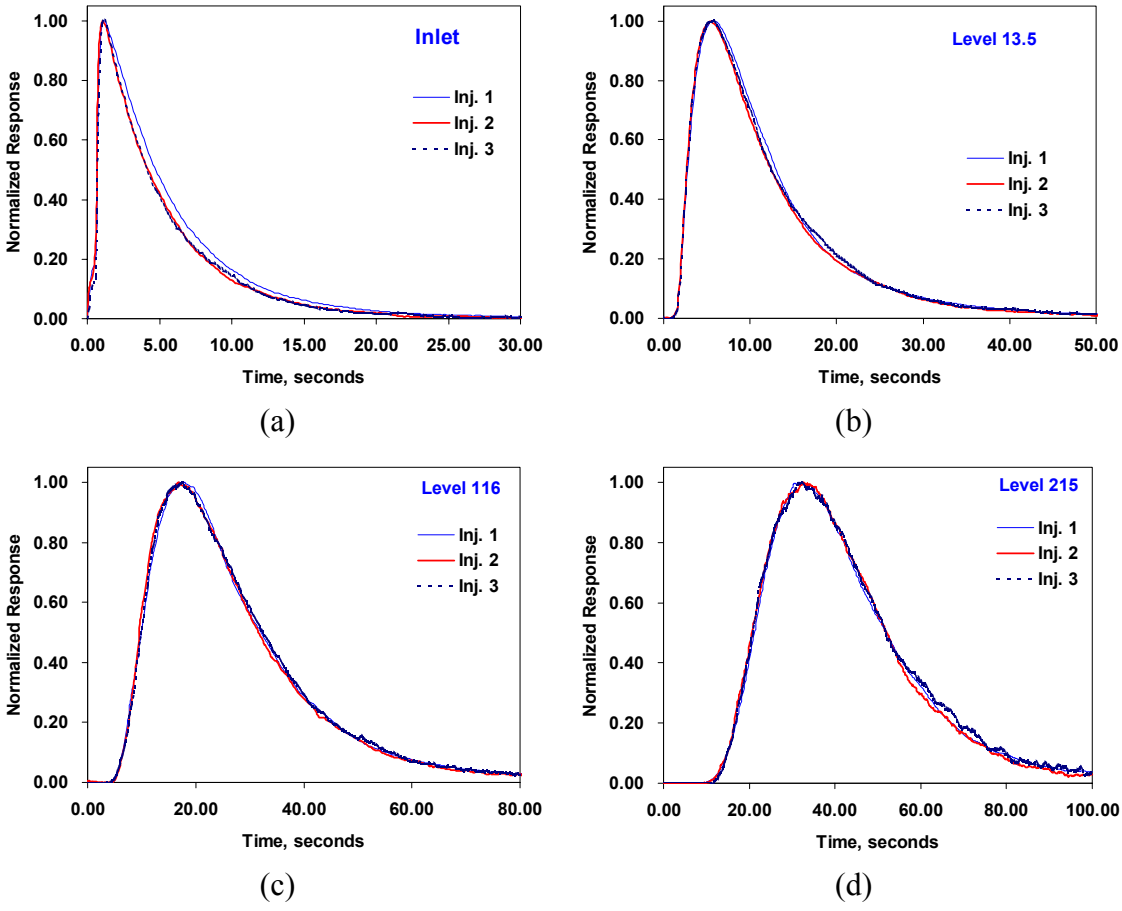


Figure 12. Result of repeated gas tracer injections for Run 16.6.

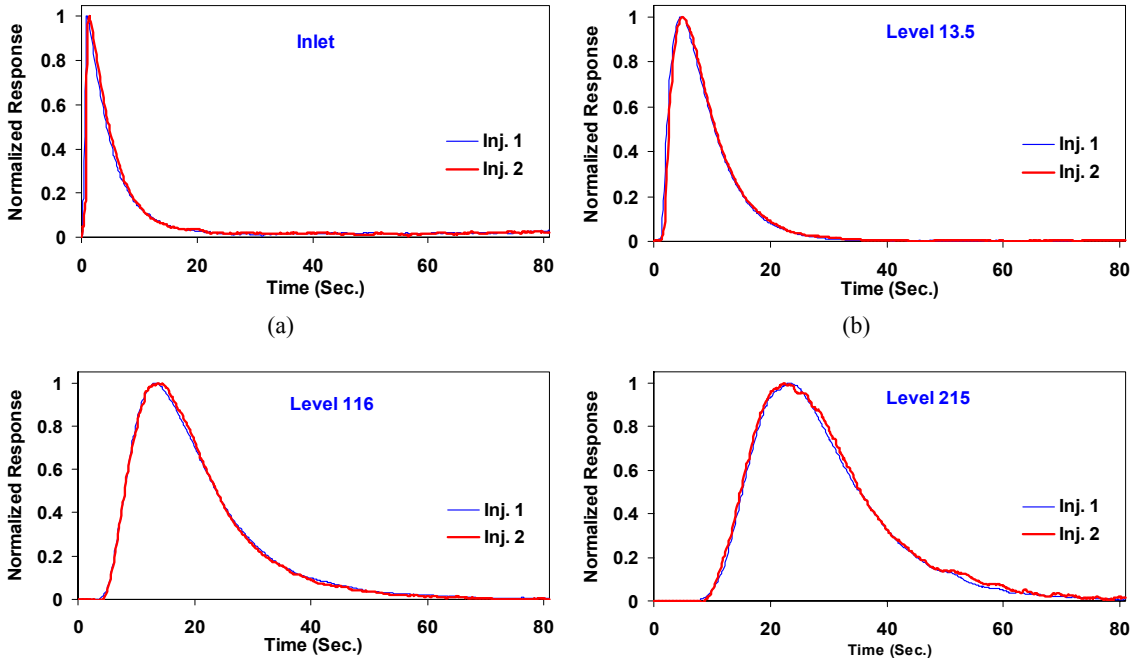


Figure 13. Result of repeated gas tracer injections for Run 16.7.

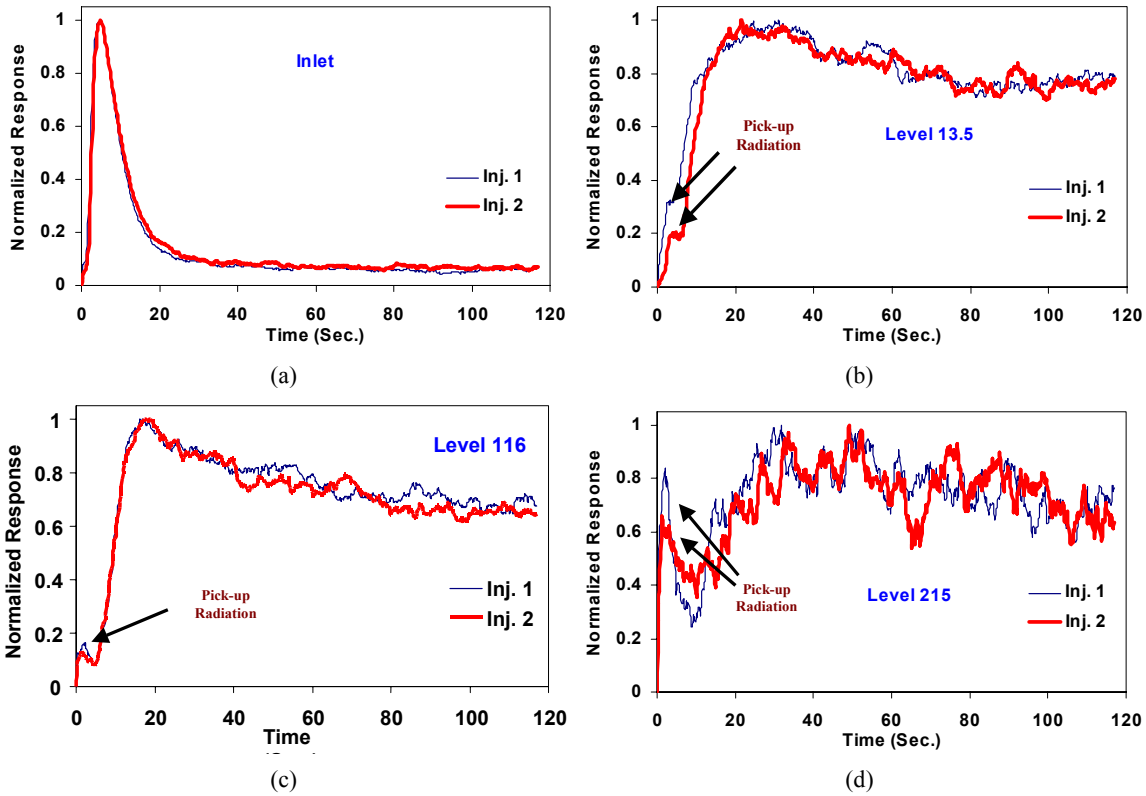


Figure 14. Result of repeated $Mn_2O_3$ tracer injections (Center, Bottom) for Run 16.7.

From Figures 14 (b) and (c), it is worth observing that even after 60-80 seconds from the time of tracer injection, the normalized responses have still not become identical. This could be caused by a changing gas holdup structure, which indirectly affects the radiation intensity counts. Alternatively, it could be due to the tracer exiting the flow domain from the slurry outlet (refer to Figure 7). Additionally, the response in Figure 14 (d) is corrupted by the closeness of the measurement location to the radiation source for the NDG measurements as well as the fluctuating gas-slurry interface.

## 2.3. Comparison between Catalyst and "Liquid" Tracer Responses

Figure 15 compares the tracer responses under identical operating conditions obtained in response to fine catalyst and coarse $MnO_2$ tracers. For conditions of Run 16.6 unfortunately, coarse $MnO_2$ tracer particles were ***accidentally*** employed to mimic the liquid phase. However, the large particle size resulted in significant settling of the tracer, and for the sidewall tracer injection, the tracer actually clogged the slurry outlet line as a result of settling. For the center-bottom injection, such a problem was not encountered since the point of tracer injection was significantly away from the slurry outlet. However, one can see from Figure 15 that settling of the tracer occurred, and the responses obtained from fine catalyst injection are significantly different from the responses of $MnO_2$ (coarse particle) injections. Therefore, for comparison with mixing models, this set of data for coarse $MnO_2$ particles has not been considered.

For tracer experiments under conditions of Run 16.7, which took place on the day following Run 16.6, the ***correct*** (fine $Mn_2O_3$) tracer particles were employed to mimic the liquid phase. Comparison of responses (averaged over repeat injections) obtained from catalyst and $Mn_2O_3$ tracer injections in the sidewall-middle and center-bottom are shown respectively in Figures 16 and 17. From these figures, one sees that the difference between the catalyst (solid) and $Mn_2O_3$ (liquid-like) tracer responses, even though clearly present, is within the range of variation in responses from repeated $Mn_2O_3$ injections as shown in Figure 14. This indicates a high probability of a well-suspended catalyst in the liquid medium, and as a first approximation, one is justified in treating the slurry in FT systems as a pseudo-homogeneous phase for modeling purposes.

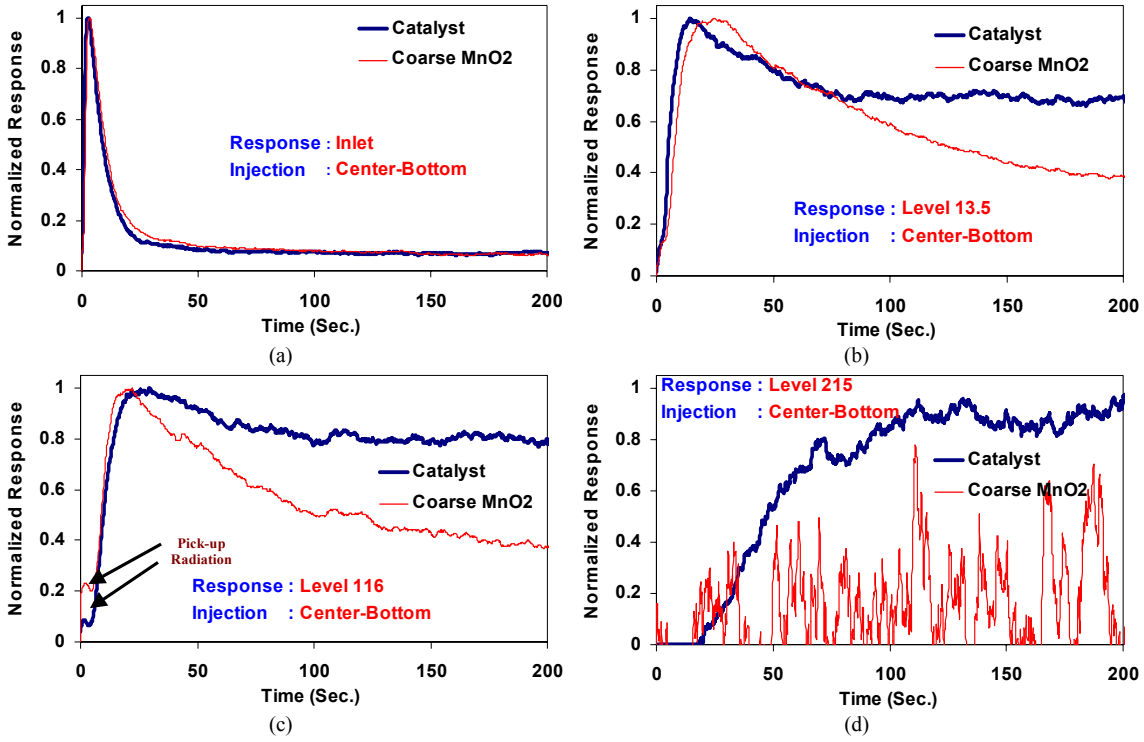


Figure 15. Comparison of tracer responses for $MnO_2$ and catalyst tracer injections (Center, Bottom) for Run 16.6.

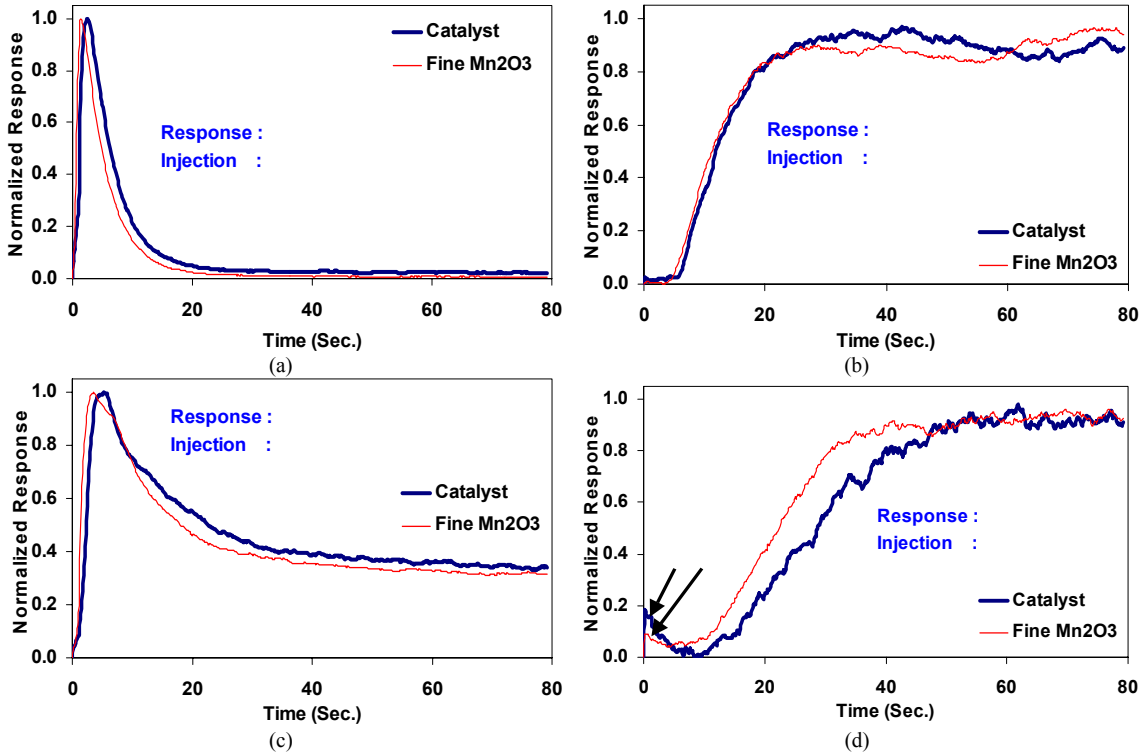


Figure 16. Comparison of tracer responses for $Mn_2O_3$ and catalyst tracer injections (Sidewall, Middle) for Run 16.7.

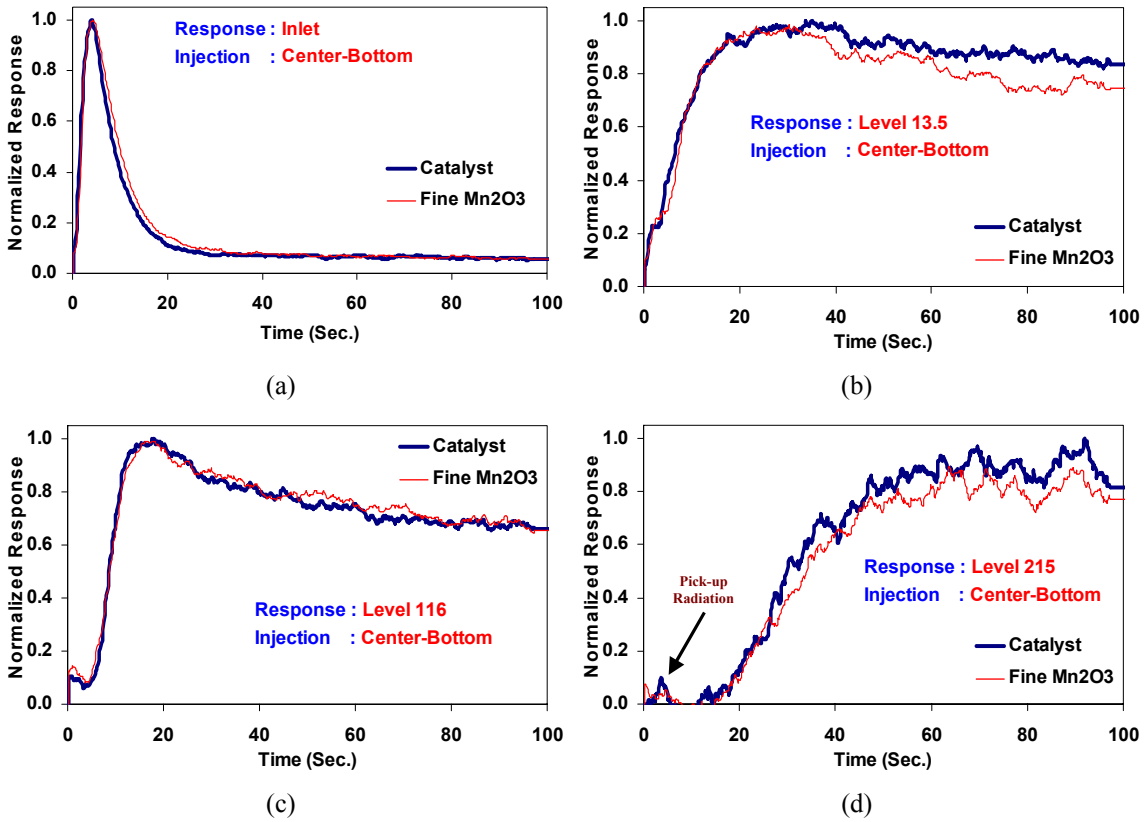


Figure 17. Comparison of tracer responses for $Mn_2O_3$ and catalyst tracer injections (Center, Bottom) for Run 16.7.

## 2.4. Liquid Mixing Model

The radioactive tracer data reported above at the two operating conditions of Table 3 has been analyzed using the liquid (slurry) (Degaleesan, 1997) and gas-liquid (slurry) (Gupta *et al*., 2001[a]) mixing and recirculation models developed at CREL. In this report, the liquid (slurry) mixing model developed at CREL (Degaleesan, 1997; Gupta *et al*., 2001[a]) is extended to account for the slurry recycle from the middle portion of the reactor. As discussed by Gupta (2002), the above models originally had incorrect boundary conditions which were corrected in the present work (Appendix B). Predictions from the developed model are compared with the $Mn_2O_3$ "liquid-like" tracer responses for Run 16.7. Since wrong "liquid-like" tracer was employed for Run 16.6, for this run

the tracer responses measured using the catalyst tracer are compared with the predictions from the liquid mixing model. In an earlier study on analysis of tracer data obtained at the AFDU, LaPorte during methanol synthesis, the shortcomings of the Axial Dispersion Model (ADM) were discussed (Degaleesan *et al.*, 1996[b]). Therefore, the FT-IV tracer data has not been analyzed using the ADM.

As mentioned earlier, Figure 7 shows the schematic of the reactor layout with syngas sparged into the bottom of the column where the slurry recycle stream is introduced also. The slurry exits the reactor approximately in the middle portion and flows to a filtration unit where the liquid product is separated from the slurry, which gets recycled back into the reactor. From the responses obtained from the detectors placed at the slurry outlet and at the slurry recycle streams, a lag time of approximately 60 seconds was observed for all tracer injections, which is to be expected since the superficial slurry velocity during the tracer tests was almost identical (0.727 cm/s for Run 16.6 and 0.722 cm/s for Run 16.7). Since the measured liquid and catalyst tracer responses do not appear to reach steady state before 100-120 seconds from the start of tracer injection, one cannot ignore the effect of the slurry recycle, having an approximate recycle-loop residence time of 60 seconds as mentioned above, on the tracer responses simulated using the mechanistic liquid mixing models. To account for the slurry recycle, the mixing model (Degaleesan, 1997) is extended and modified by modeling the slurry recycle loop as a plug flow section with a residence time of 60 seconds. Moreover, it was observed that the experimental response of the product (wax) outlet detector was relatively weak implying that there was insignificant loss of the tracer to the product outlet stream. Therefore, the loss of tracer to the product stream has not been considered in the model by assuming complete recycle of the tracer. Figure 18 shows the details of the reactor compartmentalization resulting from the phenomenological picture presented above.

It is to be noted that in the upper portion of the column above the slurry outlet, there is no net flow of the slurry; while in the bottom portion, there exists a net up-flow. Therefore, the reactor model parameters obtained from a sub-model for computing the radial profile of the liquid/slurry axial velocity (Gupta *et al*., 2001[a]), are estimated separately for the upper and lower portions of the column. The reactor

compartmentalization sketched in Figure 18 results in a coupled system of two ODEs and two PDEs for the two end CSTs (Continuous Stirred Tanks) and the two well-developed flow zones, respectively. The cell location, at which the slurry exits, patches the different model parameters for the lower and bottom portions of the reactor by mass balance considerations. The tracer concentration in the recycle slurry at the reactor inlet is taken to be the slurry outlet concentration with a time lag of 60 seconds. The resulting set of equations, with appropriate boundary and initial conditions, is solved by a completely implicit finite-difference scheme. Details of the solution procedure and the sub-model equations are presented by Gupta (2002) and Gupta *et al*., (2001[a]). The coupled system of ODEs and PDEs resulting from domain splitting is presented below.

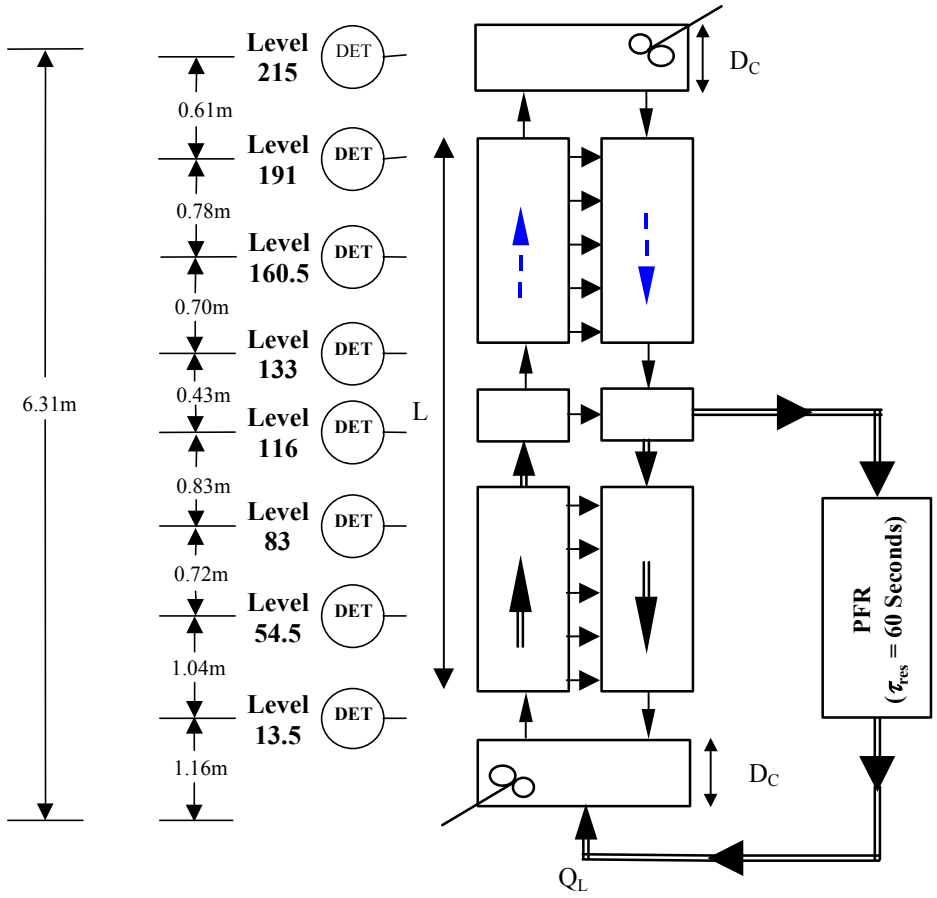


Figure 18. Schematic of the model compartmentalization.

## 2.5. Model Equations for Liquid Mixing as a Result of Domain-Splitting

***Liquid in the Distributor Zone***

$$\frac{dC_{la}}{dt}=\left\{\begin{array}{l}\dfrac{U_L}{\bar{\varepsilon}_l\,\phi_{in}\,D_C}C_{l,in}-\dfrac{U_L}{\bar{\varepsilon}_l\,\phi_{in}\,D_C}C_{la}\\ +\dfrac{\bar{\varepsilon}_{l1,BSE}}{\bar{\varepsilon}_l\,\phi_{in}\,D_C}\dfrac{r_{BSE}^{'\,2}}{R^2}\overline{D}_{xx1}\left.\dfrac{\partial C_{l1}}{\partial x}\right|_{x=0}+\dfrac{\bar{\varepsilon}_{l2,BSE}}{\bar{\varepsilon}_l\,\phi_{in}\,D_C}\dfrac{\left(R^2-r_{BSE}^{'\,2}\right)}{R^2}\overline{D}_{xx2}\left.\dfrac{\partial C_{l2}}{\partial x}\right|_{x=0}\end{array}\right\} \tag{15}$$

***Fully-Developed Zone of Up-flowing Liquid below Slurry Exit (BSE)***

$$\frac{\partial C_{l1}}{\partial t}=\left\{\overline{D}_{xx1}\frac{\partial^2 C_{l1}}{\partial x^2}-\bar{u}_{l1,BSE}\frac{\partial C_{l1}}{\partial x}-\frac{4\left(\overline{D}_{rr}\varepsilon_l\right)_{r=r_{BSE}^{'}}}{r_{BSE}^{'}R\bar{\varepsilon}_{l1,BSE}}\left(C_{l1}-C_{l2}\right)\right\} \tag{16}$$

***Fully-Developed Zone of Down-flowing Liquid below Slurry Exit (BSE)***

$$\frac{\partial C_{l2}}{\partial t}=\left\{\overline{D}_{xx_2}\frac{\partial^2 C_{l2}}{\partial x^2}+\bar{u}_{l2,BSE}\frac{\partial C_{l2}}{\partial x}+\frac{4r_{BSE}^{'}/R}{R^2-r_{BSE}^{'\,2}}\frac{\left(\overline{D}_{rr}\varepsilon_l\right)_{r=r_{BSE}^{'}}}{\bar{\varepsilon}_{l2,BSE}}\left(C_{l1}-C_{l2}\right)\right\} \tag{17}$$

***Fully-Developed Zone of Up-flowing Liquid above Slurry Exit (ASE)***

$$\frac{\partial C_{l1}}{\partial t}=\left\{\overline{D}_{xx1}\frac{\partial^2 C_{l1}}{\partial x^2}-\bar{u}_{l1,ASE}\frac{\partial C_{l1}}{\partial x}-\frac{4\left(\overline{D}_{rr}\varepsilon_l\right)_{r=r_{ASE}^{'}}}{r_{ASE}^{'}R\bar{\varepsilon}_{l1,ASE}}\left(C_{l1}-C_{l2}\right)\right\} \tag{18}$$

***Fully-Developed Zone of Down-flowing Liquid above Slurry Exit (ASE)***

$$\frac{\partial C_{l2}}{\partial t}=\left\{\overline{D}_{xx_2}\frac{\partial^2 C_{l2}}{\partial x^2}+\bar{u}_{l2,ASE}\frac{\partial C_{l2}}{\partial x}+\frac{4r_{ASE}^{'}/R}{R^2-r_{ASE}^{'\,2}}\frac{\left(\overline{D}_{rr}\varepsilon_l\right)_{r=r_{ASE}^{'}}}{\bar{\varepsilon}_{l2,ASE}}\left(C_{l1}-C_{l2}\right)\right\} \tag{19}$$

***Liquid in the Disengagement Zone***

$$\frac{dC_{lb}}{dt}=\left\{-\frac{\bar{\varepsilon}_{l1,ASE}}{\bar{\varepsilon}_l\,\phi_{out}\,D_C}\frac{r_{ASE}^{'\,2}}{R^2}\overline{D}_{xx1}\left.\frac{\partial C_{l1}}{\partial x}\right|_{x=L}-\frac{\bar{\varepsilon}_{l2,ASE}}{\bar{\varepsilon}_l\,\phi_{out}\,D_C}\frac{\left(R^2-r_{ASE}^{'\,2}\right)}{R^2}\overline{D}_{xx2}\left.\frac{\partial C_{l2}}{\partial x}\right|_{x=L}\right\} \tag{20}$$

***Initial Conditions***

The initial conditions in all zones of the reactor are those of zero initial concentration of the tracer which is introduced at time $t = 0^+$ at the tracer injection point.

$t = 0;\ C_{la} = C_{lb} = C_{l1} = C_{l2} = 0$

$x = x_{inj}$, $C_{l1} = C_{L,inj}$ for center injection OR $C_{l2} = C_{L,inj}$ for sidewall injection (21)

For simulating the catalyst and liquid-like tracer responses for the tracer runs at AFDU, LaPorte, the experimental ***molar input rate*** of the tracer has been simulated as a product of a constant (arbitrary) concentration ($C_{L,inj}$) and a volumetric flow rate ($Q_{L,inj}$). This volumetric flow rate of the tracer is time-dependent and is approximated as a Gaussian function with a tail as shown in Equation 22 (Degaleesan, 1997). The parameters of this functional form are obtained by curve fitting the experimentally measured input tracer response measured by a scintillation detector placed on the tracer injection port.

$$t \rightarrow 0^{+},\ t > 0; \quad Q_{L,inj} = \frac{\psi}{\sqrt{2\pi\kappa t}} exp\left\{-\frac{(\delta-\chi)^2}{2\kappa t}\right\} \tag{22}$$

***Boundary conditions for the fully developed region***

As mentioned earlier, it is tempting to use Danckwerts' boundary conditions at inlet and exit. However, these are not correct in this particular compartmentalization of the reactor as is discussed in further detail in Appendix B. The reader is referred to Appendix B for a comparison of the effect of the boundary conditions on the predicted tracer responses. For the cases considered in this study, the differences between the simulated results from the two boundary conditions are negligible.

The bottom of the fully developed flow zone is the boundary with the CSTR representing the distributor zone, whereas the top of the fully developed flow zone is the boundary with the CSTR representing the disengagement zone. The correct boundary conditions to use are Dirichlet type and are shown below.

***Up-flow section of the liquid***

$$C_{l1}\,|_{x=0} = C_{la} \tag{23}$$

$$C_{l2}\,|_{x=0} = C_{la} \tag{24}$$

***Down-flow section of the liquid***

$$C_{l1}\,|_{x=L} = C_{lb} \tag{25}$$

$$C_{l2}\,|_{x=L} = C_{lb} \tag{26}$$

***Numerical Treatment of the Slurry Exit Point***

The basis for the mathematical treatment of the slurry exit point is represented in the sketch below, where the index "i" represents the axial slurry exit location in the up-flow region, and "j" that in the down-flow region.

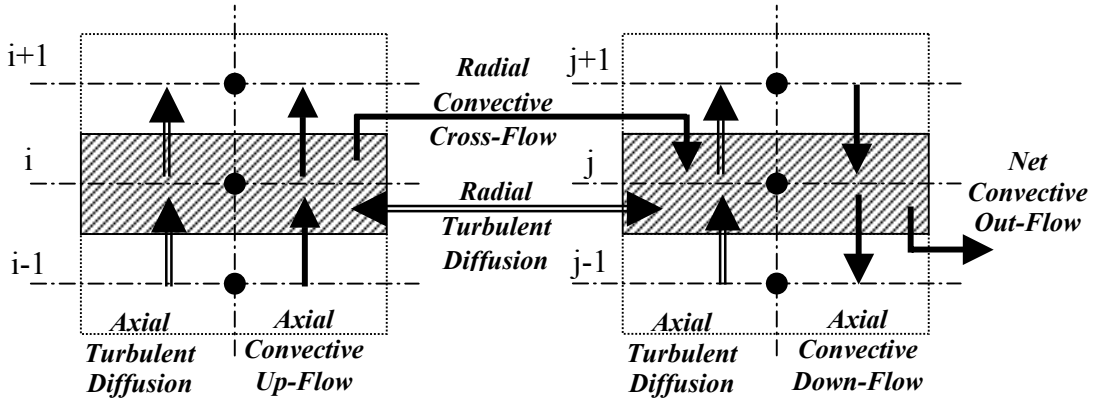


The following equations result from the above representation of the elemental mass balance for the slurry exit node in the up-flow and down-flow regions, respectively. Essentially, the above schematic implies that the difference in the net axial convective plus diffusive flux between the up-flow and the down-flow zones, when subtracted from the net radial flux gives the balance that accounts for the slurry exit concentration and accumulation in the cell representing the slurry exit node.

$$\frac{\partial C_{l1,i}}{\partial t} = \left\{ \overline{D}_{xx1} \frac{\partial^2 C_{l1}}{\partial x^2}\bigg|_i - \frac{\overline{u}_{l1,BSE}}{\Delta x} C_{l1,i} + \frac{\overline{u}_{l1,BSE}}{\Delta x} C_{l1,i-1} - \frac{4\left(\overline{D}_{rr}\varepsilon_l\right)_{r=r'_{BSE}}}{r'_{BSE} R \bar{\varepsilon}_{l1,BSE}} \left(C_{l1,i} - C_{l2,j}\right) \right\} \tag{27}$$

$$\frac{\partial C_{l2,j}}{\partial t}=\left\{\begin{array}{l}\overline{D}_{xx2}\left.\dfrac{\partial^2 C_{l2}}{\partial x^2}\right|_j+\dfrac{4r'_{BSE}/R}{R^2-r'^{\,2}_{BSE}}\dfrac{\left(\overline{D}_{rr}\varepsilon_l\right)_{r=r'_{BSE}}}{\bar{\varepsilon}_{l2,BSE}}\left(C_{l1,i}-C_{l2,j}\right)\\ +\dfrac{\bar{u}_{l2,ASE}\ \bar{\varepsilon}_{l2,ASE}\left(R^2-r'^{\,2}_{ASE}\right)}{\Delta x\ \bar{\varepsilon}_{l2,BSE}\left(R^2-r'^{\,2}_{BSE}\right)}C_{l2,j+1}-\left[\dfrac{\bar{u}_{l2,BSE}}{\Delta x}+\dfrac{U_L}{\Delta x\ \bar{\varepsilon}_{l2,BSE}\left(R^2-r'^{\,2}_{BSE}\right)}\right]C_{l2,j}\\ +\dfrac{\left(\bar{u}_{l1,BSE}\ \bar{\varepsilon}_{l1,BSE}\,r'^{\,2}_{BSE}-\bar{u}_{l1,ASE}\ \bar{\varepsilon}_{l1,ASE}\,r'^{\,2}_{ASE}\right)}{\Delta x\ \bar{\varepsilon}_{l2,BSE}\left(R^2-r'^{\,2}_{BSE}\right)}C_{l1,i}\end{array}\right\} \quad (28)$$

In the above set of Equations (15) to (28), $\overline{D}_{xx}$ and $\overline{D}_{rr}$ are the average eddy diffusivities from CARPT, which are estimated from a scale-up methodology developed by Degaleesan (1997) (refer to Appendix A).

## 2.6. Comparison of Experimental Liquid/Catalyst Tracer Responses with Simulation Results

Simulations were carried out using the liquid mixing model for the operating conditions of Run 16.6 listed in Table 3. Other parameters that were needed to predict liquid and catalyst tracer responses as well as the gas tracer responses presented in Section 3 are listed in Table 4. As was shown in earlier studies (Gupta, 2002; Gupta *et al*., 2001[a]; Gupta *et al*., 2001[b]), since Henry's constant has the greatest effect on the predicted gas tracer responses, a range of values for this parameter was investigated. The sub-model for parameter estimation (Gupta *et al*., 2001[a]) requires as input the radial gas holdup profile, which is given by Equation 10. In this equation, the parameter $\bar{\varepsilon}_G$ is the volume averaged mean gas holdup, measured using the Differential Pressure (DP). The parameter "*m*" is the exponent while "*c*" is the parameter that allows for a non-zero holdup at the wall. Earlier in this section, the reasons for fixing the parameter "*m*" as 2 were discussed in view of the suggestions from Degaleesan (1997). Once "*m*" is fixed, "*c*" is readily estimated using the chordal average holdup obtained using Nuclear Density Gauge (NDG) measurements (Equation 11). It was pointed out earlier that Table 3 reveals a peculiar situation of higher measured average gas holdup $\left(\bar{\varepsilon}_g\big|_{DP}\right)$ in Run 16.6,

executed at lower superficial gas velocity, than in the Run 16.7 conducted at higher $U_g$. Since the pressure and temperature were essentially the same in the two runs, this implies that these conditions are close to transition between bubbly and churn-turbulent flow. In the transition zone, which is known to occur at gas superficial velocities of 3-6 cm/s in water at atmospheric pressure and at much higher gas superficial velocities at elevated pressures, different overall gas holdups are frequently observed and poor reproducibility or multiple holdup values have been reported. This also means that meaningful interpretation of the effect of gas superficial velocity on liquid or gas mixing based on Runs 16.6 and 16.7 is difficult, if not impossible, since the two runs likely did not experience the same flow regime.

Table 4. Input parameters for the liquid and gas mixing models.

| **Input Parameter** | **Run 16.6** | **Run 16.7** |
|---|---|---|
| Radius of the reactor, $R_C$ (cm) | 28.6 | 28.6 |
| Height of Dispersed Media (cm) | 631 | 633 |
| Temperature ($^o$K) | 532.0 | 534.2 |
| Pressure (MPa) | 5 | 5 |
| Molecular Weight of Gas (g/mole) | 16.99 | 18.09 |
| $\rho_G$ (gm/cm$^3$) | 0.0192 | 0.0203 |
| $\rho_{SL}$ (gm/cm$^3$) | 0.795 | 0.824 |
| $\mu_{SL}$ (Poise) | 0.025 | 0.025 |
| $\sigma_{SL}$ (dyne/cm) | 13 | 13 |
| Inlet Superficial Gas Velocity (cm/s) | 12.81 | 18.23 |
| Outlet Superficial Gas Velocity (cm/s) | 9.89 | 15.21 |
| Average Superficial Gas Velocity (cm/s) | 11.35 | 16.72 |
| Liquid (Slurry) Superficial Velocity (cm/s) | 0.727 | 0.722 |
| $\bar{\varepsilon}_G$ | 0.494 | 0.464 |
| $m$ | 2 | 2 |
| $c$ | 0.351 | 0.435 |
| $D_{lm,\ Argon}$ (cm$^2$/s) | 4.41x10$^{-5}$ | 4.41x10$^{-5}$ |
| Henry's Constant, $H = \left[\left(C_{Ar}\right)_{Liq.} / \left(C_{Ar}\right)_{Gas}\right]_{Equi.}$ | 0, 0.15, 0.248*, 0.35 | 0, 0.15, 0.245*, 0.35 |

Table 5 lists the parameters computed by the solution of the sub-model equations for predicting liquid recirculation. Since the current model does not handle changing superficial gas velocity due to reaction along the reactor length, a sensitivity analysis of the computed parameters was in order. Thus, for both Run 16.6 and Run 16.7, the model parameters have been computed using the inlet, outlet and average superficial gas velocities. From Table 5, one can see that none of the ***parameters of the liquid mixing model*** are affected by a change in the gas superficial velocity. This is due to the fact that the only parameters affecting liquid recirculation are the radial gas holdup profile and the closure for liquid turbulence. Since both of these are assumed to be independent of the changing superficial gas velocity along the reactor length, the computed liquid recirculation velocities as well as the eddy diffusivities show no dependence on superficial gas velocity given a non-varying gas holdup distribution. In actuality, however, there is a finite variation in the gas holdup along the reactor length that will cause the model parameters to vary from inlet to exit. It should be pointed out though that a change in superficial gas velocity would cause a change in the ***parameters of the gas-mixing model***.

Figures 19 and 20 show the comparison of the simulation results with experimental data for sidewall-middle and center-bottom injections, respectively. One can see from Figure 19 that the model predictions for the sidewall-middle injection of the catalyst tracer are distinctly different from the experimental responses. The reason for this significant deviation is the fact that the model assumes a well-developed one-dimensional flow in the region of slurry exit, which obviously is not the case. However, this approximation in modeling the slurry exit is not met when the tracer is injected close to the axial location of the slurry outlet, which happens to be the case with the tracer injected into the reactor sidewall. Therefore, if one observes the comparison of the simulated and experimental responses for the tracer injection into the reactor center–bottom, shown in Figure 20, one finds reasonable agreement, especially in the fully developed portion of the flow. In this case, the tracer has sufficient time to mix radially before encountering the slurry outlet stream, and the three-dimensionality of the flow near the slurry outlet does not significantly affect the measured tracer responses.

Table 5. Computed model parameters for the liquid mixing model.

| Parameter | Run 16.6 | | | Run 16.7 | | |
|---|---|---|---|---|---|---|
| **$U_G$ (cm/s)** | **12.8** | **9.89** | **11.4** | **18.2** | **15.2** | **16.7** |
| $\overline{\varepsilon}_g$ | 0.494 | 0.494 | 0.494 | 0.464 | 0.464 | 0.464 |
| $U_{ge}$ (cm/s) | 86.4 | 86.4 | 86.4 | 74.9 | 74.9 | 74.9 |
| $\overline{\varepsilon}_{l1,BSE}$ | 0.458 | 0.458 | 0.458 | 0.478 | 0.478 | 0.478 |
| $\overline{\varepsilon}_{l2,BSE}$ | 0.564 | 0.564 | 0.564 | 0.607 | 0.607 | 0.607 |
| $\overline{\varepsilon}_{l1,ASE}$ | 0.457 | 0.457 | 0.457 | 0.476 | 0.476 | 0.476 |
| $\overline{\varepsilon}_{l2,ASE}$ | 0.562 | 0.562 | 0.562 | 0.605 | 0.605 | 0.605 |
| $\overline{u}_{l1,BSE}$ (cm/s) | 33.6 | 33.6 | 33.6 | 36.2 | 36.2 | 36.2 |
| $\overline{u}_{l2,BSE}$ (cm/s) | 30.1 | 30.1 | 30.1 | 32.2 | 32.2 | 32.2 |
| $\overline{u}_{l1,ASE}$ (cm/s) | 33.1 | 33.1 | 33.1 | 35.7 | 35.7 | 35.7 |
| $\overline{u}_{l2,ASE}$ (cm/s) | 30.7 | 30.7 | 30.7 | 32.8 | 32.8 | 32.8 |
| $r'_{BSE}/R_C$ | 0.739 | 0.739 | 0.739 | 0.742 | 0.742 | 0.742 |
| $r'_{ASE}/R_C$ | 0.730 | 0.730 | 0.730 | 0.734 | 0.734 | 0.734 |
| $\overline{D}_{xx_1}\big\vert_{BSE}$ (cm$^2$/s) | 624 | 624 | 624 | 601 | 601 | 601 |
| $\overline{D}_{xx_2}\big\vert_{BSE}$ (cm$^2$/s) | 606 | 606 | 606 | 573 | 573 | 573 |
| $\overline{D}_{xx_1}\big\vert_{ASE}$ (cm$^2$/s) | 604 | 604 | 604 | 585 | 585 | 585 |
| $\overline{D}_{xx_2}\big\vert_{ASE}$ (cm$^2$/s) | 624 | 624 | 624 | 590 | 590 | 590 |
| $\overline{D}_{rr}\big\vert_{No\ Int.}$ (cm$^2$/s) | 153 | 153 | 153 | 146 | 146 | 146 |
| $\overline{D}_{rr}\big\vert_{With\ Int.}$ (cm$^2$/s) | 60 | 60 | 60 | 55 | 55 | 55 |

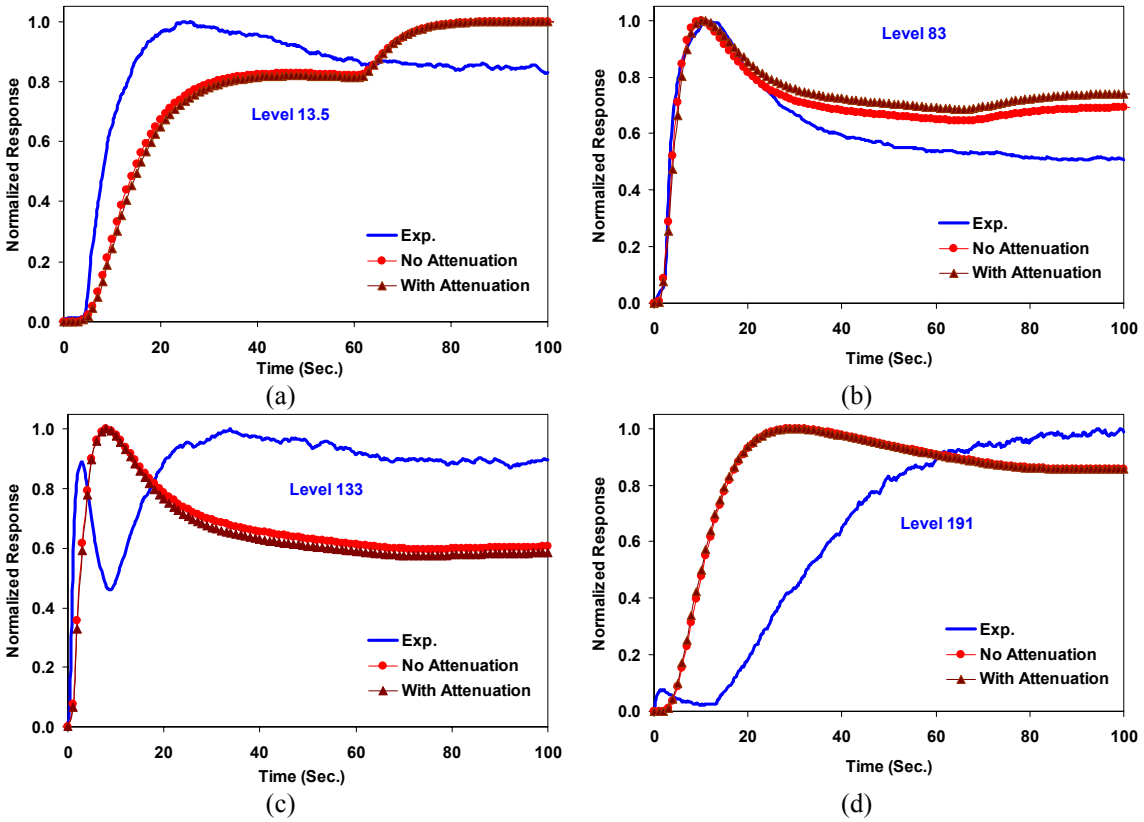


Figure 19. Comparison of experimental and simulated tracer responses for Run 16.6 (Tracer: - Catalyst; Injection Pt.: - Sidewall-Middle).

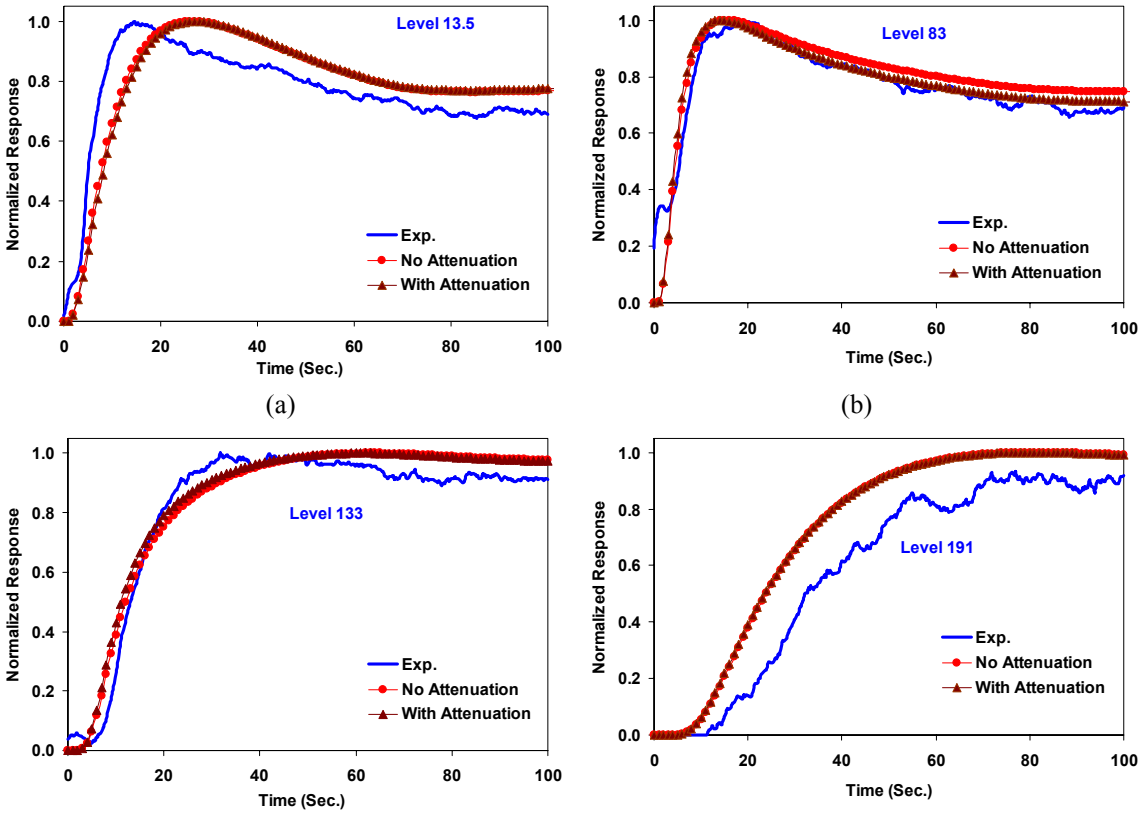


Figure 20. Comparison of experimental and simulated tracer responses for Run 16.6 (Tracer: - Catalyst; Injection Pt.: - Center-Bottom).

The comparison of the simulated and experimental results for levels 191 and 215 inches (refer to Appendix C), as referenced on the outside tape, indicates that the simulated tracer responses seem to arrive earlier than the experimental ones. There could be several possibilities which can cause the experimental tracer responses to be detected later at higher column elevations. They are:

1. Existence of a foamy structure at the top of the column, which would prevent the tracer from easily accessing the slurry fluid elements in that zone of the reactor.
2. A significant fluctuation of the gas-slurry interface.
3. Reduction in the superficial gas velocity, $U_G$, through the upper portion of the column as some amounts of gas leave the column via the slurry exit. This gas is

actually re-introduced into the reactor close to the vapor headspace after going through a gas- slurry separator (degasser). However, this probably results in lowering the superficial gas velocity and consequently the gas holdup in the upper portion of the column. Additionally, the axial and radial eddy diffusivities used in the model simulations are based on a constant (mean) $U_G$. Therefore, the model parameters could be slightly over-estimated for the upper portion of the column and could explain the earlier arrival of the simulated tracer responses, especially at levels 191 and 215. Unfortunately, there is no readily available information to estimate how much gas bypasses through the degasser.

4. The catalyst tracer particles are more representative of the solids phase while the simulations represent the slurry. There may be some slip between solids and liquid, which could cause the measured responses to rise slower than predicted liquid ("slurry") response of solids tracer.

This model has been further employed to simulate the tracer responses for Run 16.7 for both the liquid-like (fine $Mn_2O_3$ powder in heat transfer oil) and catalyst tracers. These results are presented next along with the comparison of the model simulations with experimentally obtained responses. Figures 21 and 22 show the comparison of the simulation results with experimental data for sidewall-middle and center-bottom injections, respectively, for the catalyst tracer. This comparison reveals that the dominant time constant is captured rather well by the model at all axial detector locations. The agreement between model predictions and data is somewhat better for the center-bottom injection (Figure 22) than for sidewall-middle injection (Figure 21) since for the former the assumptions of the model are better satisfied (more liquid radial and azimuthal mixing at the location of tracer injection). It should be recalled that this model treats the slurry as a pseudo-homogeneous mixture so that the response of the catalyst tracer is modeled as the liquid (slurry) response.

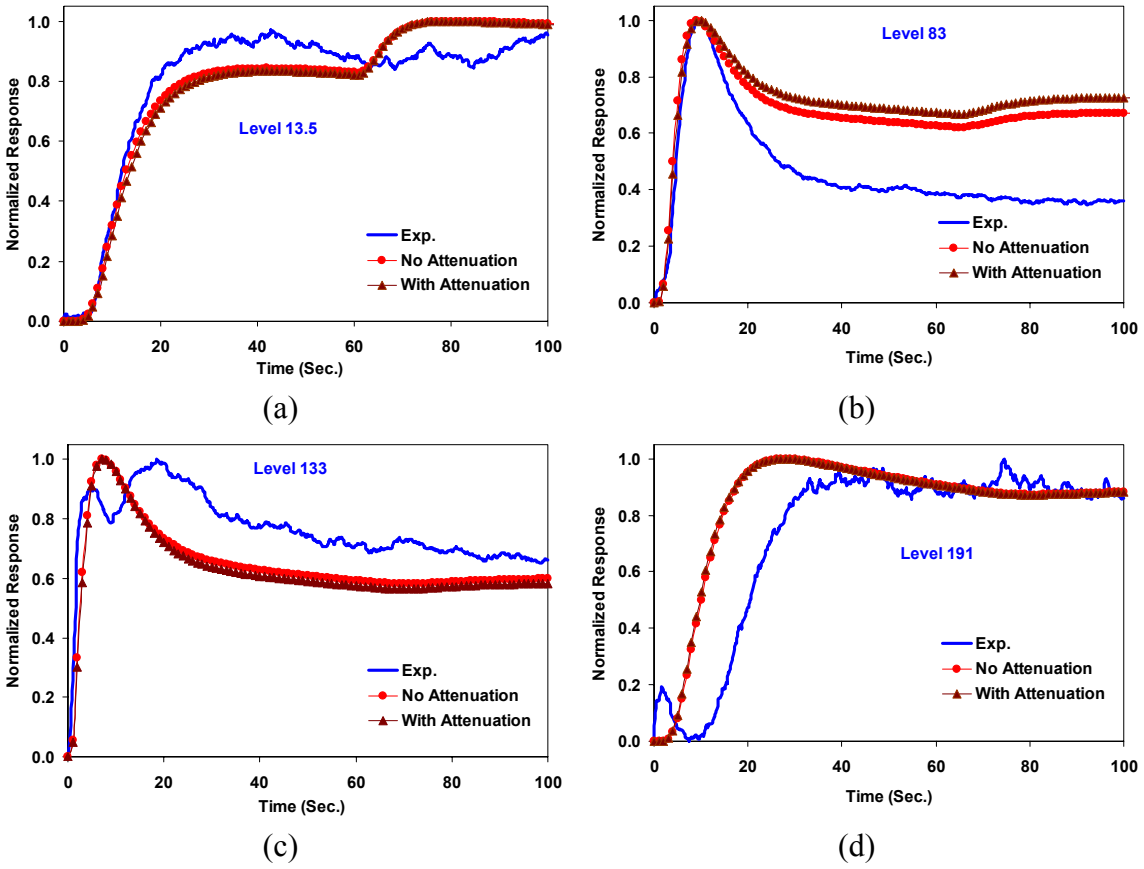


Figure 21. Comparison of experimental and simulated tracer responses for Run 16.7 (Tracer: - Catalyst; Injection Pt.: - Sidewall-Middle).

Figures 23 and 24 show the comparison of the model predictions for the slurry response (same as in Figures 21 and 22) and the experimental data for the fine $Mn_2O_3$ tracer that should be fully capable of following the liquid. In general the agreement between data and predictions is even better. One can also see from Figures 21 and 23 that the model predictions for the sidewall-middle injection, both for the catalyst as well as of $Mn_2O_3$ tracer, are in fair agreement with the experimental responses as far as the overall mixing time are concerned. This is especially true for the levels 54.5, 83, 116, 133, and 160.5 inches with reference to zero on the outside tape. It should be recalled that this was not the case for the tracer responses obtained for sidewall injections under conditions of Run 16.6. It seems that the higher superficial gas velocity employed during Run 16.7

results in better radial mixing of the tracer even for the sidewall-middle injection, thus satisfying better the model assumptions. However, even though the agreement is better than for Run 16.6, the proximity of the tracer injection point to the slurry outlet still cannot be completely captured by the employed model. ***Consequently, this tracer injection point is not recommended for any future studies with net slurry recycle from the middle portion of the reactor***.

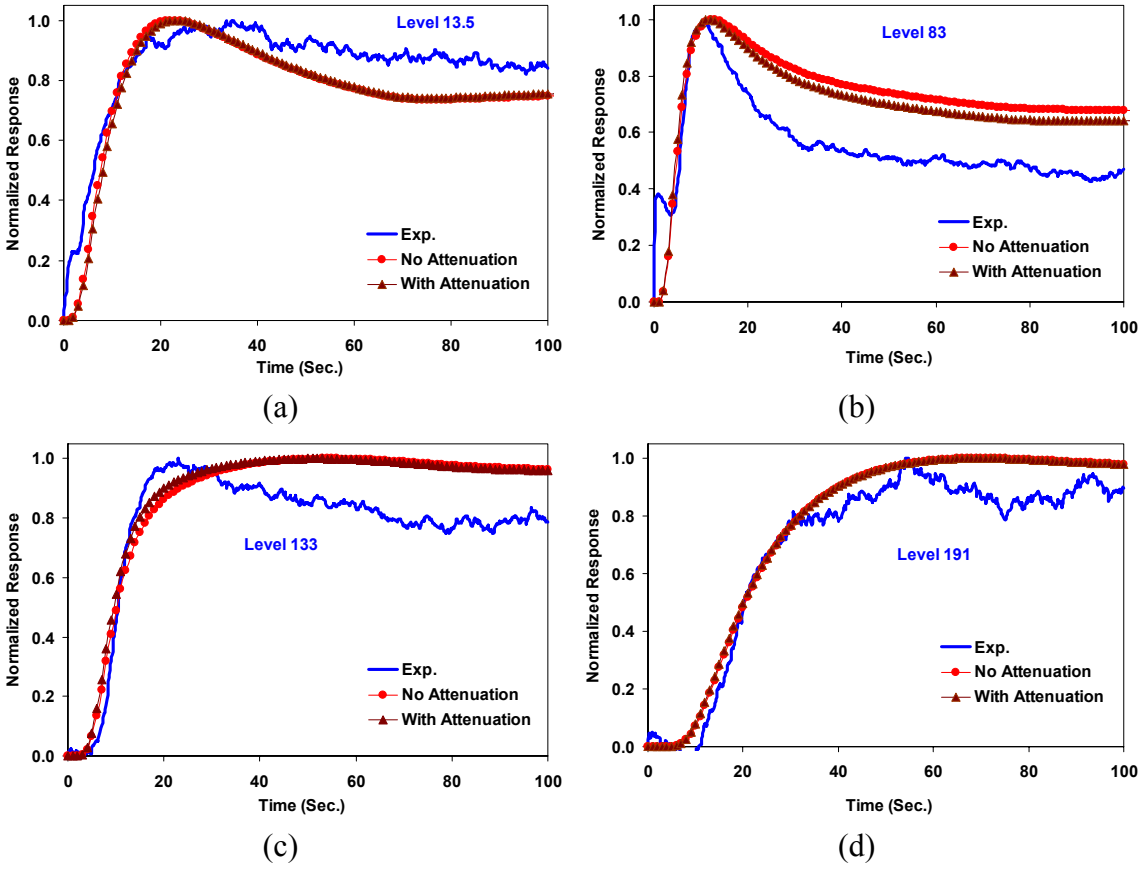


Figure 22. Comparison of experimental and simulated tracer responses for Run 16.7 (Tracer: - Catalyst; Injection Pt.: - Center-Bottom).

When one examines the comparison of the simulated tracer responses and experimental ones for the center-bottom injection (both for the catalyst as well as for the $Mn_2O_3$ fine tracer), one finds better agreement between data and model predictions as

compared to the results for the sidewall-middle injection. This is not surprising since for the center-bottom injection, the tracer has sufficiently longer time to disperse radially before encountering the slurry exit as compared to the sidewall-middle injection. Additionally, the radial mixing for Run 16.7 is enhanced as compared to Run 16.6 due to a higher superficial gas velocity. While comparing the tracer responses with simulation results for the catalyst and fine $Mn_2O_3$ particles, one finds that the $Mn_2O_3$ particles seem to trace the liquid better, and consequently, one observes better agreement of $Mn_2O_3$ responses with simulation results as compared to catalyst responses.

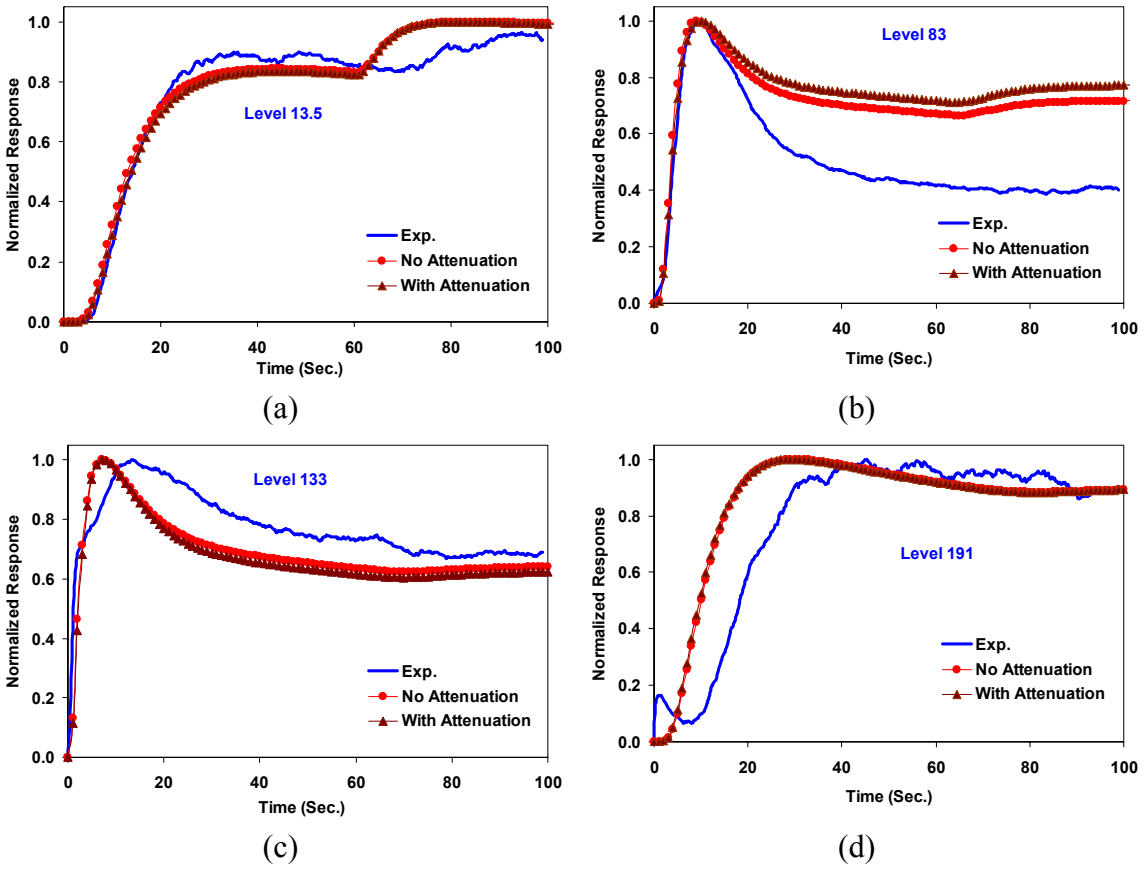


Figure 23. Comparison of experimental and simulated tracer responses for Run 16.7 (Tracer: - $Mn_2O_3$; Injection Pt.: - Sidewall-Middle).

As was observed for Run 16.6, again the comparison of the simulated responses and experimental data for levels of 191 and 215 inches (see Appendix C), as referenced on the outside tape, indicates that the simulated tracer responses arrive earlier than the experimental ones. As mentioned before, these discrepancies between the simulated and measured responses for the top portion of the reactor could result from existence of a foamy structure near the gas-liquid interface and/or from a lower effective superficial gas velocity through the upper portion of the column due to some gas bypassing via the slurry outlet line.

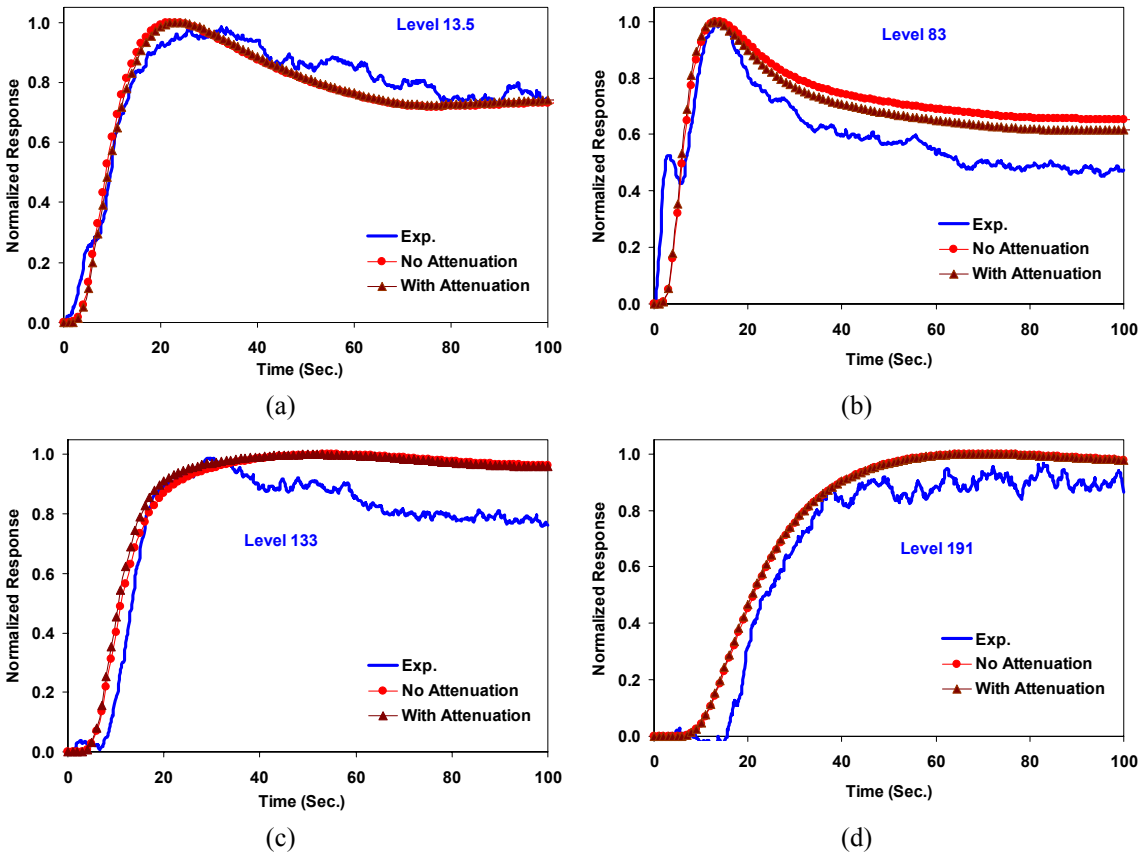


Figure 24. Comparison of experimental and simulated tracer responses for Run 16.7 (Tracer: - $Mn_2O_3$; Injection Pt.: - Center-Bottom).

In addition, the experimentally measured response at Level 133 in Figure 22 and 24 show a loss of tracer as this is very close to the location of the slurry exit. It is also

possible that around the slurry exit location there are internals/flanges that obstruct the field of view of detectors at that level and result in a lower count-rate. However, if this were the case, then the count-rate would be lower at all times and would not explain the observed trend. Thus, the observed trend is most likely the result of a preferential loss of tracer.

For all the simulation results in Figure 19 to 22 above, the radial eddy diffusion coefficients used to model cross mixing between the up-flow and down-flow liquid zones were estimated based on the scale-up procedure of Degaleesan (1997) as presented in Appendix A. Following her methodology, the estimated radial eddy diffusivities were further scaled down to account for the presence of the internal heat exchanger tubes. Unfortunately, since details on evaluating the shape of the scaled-down radial profile of the $D_{rr}$ due to the presence of internals are not clearly spelled out in the protocol suggested by Degaleesan (1997), a visual approximation of the shape of her profile was used in this study.

In addition to the comparison of the simulated responses with the experimental ones, the above figures also show the comparison of the simulated responses with and without accounting for radiation attenuation by the Beer-Lambert's law as discussed by Gupta (2002). In general, the differences between the simulated responses with and without attenuation are minimal indicating that the radial uniformity in the distribution of the tracer is achieved on a much shorter time scale as compared to the time-scale at which the mixing in the axial direction occurs.

## 2.7. Parametric Sensitivity of Simulated Liquid/Catalyst Tracer Responses

As mentioned earlier, the simulated tracer responses are computed from model equations that require as inputs the gas holdup profile, a closure for liquid phase turbulence and an estimate of the radial eddy diffusion coefficient. Even though guidelines are available for choosing the above parameters, these are unfortunately empirically based. It is therefore important to explore the effect of these parameters on the change in trends of the simulated responses. For this purpose, the effect of three different gas holdup profiles, three different mixing length profiles (described by Gupta

(2002) in Chapter 6 of his thesis) and two different radial eddy diffusivities on the simulated responses at two detector levels (83 & 160.5 as measured on the outside tape) is presented below. The experiments chosen for this evaluation are

- Bottom-Center injection of Catalyst tracer for Run 16.6
- Bottom-Center injection of Catalyst tracer for Run 16.7
- Middle-Sidewall injection of $Mn_2O_3$ tracer for Run 16.7

The effect of the aforementioned parameters on the simulated responses for the above three experiments are presented in Figures 25 to 27 respectively. From these figures, it can be seen that the effect of the radial eddy diffusion coefficient on the predicted tracer responses is the most pronounced especially for responses resulting from tracer injections at the "preferred" bottom-center location (refer to Figures 25b and 26b). On the other hand, for the sidewall injection of the tracer, the effect of $D_{rr}$ on the simulated responses is smaller as compared to those resulting from the bottom-center injection. It is therefore important to consider the presence of internals for properly estimating the radial eddy diffusion coefficient that accounts for the radial cross mixing of the tracer. On the other hand, the effects of the mixing length and gas holdup profiles, though significant for some cases, do not indicate a clear choice for either of them across all conditions. Further, it appears that on the whole, a gas holdup profile with "m = 2" and the mixing length profile (ML-3), the original choices as model inputs, provide the best comparison of experiments with simulations.

In conclusion, the developed recirculation model, in spite of its simplicity, is successful in capturing the dominant transport time-scale in a complex three-phase multiphase flow accompanied by heat transfer and further complicated by the difficulties associated with interpretation of data from radiotracers. It is hoped that future advancements in understanding of the liquid phase turbulence and its interaction with gas holdup and bubble motion would be beneficial in improving the predictive capabilities of the developed model.

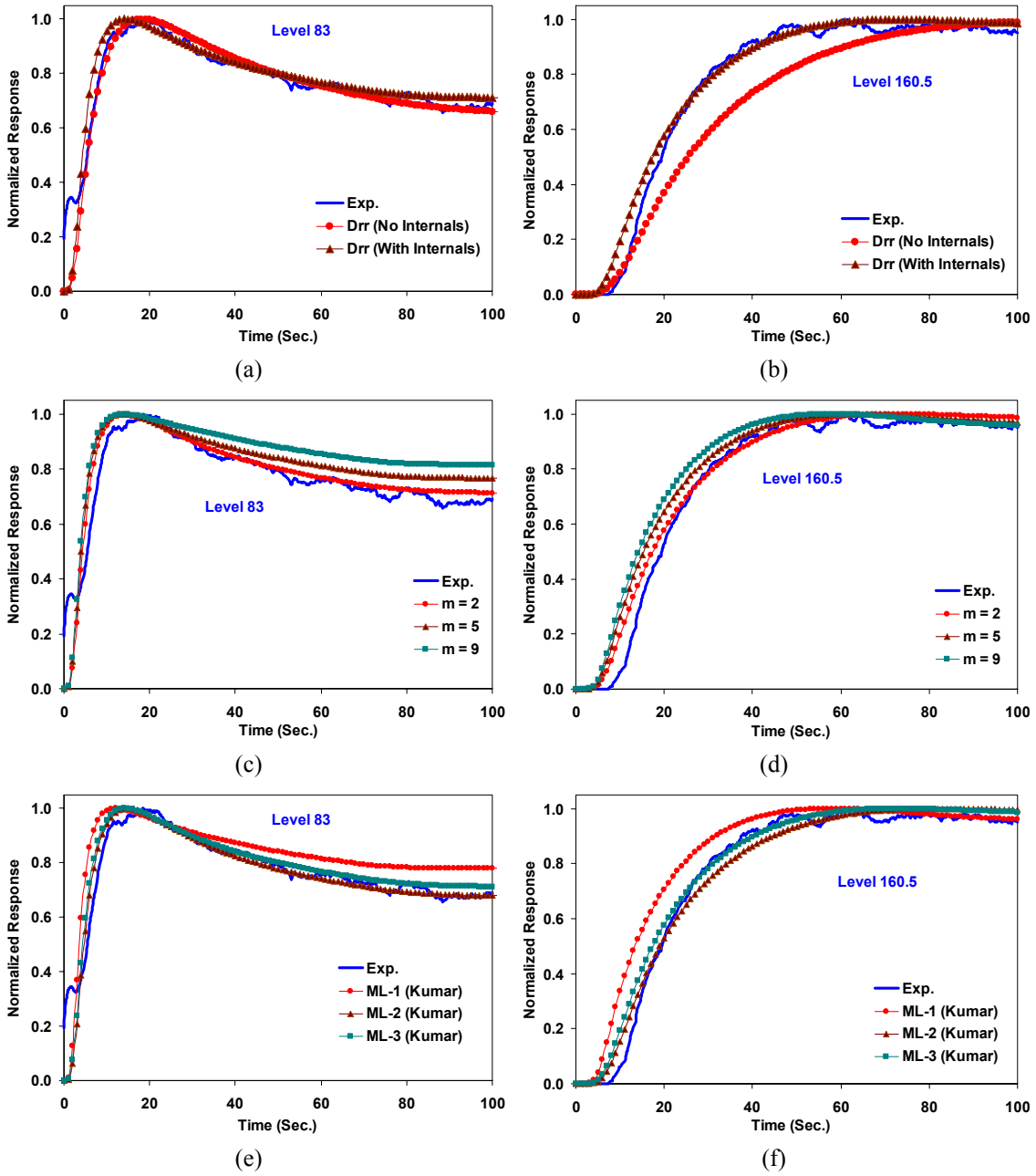


Figure 25. Parametric sensitivity of simulated tracer responses for Run 16.6 for Bottom-Center injection of catalyst tracer

a) - b) Effect of $D_{rr}$ c) - d) Effect of gas holdup profile

e) - f) Effect of mixing length profile

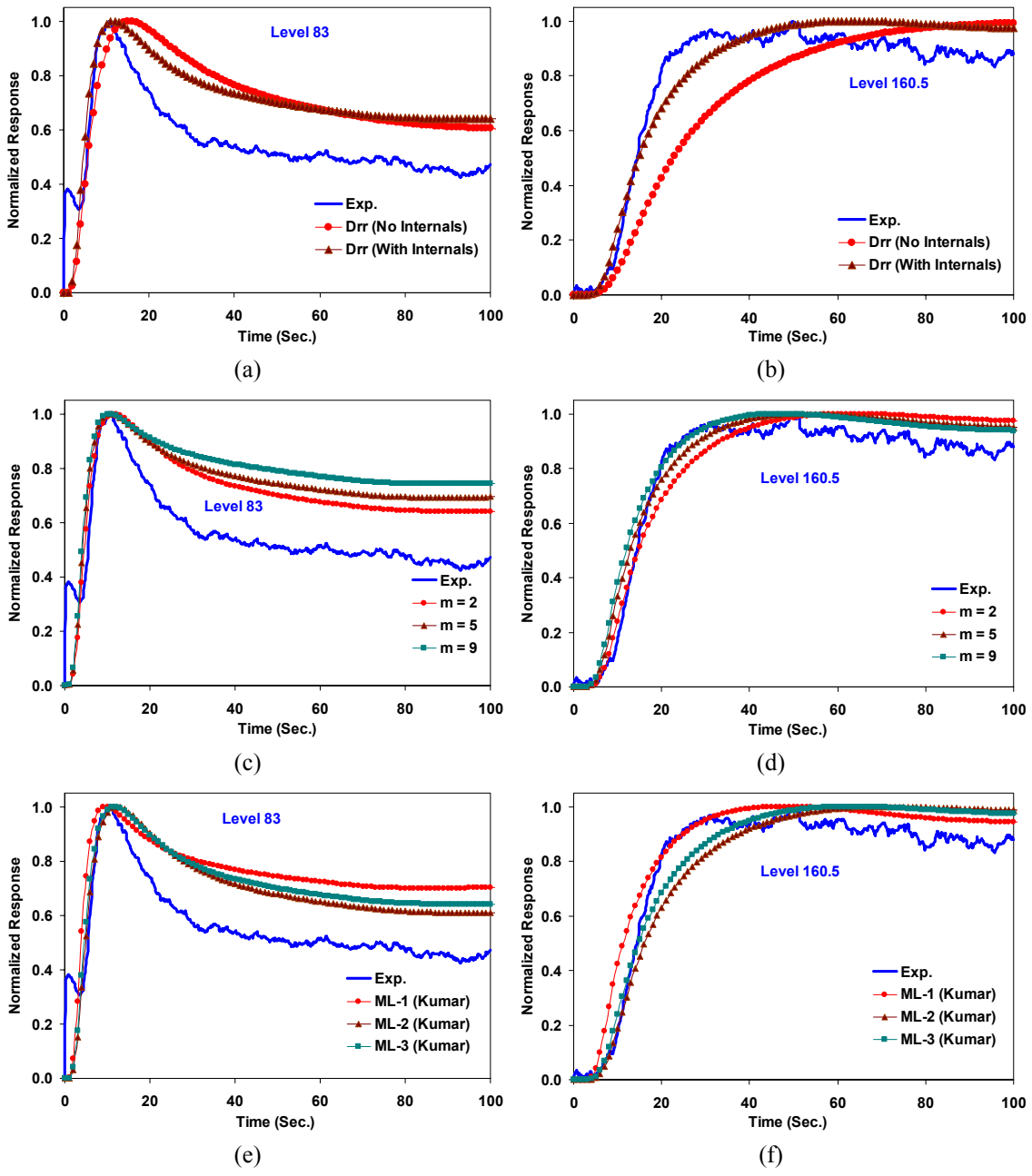


Figure 26. Parametric sensitivity of simulated tracer responses for Run 16.7 for Bottom-Center injection of catalyst tracer

a) - b) Effect of $D_{rr}$ c) - d) Effect of gas holdup profile

e) - f) Effect of mixing length profile

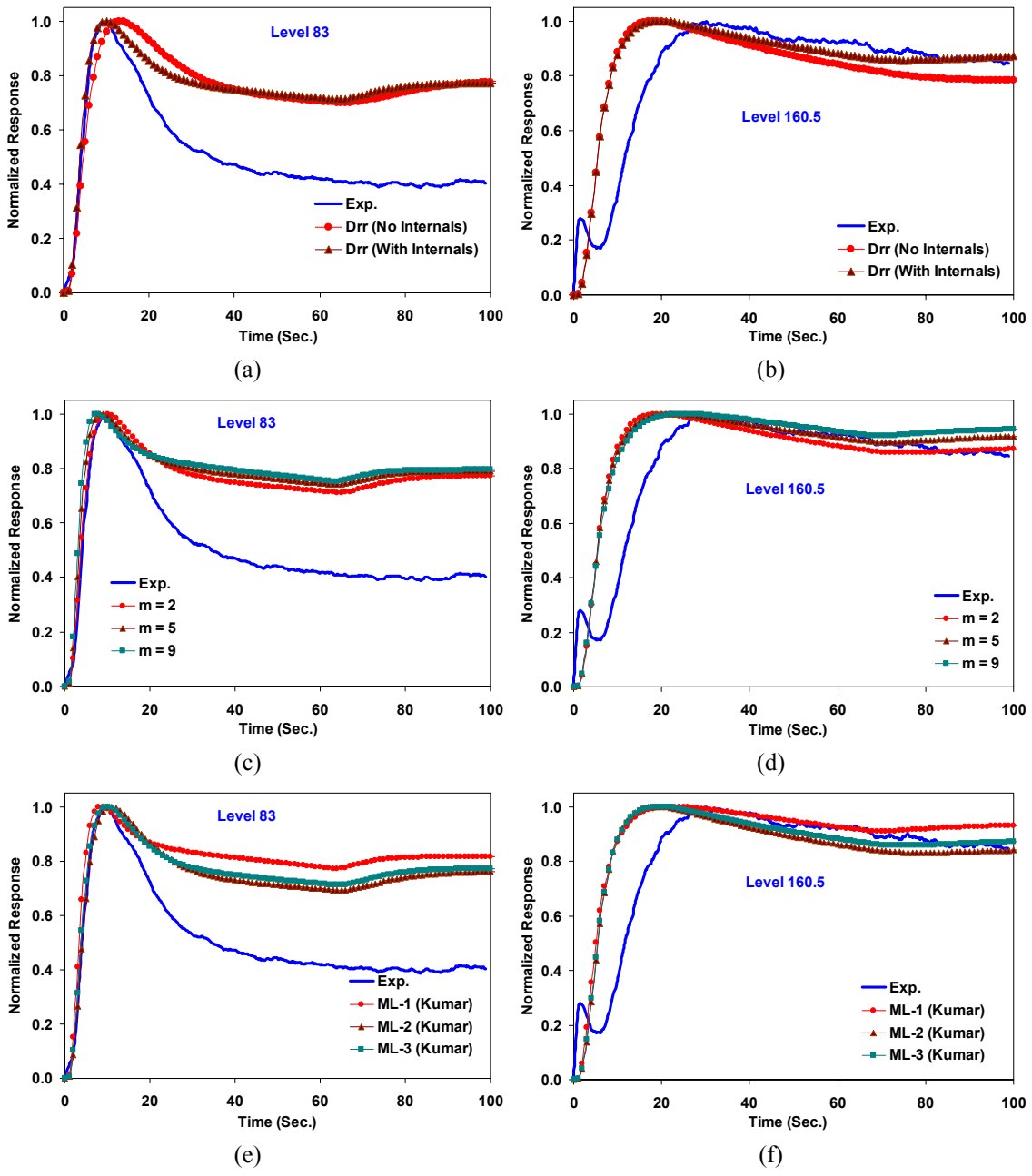


Figure 27. Parametric sensitivity of simulated tracer responses for Run 16.7 for Middle-Sidewall injection of $Mn_2O_3$ tracer

a) - b) Effect of $D_{rr}$ c) - d) Effect of gas holdup profile

e) - f) Effect of mixing length profile

## 3. Radioactive Gas Tracer Studies during FT-IV Runs at AFDU

In this section, the analysis of the gas tracer responses from Runs 16.6 and 16.7 are presented using a mechanistic gas-liquid/slurry mixing model with inter-phase mass transfer to account for the finite solubility of the gas tracer ($Ar^{41}$). The compartmentalization of the reactor volume is shown in Figure 28 and is the same as the Single Bubble Class Model (SBCM) described by Gupta (2002), whereas the model equations for each compartment are stated in Table 6.

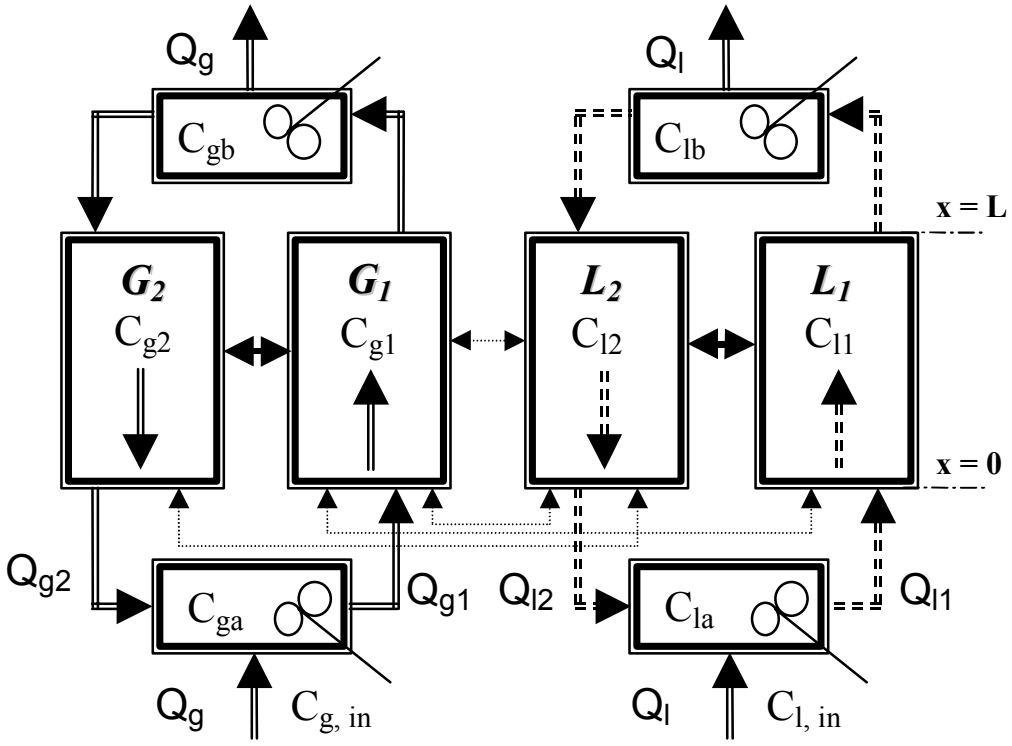


Figure 28. Schematic of the reactor compartmentalization for the gas-liquid mixing model with interphase mass transfer.

Table 6. Equations for Single Bubble-Class Gas-Liquid Recirculation Model.

$$\frac{\partial C_{g1}}{\partial t} = \left\{ \overline{D}_{xx_1} \frac{\partial^2 C_{g1}}{\partial x^2} - \overline{u}_{g1} \frac{\partial C_{g1}}{\partial x} - \frac{4\left(\overline{D}_{rr}\varepsilon_g\right)_{r=r''}}{r'' R\, \overline{\varepsilon}_{g1}} \left(C_{g1} - C_{g2}\right) + R_{x,g1} - \frac{k_{gulu} a_{gulu}}{\overline{\varepsilon}_{g1}} \left(HC_{g1} - C_{l1}\right) - \frac{k_{guld} a_{guld}}{\overline{\varepsilon}_{g1}} \left(HC_{g1} - C_{l2}\right) \right\}$$

$$\frac{\partial C_{g2}}{\partial t} = \left\{ \overline{D}_{xx_2} \frac{\partial^2 C_{g2}}{\partial x^2} + \overline{u}_{g2} \frac{\partial C_{g2}}{\partial x} - \frac{k_{gdld} a_{gdld}}{\overline{\varepsilon}_{g2}} \left(HC_{g2} - C_{l2}\right) + \frac{4r''/R}{R^2 - r''^2} \frac{\left(\overline{D}_{rr}\varepsilon_g\right)_{r=r''}}{\overline{\varepsilon}_{g2}} \left(C_{g1} - C_{g2}\right) + R_{x,g2} \right\}$$

$$\frac{\partial C_{l1}}{\partial t} = \left\{ \overline{D}_{xx_1} \frac{\partial^2 C_{l1}}{\partial x^2} - \overline{u}_{l1} \frac{\partial C_{l1}}{\partial x} + \left(\frac{r''}{r'}\right)^2 \frac{k_{gulu} a_{gulu}}{\overline{\varepsilon}_{l1}} \left(HC_{g1} - C_{l1}\right) - \frac{4\left(\overline{D}_{rr}\varepsilon_l\right)_{r=r'}}{r' R\, \overline{\varepsilon}_{l1}} \left(C_{l1} - C_{l2}\right) + R_{x,l1} \right\}$$

$$\frac{\partial C_{l2}}{\partial t} = \left\{ \begin{array}{l} \overline{D}_{xx_2} \dfrac{\partial^2 C_{l2}}{\partial x^2} + \overline{u}_{l2} \dfrac{\partial C_{l2}}{\partial x} + \dfrac{4r'/R}{R^2 - r'^2} \dfrac{\left(\overline{D}_{rr}\varepsilon_l\right)_{r=r'}}{\overline{\varepsilon}_{l2}} \left(C_{l1} - C_{l2}\right) + \left(\dfrac{r''^2}{R^2 - r'^2}\right) \dfrac{k_{guld} a_{guld}}{\overline{\varepsilon}_{l2}} \left(HC_{g1} - C_{l2}\right) \\ + \left(\dfrac{R^2 - r''^2}{R^2 - r'^2}\right) \dfrac{k_{gdld} a_{gdld}}{\overline{\varepsilon}_{l2}} \left(HC_{g2} - C_{l2}\right) + R_{x,l2} \end{array} \right\}$$

$$\frac{dC_{ga}}{dt} = \left\{ \begin{array}{l} \dfrac{U_G}{\overline{\varepsilon}_g \phi_{in} D_C} C_{g,in} - \dfrac{U_G}{\overline{\varepsilon}_g \phi_{in} D_C} C_{ga} + \dfrac{\overline{\varepsilon}_{g1}}{\overline{\varepsilon}_g \phi_{in} D_C} \dfrac{r''^2}{R^2} \overline{D}_{xx_1} \left.\dfrac{\partial C_{g1}}{\partial x}\right|_{x=0} \\ + \dfrac{\overline{\varepsilon}_{g2}}{\overline{\varepsilon}_g \phi_{in} D_C} \dfrac{\left(R^2 - r''^2\right)}{R^2} \overline{D}_{xx_2} \left.\dfrac{\partial C_{g2}}{\partial x}\right|_{x=0} - \dfrac{k_{CST} a_{CST}}{\overline{\varepsilon}_g} \left(HC_{ga} - C_{la}\right) + R_{x,ga} \end{array} \right\}$$

$$\frac{dC_{la}}{dt} = \left\{ \begin{array}{l} \dfrac{U_L}{\overline{\varepsilon}_l \phi_{in} D_C} C_{l,in} - \dfrac{U_L}{\overline{\varepsilon}_l \phi_{in} D_C} C_{la} + \dfrac{\overline{\varepsilon}_{l1}}{\overline{\varepsilon}_l \phi_{in} D_C} \dfrac{r'^2}{R^2} \overline{D}_{xx_1} \left.\dfrac{\partial C_{l1}}{\partial x}\right|_{x=0} \\ + \dfrac{\overline{\varepsilon}_{l2}}{\overline{\varepsilon}_l \phi_{in} D_C} \dfrac{\left(R^2 - r'^2\right)}{R^2} \overline{D}_{xx_2} \left.\dfrac{\partial C_{l2}}{\partial x}\right|_{x=0} + \dfrac{k_{CST} a_{CST}}{\overline{\varepsilon}_l} \left(HC_{ga} - C_{la}\right) + R_{x,la} \end{array} \right\}$$

$$\frac{dC_{gb}}{dt} = \left\{ - \frac{\overline{\varepsilon}_{g1}}{\overline{\varepsilon}_g \phi_{out} D_C} \frac{r''^2}{R^2} \overline{D}_{xx_1} \left.\frac{\partial C_{g1}}{\partial x}\right|_{x=L} - \frac{\overline{\varepsilon}_{g2}}{\overline{\varepsilon}_g \phi_{out} D_C} \frac{\left(R^2 - r''^2\right)}{R^2} \overline{D}_{xx_2} \left.\frac{\partial C_{g2}}{\partial x}\right|_{x=L} - \frac{k_{CST} a_{CST}}{\overline{\varepsilon}_g} \left(HC_{gb} - C_{lb}\right) + R_{x,gb} \right\}$$

$$\frac{dC_{lb}}{dt} = \left\{ - \frac{\overline{\varepsilon}_{l1}}{\overline{\varepsilon}_l \phi_{out} D_C} \frac{r'^2}{R^2} \overline{D}_{xx_1} \left.\frac{\partial C_{l1}}{\partial x}\right|_{x=L} - \frac{\overline{\varepsilon}_{l2}}{\overline{\varepsilon}_l \phi_{out} D_C} \frac{\left(R^2 - r'^2\right)}{R^2} \overline{D}_{xx_2} \left.\frac{\partial C_{l2}}{\partial x}\right|_{x=L} + \frac{k_{CST} a_{CST}}{\overline{\varepsilon}_l} \left(HC_{gb} - C_{lb}\right) + R_{x,lb} \right\}$$

$$d_B = \overline{d}_B$$

## Hydrodynamic Model

$$\varepsilon_g(\xi) = \overline{\varepsilon}_g \left(\frac{m+2}{m+2-2c}\right)\left(1 - c\xi^m\right)$$

| Liquid Phase | Gas Phase |
|---|---|
| $0 = -\left(\rho_g \varepsilon_g + \rho_l \varepsilon_l\right) g - \dfrac{dP}{dz} + \dfrac{1}{r}\dfrac{d}{dr}\left( r\varepsilon_l \left\{ \overbrace{\tau^m_{l,rz} + \tau^t_{l,rz}}^{\tau_{l,rz}} \right\} \right)$ | $0 = -\rho_g \varepsilon_g g - \varepsilon_g \dfrac{dP}{dz} + M_d$ |
| $\tau_{l,rz}(\xi) = -\dfrac{\rho_l \nu_l^m}{R}\dfrac{du_l}{d\xi} - \dfrac{\rho_l l^2}{R^2}\left(\dfrac{du_l}{d\xi}\right)^2$ | $M_d = -\dfrac{3\varepsilon_l \varepsilon_g \rho_l C_D}{4 d_B}\left(u_l - u_g\right)^2$ |
| $\dfrac{l(\xi)}{R} = \dfrac{a(1-\xi)}{(\xi+b)^c} + d(1-\xi)^e$ Kumar *et al.* (1995) | $C_D = max\left[\dfrac{24}{Re}\left(1 + 0.15\,Re^{0.687}\right), \dfrac{8}{3}\dfrac{Eo}{Eo+4}\right]$ Tomiyama *et al.* (1995) |

For details of the derivation of the gas-liquid recirculation model equations, the solution procedure and the parameter estimation, the reader is referred to Gupta (2002). Since only a small fraction of the gas escapes along with the slurry through the reactor outlet, this effect has not been incorporated into the gas phase mixing model. While the slurry recycle effect could be safely ignored for the gas phase model, it would not be

appropriate to do so for the liquid phase model. It could be argued that since mass transfer of the gas tracer to the liquid phase is significant, consideration should be given to the effect of the slurry recycle on the gas tracer responses. Similarly, the effect of the changing gas velocity along the reactor could have an effect on the simulated responses, but has not been considered in the model comparisons with data presented in this study. In theory both of these could be achieved but call for significant model and code development efforts. It is proposed that these effects be explored in future continuation of the present work to bring the current mixing models to the next level of sophistication.

### 3.1. Comparison of Experimental Tracer Responses with Simulation Results

Table 7 lists the parameters computed by the gas-liquid recirculation model. As for the parameters of liquid/catalyst mixing model, gas-mixing model parameters were computed from the one-dimensional sub-model for three different superficial gas velocities (inlet, outlet and mean) for both Run 16.6 and Run 16.7 to explore their dependence on the changing superficial gas velocity along the reactor length. However, the figures presented subsequently have all been computed using the parameters based on the mean superficial gas velocity. Additionally, the simulated responses account both for the presence of the internals as well as for the radiation attenuation based on the Beer-Lambert's law as presented by Gupta (2002).

Figures 29 to 32 show the comparison of the simulation results using different values of the Henry's constant (H) with experimental tracer data for Run 16.6 in response to the radioactive gas tracer injected below the gas sparger. One can see from these figures that the model predictions are in good agreement with the experimental responses for zero and small values of the Henry's constant at lower reactor levels, while at higher levels, a Henry's constant of 0.15 (dimensionless) seems to bring the predictions closer to data. However, for the thermodynamically estimated Henry's constant ($H = H^* = 0.248$), the predicted responses are slightly delayed in time as compared to the experimental data. The reason for these discrepancies between simulated and experimental responses could lie in the uncertainties associated with the estimated Henry's constant, which influences the mean residence time of the gas species in the reactor. However, in general, there is

good agreement between the simulated and experimental responses for the Henry's constant of 0.15 and 0.248.

Table 7. Computed model parameters for the gas-mixing model.

| **Parameter** | **Run 16.6** | | | **Run 16.7** | | |
|---|---|---|---|---|---|---|
| **$U_G$ (cm/s)** | **12.8** | **9.89** | **11.4** | **18.2** | **15.2** | **16.7** |
| $\bar{\varepsilon}_{l1}$ | 0.458 | 0.458 | 0.458 | 0.478 | 0.478 | 0.478 |
| $\bar{\varepsilon}_{l2}$ | 0.564 | 0.564 | 0.564 | 0.607 | 0.607 | 0.607 |
| $\bar{\varepsilon}_{g1}$ | 0.516 | 0.524 | 0.520 | 0.481 | 0.488 | 0.484 |
| $\bar{\varepsilon}_{g2}$ | 0.448 | 0.443 | 0.446 | 0.416 | 0.410 | 0.413 |
| $\bar{u}_{l1}$ (cm/s) | 33.6 | 33.6 | 33.6 | 36.2 | 36.2 | 36.2 |
| $\bar{u}_{l2}$ (cm/s) | 30.1 | 30.1 | 30.1 | 32.2 | 32.2 | 32.2 |
| $\bar{u}_{g1}$ (cm/s) | 46.3 | 42.6 | 44.4 | 57.2 | 52.9 | 55.1 |
| $\bar{u}_{g2}$ (cm/s) | 22.5 | 24.6 | 23.5 | 19.9 | 22.1 | 21.0 |
| $r'/R_C$ | 0.739 | 0.739 | 0.739 | 0.742 | 0.742 | 0.742 |
| $r''/R_C$ | 0.821 | 0.791 | 0.806 | 0.860 | 0.834 | 0.845 |
| $\bar{D}_{xx_1}$ (cm$^2$/s) | 624 | 624 | 624 | 601 | 601 | 601 |
| $\bar{D}_{xx_2}$ (cm$^2$/s) | 606 | 606 | 606 | 573 | 573 | 573 |
| $\bar{D}_{rr}\big\|_{No\ Int.}$ (cm$^2$/s) | 153 | 153 | 153 | 146 | 146 | 146 |
| $\bar{D}_{rr}\big\|_{With\ Int.}$ (cm$^2$/s) | 60 | 60 | 60 | 55 | 55 | 55 |
| $\bar{d}_B$ (cm) | 0.198 | 0.122 | 0.159 | 1.28 | 0.632 | 0.940 |
| $k_{gulu}$ (cm/s) | 0.060 | 0.064 | 0.062 | 0.030 | 0.039 | 0.034 |
| $a_{gulu}$ (1/cm) | 13.3 | 23.3 | 17.2 | 1.82 | 3.92 | 2.55 |
| $k_{guld}$ (cm/s) | 0.147 | 0.183 | 0.163 | 0.063 | 0.087 | 0.072 |
| $a_{guld}$ (1/cm) | 2.32 | 2.53 | 2.44 | 0.437 | 0.715 | 0.539 |
| $k_{gdld}$ (cm/s) | 0.046 | 0.050 | 0.048 | 0.023 | 0.030 | 0.026 |
| $a_{gdld}$ (1/cm) | 13.6 | 21.9 | 16.8 | 1.96 | 3.89 | 2.64 |
| $k_{CST}$ (cm/s) | 0.062 | 0.060 | 0.062 | 0.033 | 0.040 | 0.035 |
| $a_{CST}$ (1/cm) | 15.0 | 24.4 | 18.7 | 2.18 | 4.41 | 2.96 |

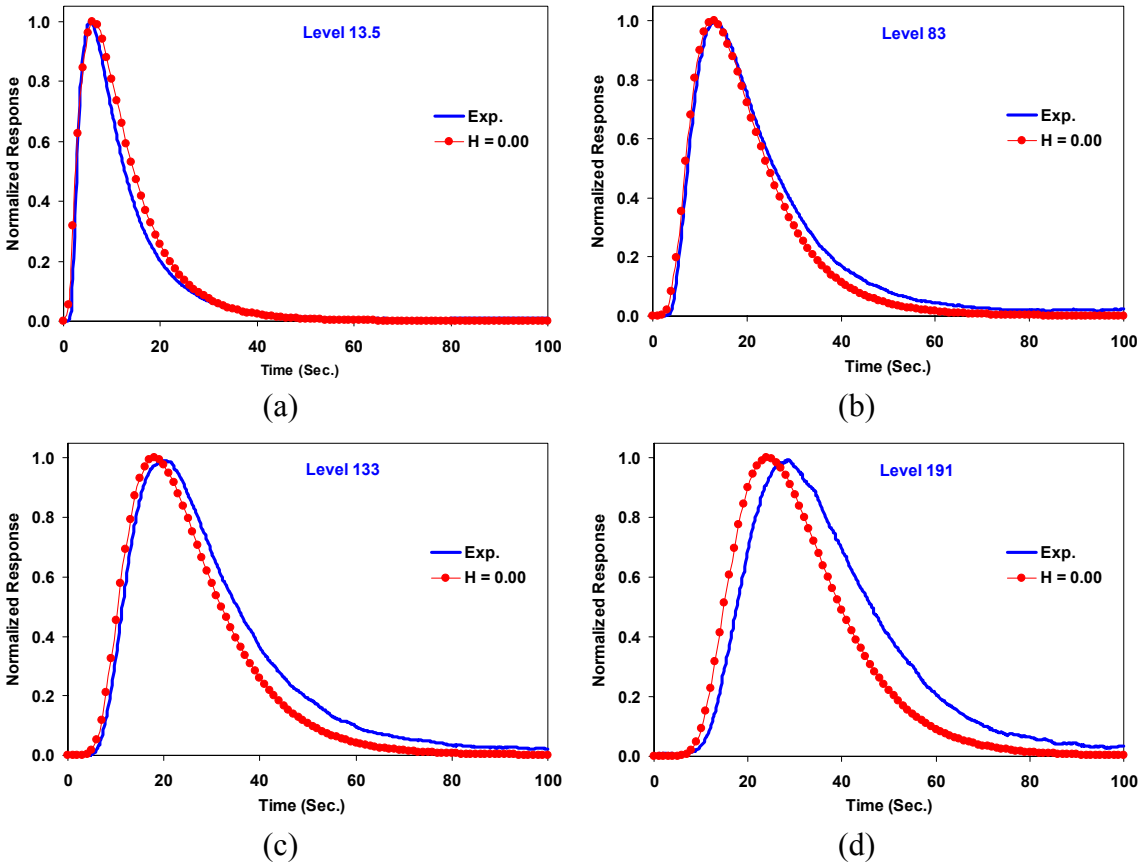


Figure 29. Comparison of experimental and simulated gas tracer response curves for Run 16.6 with Henry's constant, H = 0.

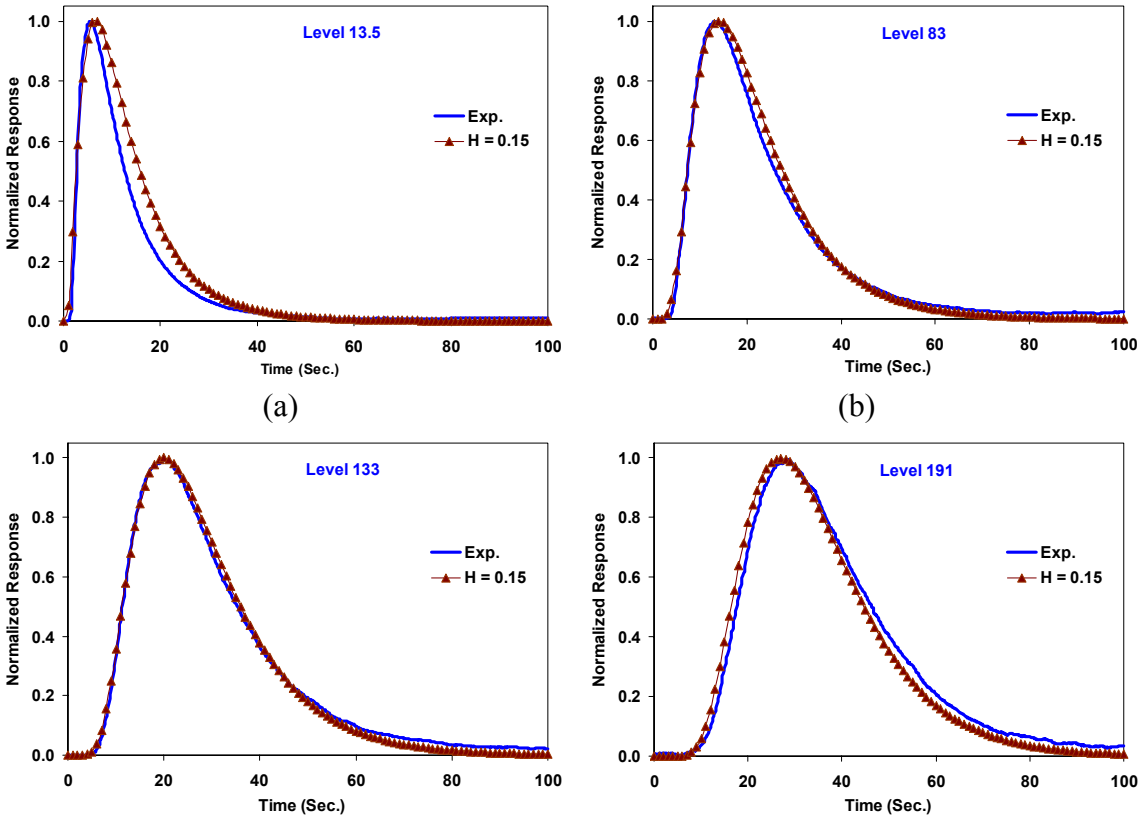


Figure 30. Comparison of experimental and simulated gas tracer response curves for Run 16.6 with Henry's constant, H = 0.15.

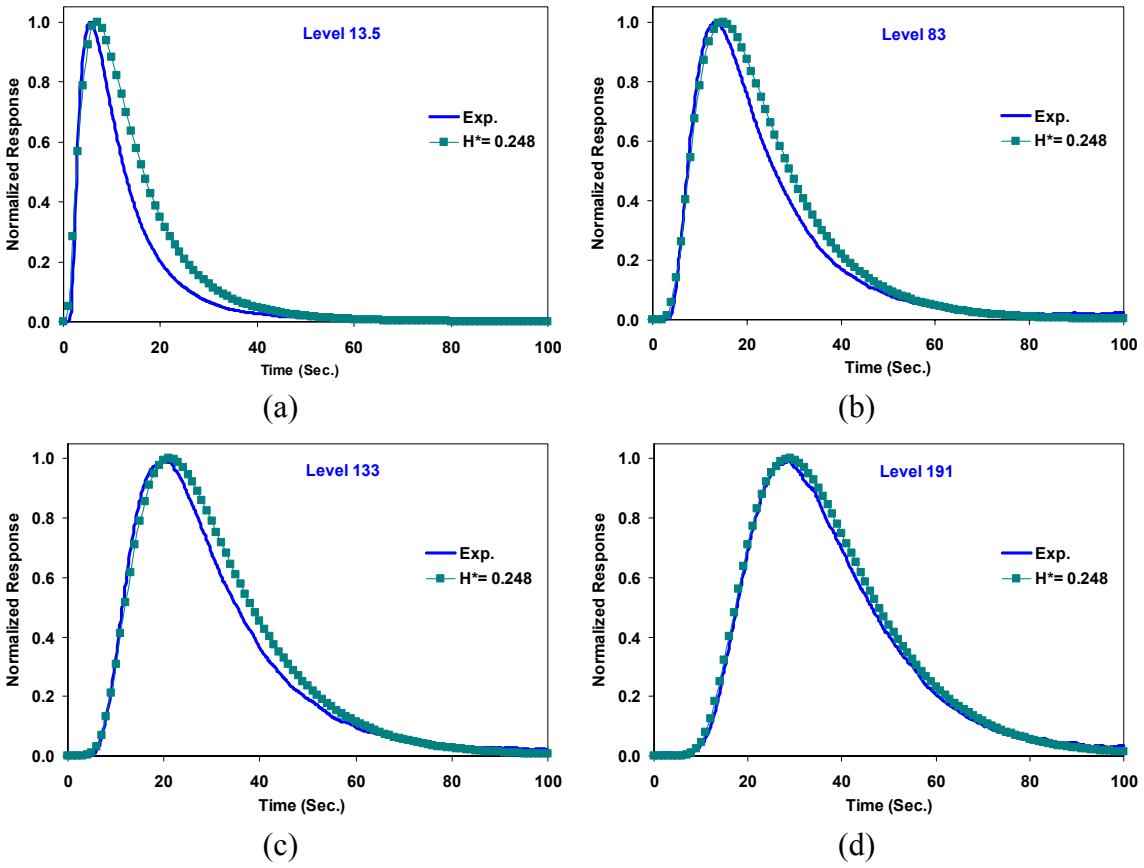


Figure 31. Comparison of experimental and simulated gas tracer response curves for Run 16.6 with thermodynamically estimated Henry's constant, H* = 0.248.

As for Run 16.6, Figures 32 to 34 show the comparison of the simulation results with experimental data for the radioactive gas tracer injected below the gas sparger for Run 16.7. One can see from these figures that at the lowest tracer-monitoring level, the model simulations are in good agreement with the experimental responses for smaller values of the Henry's constant than predicted by thermodynamic calculations. For the middle monitoring levels, a Henry's constant of 0.15 (dimensionless) again provides the best match between data and simulations. The thermodynamically estimated Henry's constant (H*=0.245) results in good predictions of the data at the middle levels and is in excellent agreement with the experimental data at the two highest levels in the column.

Overall, the mismatch between simulated and experimental tracer curves is well within the thermodynamic estimation accuracy of the Henry's constant that can have a variation of ± 25-50%. Additional figures at other levels are presented in Appendix C.

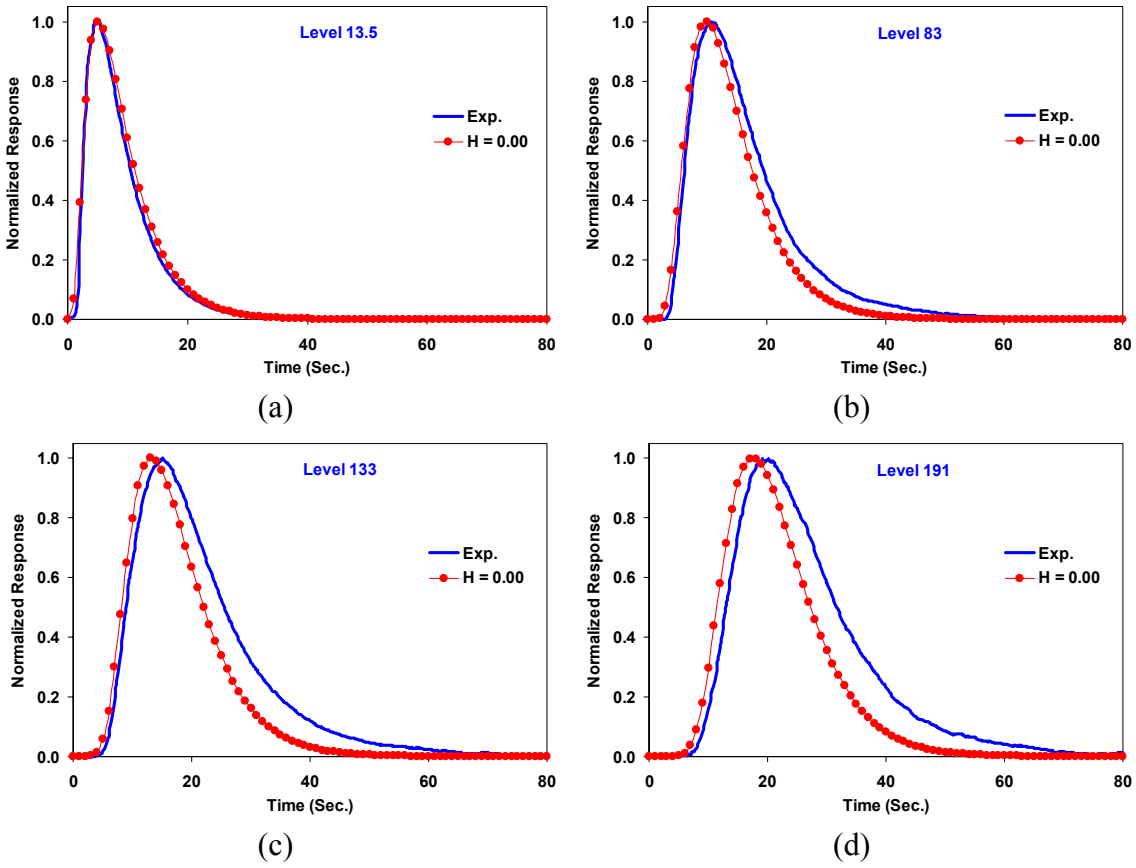


Figure 32. Comparison of experimental and simulated gas tracer response curves for Run 16.7 with Henry's constant, H = 0.

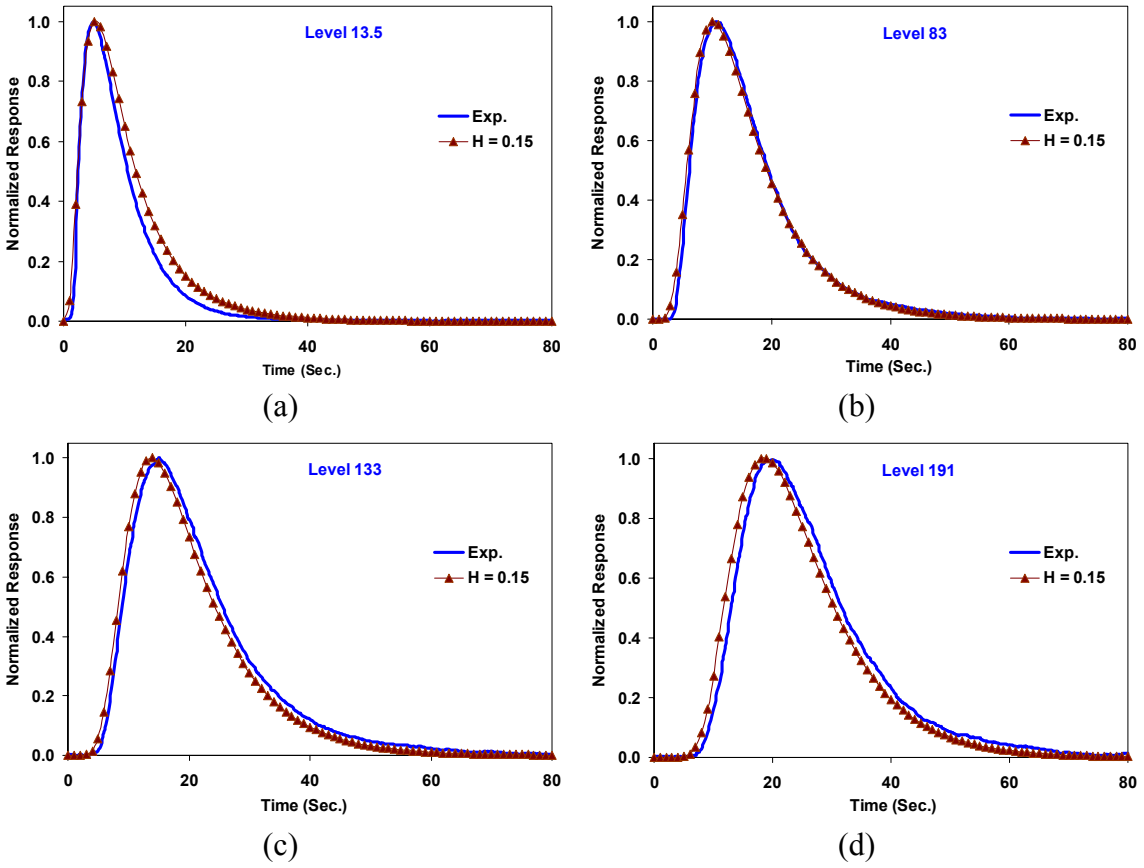


Figure 33. Comparison of experimental and simulated gas tracer response curves for Run 16.7 with Henry's constant, H = 0.15.

It is worth mentioning that the protocols for executing the tracer experiments during the FT-IV runs were improved from those that were in place when tracer tests were done during methanol synthesis (Degaleesan, 1997). Additionally, the reactor used for FT-IV is considerably shorter than that used for methanol synthesis experiments. Furthermore, the superficial gas velocities employed for methanol runs were significantly higher than those used for FT-IV runs. As a result, the gas tracer for FT-IV experiments gets convected axially on a relatively longer time scale as compared to the methanol runs implying that comparatively it is more backmixed or has a lower plug flow character. As has been discussed by Gupta (2002), the more a radiotracer gets mixed, the lesser the

tracer broadening effect, which vanishes for a completely backmixed flow pattern. Thus, the gas tracer responses for FT-IV have relatively lower (negligible) tracer broadening effects as compared to methanol gas tracer responses.

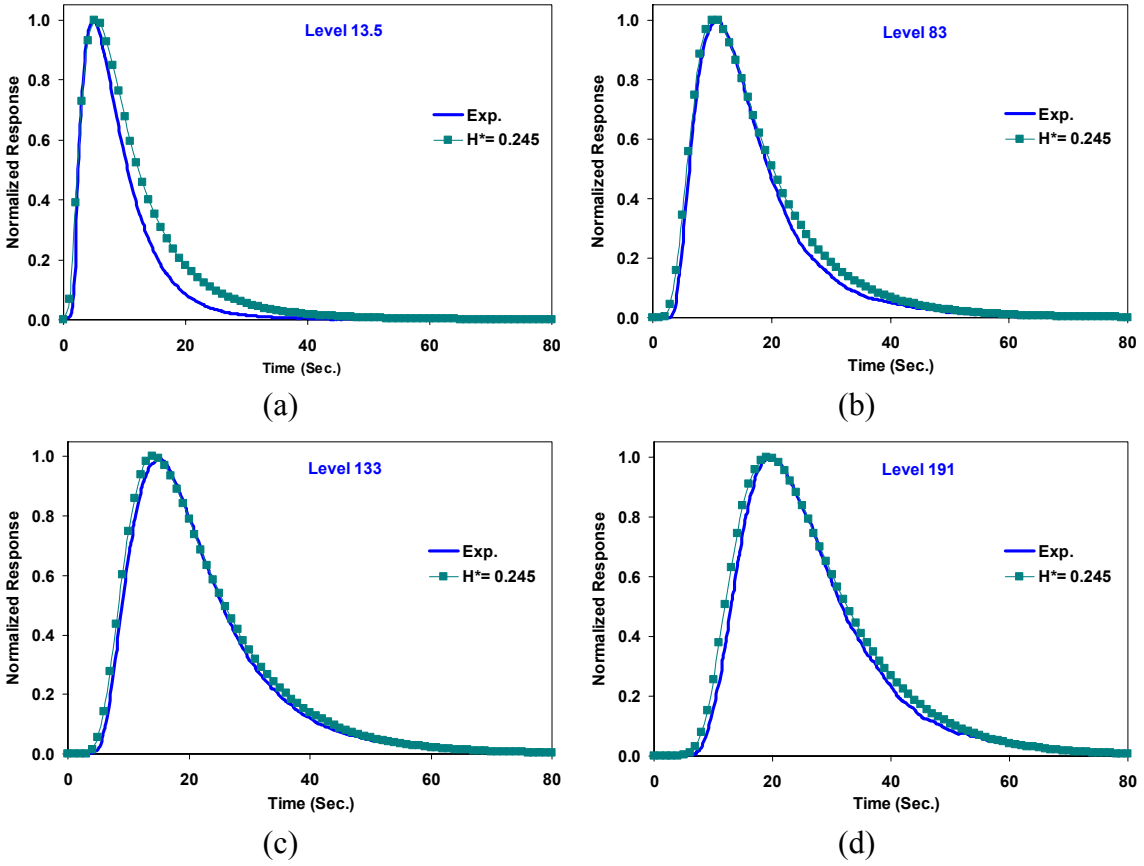


Figure 34. Comparison of experimental and simulated gas tracer response curves for Run 16.7 with thermodynamically estimated Henry's constant, H* = 0.245.

### 3.2. Parametric Sensitivity of Simulated Gas Tracer Responses

As for the liquid/catalyst tracer experiments, Figures 35 and 36 present the effect of the various model input-parameters on the computed gas tracer responses for Run 16.6 and Run 16.7 respectively. For this purpose, the normalized tracer response at level 191 inches as marked on the outside tape has been chosen. As before for the liquid responses, the gas tracer responses also show a finite but relatively insignificant effect of the radial

eddy diffusivity on the computed tracer response, with the response computed with account for the presence of internals yielding better agreement with data. Secondly, since the gas tracer is injected below the gas sparger, it is relatively well mixed radially resulting in a negligible difference between attenuated and non-attenuated responses. Thirdly, the effect of the gas holdup profile on the computed responses is negligible, however, the lower values of the exponent "*m*" provide a marginally better agreement between simulations and data. Lastly, the effect of the mixing length profile on the computed responses is also not large, with ML-1 (representative of bubbly flow as per Kumar, 1994) resulting in the greatest deviation between simulated and experimental responses.

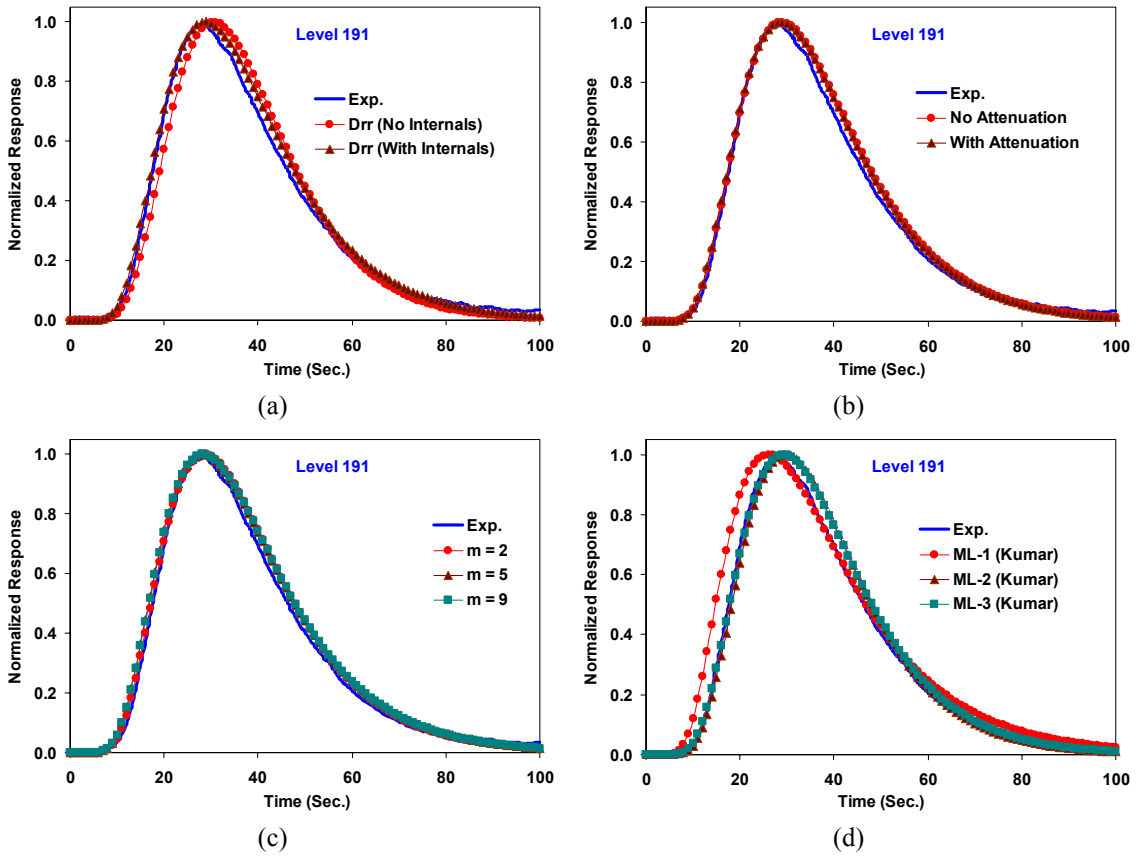


Figure 35. Parametric sensitivity of simulated gas tracer responses for Run 16.6

a) Effect of $D_{rr}$ b) Effect of radiation attenuation

c) Effect of gas holdup profile d) Effect of mixing length profile

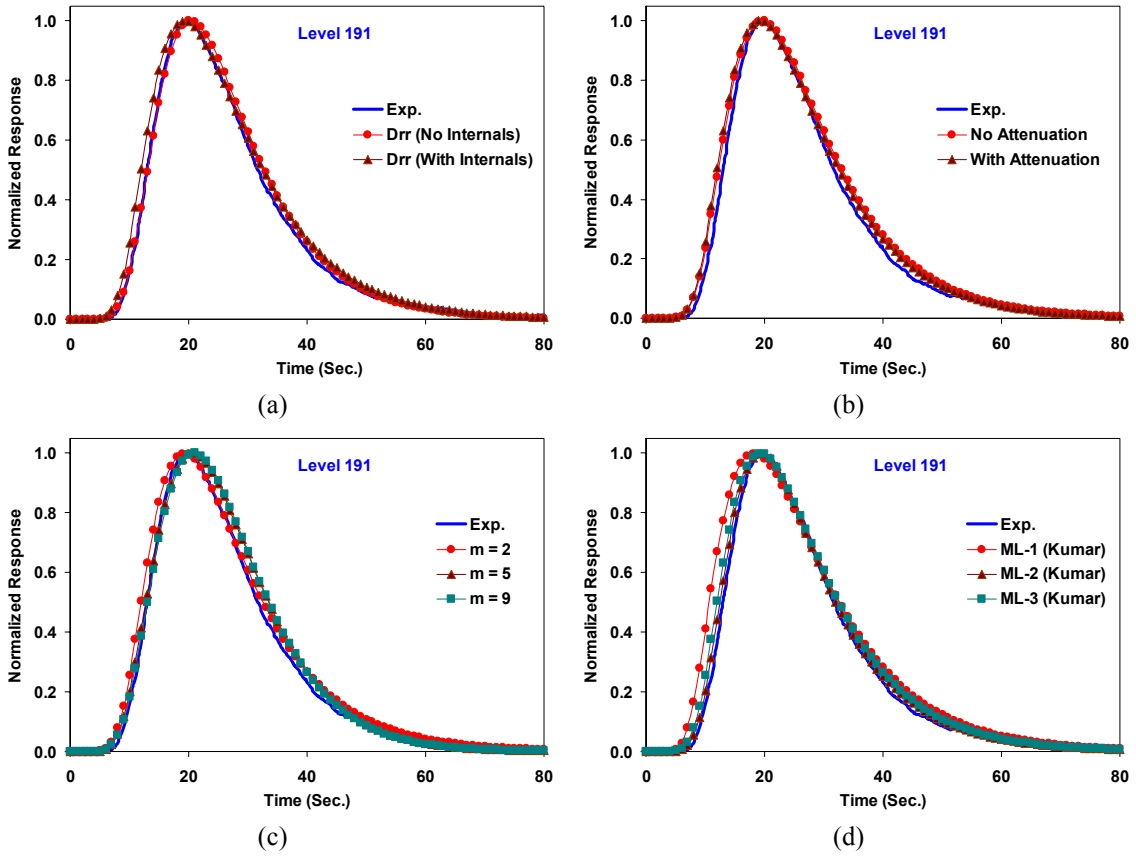


Figure 36. Parametric sensitivity of simulated gas tracer responses for Run 16.7

a) Effect of $D_{rr}$ b) Effect of radiation attenuation

c) Effect of gas holdup profile d) Effect of mixing length profile

In conclusion, the dynamics of the gas phase mixing during the FT-IV runs is well predicted by the SBCM developed by Gupta (2002). This includes not only the peak arrival times of the tracer impulse at various detector levels, but also the overall shape of the normalized responses. In general, the overall agreement between model predictions and data for FT-IV experiments is better than that for methanol runs. A possible reason for this outcome could be the relatively better known hydrodynamics (turbulence closure, drag, etc.) at the conditions of the FT-IV experiments. This points to the need for future investigations to expand the hydrodynamic database to operating conditions emulating those of the methanol runs.

## 4. Summary and Conclusions

Detailed hydrodynamic investigations on a pilot-scale FT reactor were conducted at the AFDU under reaction conditions with the scope of unraveling a few of the complexities associated with hydrodynamics of slurry bubble column reactors. This was a unique venture as most laboratory scale experiments are usually conducted under cold-flow conditions, or in cases where reaction conditions are involved, the studies are limited to relatively small vessels. However, relatively simple tasks that are taken for granted in a laboratory setup often prove to be the most challenging during a field experiment. The experience with the γ-densitometry scans at the AFDU for the present investigation is a case in point.

To summarize the evaluation of the data from the densitometry studies, one can state that it is evident that the uncertainties in the estimation of chordal averaged gas holdup from the gamma scans data are large and significant. This makes any quantitative holdup profile estimate difficult for use in a hydrodynamic model. Therefore, future gamma-scans at the LaPorte AFDU should be considered only when the errors associated with source-detector misalignment are resolved with a test on a phantom of known geometry. A simple experiment was described that could be performed to achieve this objective. In the absence of a reliable and precise densitometry equipment, and until the new scanning protocols are designed and formulated, it is recommended that sectional Differential Pressure (DP) measurements be conducted together with Nuclear Densitometry Gauge (NDG) measurements to aid in the determination of the radial gas holdup profile. The NDG measurements should be performed at several axial locations around which DP measurements exist, and at least along three chordal lengths. In the past, from a single NDG line average measurement along the column diameter and DP measurements, the holdup profile was estimated assuming one of the parameters in the profile. Additional accurate chordal measurements would provide for estimation of the entire set of holdup profile parameters, i.e., the values of $\bar{\varepsilon}_g$, $c$ and $m$.

The mixing studies using radioactive tracers provided invaluable information on the degree of backmixing in the individually traced phases. Since the temporal evolution

of tracer responses along the reactor length is dependent on the condition of flow that existed at the particular moment of injection, repeated experiments were conducted to properly assess ensemble averaged tracer responses for comparison with simulation results from mixing models. The injection of gas tracer in the gas feed line before the sparger ensured a high degree of cross-sectional uniformity of the tracer at the point of tracer entry into the column, which was the gas sparger. As a result, excellent reproducibility was achieved for gas tracer experiments under both operating conditions. It is, therefore, proposed that for future gas tracer experiments many repeated tracer injections are not necessary. It is, however, recommended that for a given operating condition, one repetition still be done as a check. On the other hand, for point tracer injections of the catalyst or $Mn_2O_3$ tracers, it is recommended that injections be repeated at least five times to obtain the ensemble-averaged responses. This is necessary to account for the variable flow conditions at the point of tracer injection.

Generally, it is expected that the catalyst is well suspended in the liquid phase because of the small size (~ 10-50 μm) of the catalyst particles in a slurry bubble column operation. During the course of the experimentation with the catalyst and "liquid" tracers at the AFDU, it was confirmed that the differences in responses from the catalyst and fine powdered $Mn_2O_3$ tracer injections are minimal indicating the validity of the pseudo-homogeneous assumption for the liquid (FT-wax) plus the solid (catalyst) phases. Valuable qualitative information was obtained in Run 16.6 by employing the ***wrong*** tracer (coarse $MnO_2$ particles ~ 150 μm were accidentally used instead of the fine $Mn_2O_3$ powder) which clearly demonstrated that coarse particles do settle. It is evident that because of the settling of these large $MnO_2$ particles, the tracer responses from $MnO_2$ tracer particles is dramatically different than the responses due to the catalyst or "liquid" (fine particles) tracers.

Both the gas and the liquid (slurry) tracer data was analyzed with mixing models developed at CREL (Degaleesan, 1997; Gupta *et al*., 2001[a]). The existing liquid/slurry mixing model was successfully modified by splitting the reactor domain to account for the slurry exit from the middle portion of the column as well as the slurry recycle at the bottom of the reactor. Comparison of tracer data with simulation results shows that the

responses obtained from the catalyst tracer injection in the bottom-center portion of the reactor for Run 16.6 are in reasonable agreement with the predictions of the liquid-mixing model. However, such is not the case with the tracer responses obtained from the side-wall injection in the middle portion of the reactor, since the tracer injection point is very close to the slurry exit, which results in incomplete radial mixing of the tracer before encountering the slurry outlet. Thus, model assumptions are severely violated for tracer injections very close to the slurry exit (as for the sidewall tracer injection), and this manifests itself in poor agreement between simulated and experimental data. However, the model assumptions seem to hold well for the tracer injection into the reactor bottom, and good agreement is obtained between simulated and experimental data. It is recommended that for future tracer tests on this unit with a finite slurry outflow, sidewall tracer injections into the middle portion of the reactor be avoided unless comparison with 3-D mixing models is being considered.

Similar to Run 16.6, the liquid/slurry-mixing model was used to model the liquid and catalyst tracer data acquired during the operating conditions of Run 16.7, and simulation results compare well with experimental data. The higher superficial gas velocity for Run 16.7 apparently results in relatively faster radial mixing as compared to Run 16.6. Therefore, for Run 16.7, the agreement between simulation results and experimental data for the sidewall-middle tracer injection are considerably better than for Run 16.6. Nevertheless, for future tracer studies at the AFDU, bottom-middle injection is recommended for characterization of mixing of the slurry phase for this particular reactor setup and sidewall injection should be avoided.

Correct “liquid” tracer was employed during Run 16.7 to trace the liquid phase. It appears that the fine $Mn_2O_3$ particles tag the liquid phase very well, and consequently the tracer responses, obtained by employing these particles as tracers, are predicted well by the mixing model which is based on the assumption of a pseudo-homogeneous slurry phase. Compared to the catalyst tracer particles, fine $Mn_2O_3$ tracer appears to follow the liquid even more closely as in general there is even better agreement between simulation results for the slurry (liquid) and experimental data for $Mn_2O_3$ tracer responses. However, at conditions of Run 16.7 the catalyst tracer also seems to follow the liquid closely. This

analysis indicates that a reliable estimate of the state of liquid mixing can be obtained by using the fine $Mn_2O_3$ particles.

For the analysis of gas tracer data, the gas-liquid recirculation model, based on a constant bubble size as developed by Gupta *et al*. (2001[a]), was used to simulate the gas tracer responses acquired during the FT-IV operation of the AFDU. The model is able to predict the characteristic features of the observed experimental responses. The sub-model employed to compute the gas-liquid recirculation rates, for the given gas holdup profiles and operating conditions, predicts a mean bubble size of 1.6 mm for Run 16.6 and 9.4 mm for Run 16.7. These bubble sizes reflect the higher gas holdup measured during Run 16.6 as compared to Run 16.7 with the magnitude of the bubble sizes suggesting that Run 16.7 was most likely in churn-turbulent flow while Run 16.6 most likely experienced transition or even bubbly flow. For Run 16.6, the predicted tracer responses based on Henry's constant of H = 0.15 are in reasonable agreement with experimental data. However, the predicted response for the thermodynamically estimated Henry's constant of H* = 0.248 seems to be marginally delayed in time compared to the experimental curve. On the other hand, the predicted tracer responses for Run 16.7 based on the thermodynamically predicted Henry's of H* = 0.245 are in reasonably good agreement with experimental data. This could be due to the higher superficial gas velocity in Run 16.7 that most likely results in satisfying the model assumptions better as compared to Run 16.6.

Analysis of the various model parameters on the computed responses indicates that the effect of internals on the radial eddy diffusivities is significant, which consequently considerably affects the computed liquid tracer responses. This effect is more pronounced and important for responses resulting from point injection of liquid/catalyst tracer than for gas tracer responses. Comparatively, gas holdup and mixing length have relatively lower influence on the simulation results, especially for gas tracer responses. The parametric sensitivity analysis indicates that a gas holdup profile with low values of the exponent "m" and mixing length (ML-3) are good choices as the input model parameters for the FT-IV operating conditions. However, more investigations need

to be made to formulate reliable principles based on which these parameters could be chosen for a broader range of reactor sizes and operating conditions.

In conclusion, the by-and-large reasonable agreement of the simulation results with experimental data indicates that the mechanistic modeling of gas-liquid flows in slurry bubble columns, in the framework developed by Gupta *et al*. (2001[a]) and Gupta (2002), provides a relatively simple tool for assessing the extent of mixing to within 20% in these reactor types. It should be re-emphasized that numerous physical phenomena that affect mixing in a slurry bubble column operation result in extremely complex physics which is difficult to model precisely with the current level of understanding. In this sense, these models are powerful as they systematically incorporate the known physics of slurry bubble column hydrodynamics and provide a fundamentally based framework for bubble column reactor modeling.

# Appendix A. Parameter Estimation of Bubble Column Hydrodynamics

This appendix describes the liquid recirculation model of Ueyama and Miyauchi (1979) as well as presents the correlations for predicting the parameters of the radial gas holdup profile and the radial and axial eddy diffusivities from the CT (Computed Tomography) and CARPT (Computer Automated Radioactive Particle Tracking) databases.

**Model for Liquid Velocity Profiles (Ueyama and Miyauchi, 1979)**

$$\frac{u_l + |u_w|}{u_0 + |u_w|} = \left[1 - \left(\frac{r}{R}\right)^2\right]^2 \tag{A-1}$$

$$u_0 = \frac{gD\varepsilon_g}{192\upsilon_t}\left(\frac{4 - 3\varepsilon_g}{1 - \varepsilon_g}\right) + \frac{U_L}{1 - \varepsilon_g} \tag{A-2}$$

$$|u_w| = \frac{gD\varepsilon_g}{192\upsilon_t}\left(\frac{2 - 3\varepsilon_g}{1 - \varepsilon_g}\right) - \frac{U_L}{1 - \varepsilon_g} \tag{A-3}$$

where, D ≡ column diameter

g ≡ acceleration due to gravity

$U_L$ ≡ superficial liquid velocity

$u_0$ ≡ centerline interstitial liquid velocity

$|u_w|$ ≡ absolute value of the interstitial axial liquid velocity near the wall.

$U_L$ is zero if the liquid is a batch. In this approach, the velocity in the core is matched to the universal velocity profile for the laminar sub-layer at a distance δ from the column wall. With this model, some degree of empiricism is involved in extending the single-phase universal velocity relations to two-phase flows.

**Model for Liquid Velocity Profiles (Anderson and Rice, 1989)**

In this model, the following equation was derived relating the dimensionless pressure gradient, p' to $\xi^*$:

$$\xi^* = \sqrt{\bar{\varepsilon}_g / (1 - p')} \tag{A-4}$$

Here, $\xi^*$ is the dimensionless radius at which the downward liquid velocity is maximum. They also derived the following equation for the downward maximum velocity:

$$u_l(\xi = \xi^*) = u_{\xi^*} = \frac{gR^2 \bar{\varepsilon}_g}{4\upsilon_m \xi^{*2}} \left( \xi^{*2} - 1 - 2\xi^{*2} \ln \xi^* \right) \tag{A-5}$$

**Correlations for Parameters of the Radial Gas Holdup Profiles (Wu *et al*., 2001)**

As mentioned previously, the following expression is usually used to describe the radial distribution of the gas holdup in well-developed flow zones of a bubble column:

$$\varepsilon_g(\xi) = \bar{\varepsilon}_g \left( \frac{m+2}{m+2-2c} \right) (1 - c\xi^m) \tag{A-6}$$

Wu *et al*. (2001) correlated the parameters *m* and *c* in the above expression with macroscopic flow variables. These correlations are:

$$m = 2.188x10^3 \; Re_G^{-0.598} \; Fr_G^{0.146} Mo_L^{-0.004} \tag{A-7}$$

$$c = 4.32x10^{-2} \; Re_G^{0.2492} \tag{A-8}$$

where,

$$Re_G = \frac{D_C U_G (\rho_L - \rho_G)}{\mu_L}$$

$$Fr_G = \frac{U_G^2}{gD_C}$$

$$Mo_L = \frac{g\mu_L^4}{(\rho_L - \rho_G)\sigma_L^3}$$

$U_G \equiv$ gas superficial velocity

$D_C \equiv$ column diameter

$\rho_L$ ≡ density of the liquid phase

$\mu_L$ ≡ molecular viscosity of the liquid phase

$\sigma_L$ ≡ surface tension of the liquid phase

$\rho_G$ ≡ density of the gas phase (dependent on operating pressure)

For estimating the cross-sectional average gas holdup, $\bar{\varepsilon}_g$, an appropriate correlation could be chosen as presented by Ong (1999) and Kemoun *et al*. (2001).

**Correlations for Radial and Axial Turbulent Eddy Diffusivities (Degaleesan, 1997)**

For estimating some of the parameters of the mixing models presented in this report, the correlations developed by Degaleesan (1997) for estimating the radial ($D_{rr}$) and axial ($D_{xx}$) turbulent eddy diffusivities are used. These correlations are:

$$D_{rr}(\xi) = \left( -\frac{350}{D_C^{0.8}} + 13\left(D_C U_{Ge}\right)^{0.3} \right) P_2(\xi) \tag{A-9}$$

$$D_{xx}(\xi) = \left( -\frac{2325}{D_C^{0.8}} + 106.6\left(D_C U_{Ge}\right)^{0.3} \right) P_4(\xi) \tag{A-10}$$

$$P_2(\xi) = 0.1653 + 5.0717\xi - 5.0929\xi^2 \tag{A-11}$$

$$P_4(\xi) = 0.5847 + 0.005035\xi + 0.4693\xi^2 + 3.2704\xi^3 - 3.4979\xi^4 \tag{A-12}$$

where $U_{ge}$ is an equivalent superfical gas velocity based on the observed gas holdup and is given as

$$U_{ge} = \left( \frac{\bar{\varepsilon}_g}{0.07} \right)^{(0.474 - 0.000626 D_C)} \tag{A-13}$$

# Appendix B. Effect of Boundary Conditions on Simulation Results from Mixing Models

In this appendix, the comparison of the simulation results from the gas and liquid phase mixing models, reported by Gupta (2002), with the correct (Dirichlet) and incorrect (Danckwerts') boundary conditions is presented. For a well-defined "closed" system, Danckwerts' boundary conditions consist of the Robin (mixed) boundary conditions at the inlet boundary with Neumann boundary conditions at the outlet. It seemed natural at first to use the Danckwerts' boundary conditions for the well-developed zones in the mixing models presented earlier. However, it was subsequently realized that since the boundaries of the well-developed zones are not the ***physical*** boundaries of the reactor domain but only ***fictitious*** "ones", as pertinent to the compartmentalization of the reactor domain, the use of Danckwerts' boundary conditions for a "closed" system is ***unphysical***. Therefore, the correct boundary conditions to use for the well-developed zones are the continuity of species concentration in both the gas and liquid phases, which makes the concentrations at the ends of the well-developed flow zones equal to the concentrations in the respective end zones.

To elucidate the problem with using the Danckwerts boundary conditions for the reactor compartmentalization proposed in this study, a simplified situation of a unidirectional flow with three sub-zones is presented in Figure B-1. If Danckwerts boundary conditions are imposed at the two boundaries of the axial dispersion zone (zone B), it implies that if the tracer is injected in zone C, ***mathematically*** it will never be able to get into zones A or B because of the zero flux condition at the hypothetical interface between zone B and zone C. This is physically unrealistic since there are situations where the effective dispersion coefficients (in the context of the ADM) are estimated from

tracer responses resulting from the injection of the tracer close to the vessel exit in a location similar to zone C. On the contrary, if Dirichlet boundary conditions are imposed at the two boundaries of the axial dispersion zone, a tracer injected into zone C will be able to diffuse into zone B and subsequently into zone A with convection having zero contribution to the tracer transport into zones A and B. Thus, by appropriately incorporating the dispersive fluxes from the axial dispersion zone into the end zone mass balance equations, with a superposition of the Dirichlet boundary conditions at the two boundaries of the axial dispersion zone, one eliminates the unphysical nature of scalar transport resulting from the use of Danckwerts' boundary conditions.

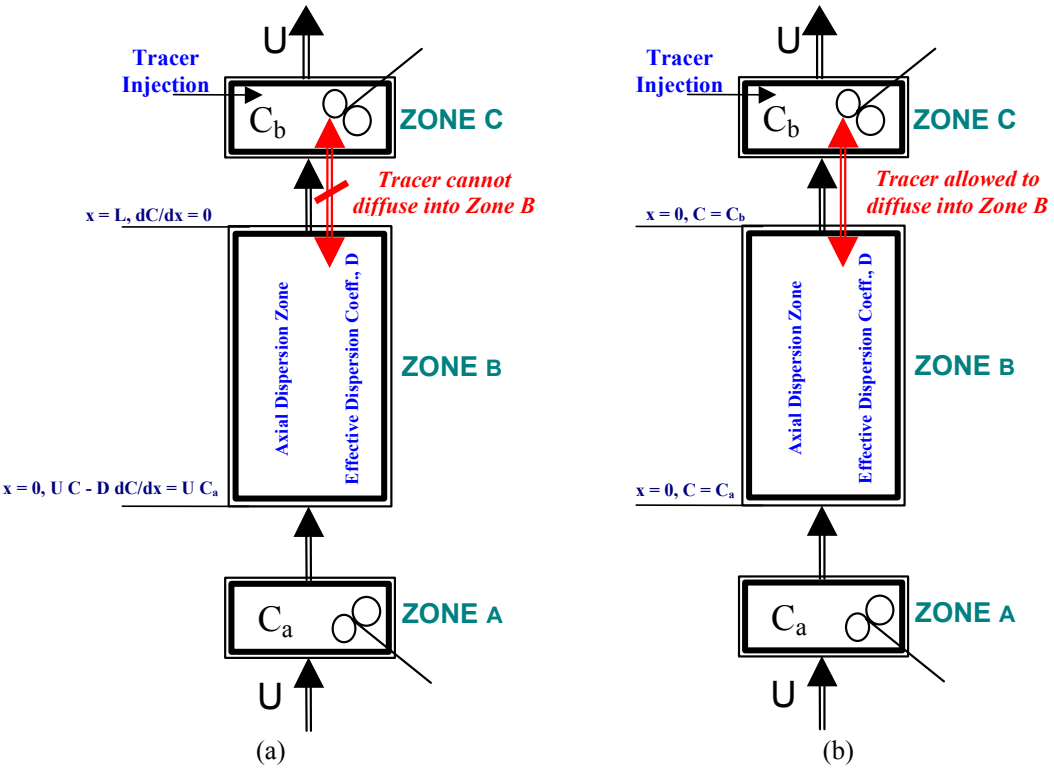


Figure B-1. Schematic of unidirectional flow with the axial dispersion zone imposed with

a) Incorrect Danckwerts' boundary conditions

b) Correct Dirichlet boundary conditions

Much of the earlier work reported using the mixing models reported earlier used the improper Danckwerts' boundary conditions (Degaleesan *et al.*, 1996[a]; Gupta *et al.*,

2001[a]; Gupta *et al*., 2001[b]). Based on the realization of the problem associated with scalar transport arising from the use of the Danckwerts' boundary conditions (depicted in Figure B-1), a revision of the model formulation was accomplished by re-deriving the model equations and boundary conditions based on ***proper*** mass balance at the end zones modeled as perfectly mixed vessels. ***Fortunately, the differences in the simulated responses computed with these alternative boundary conditions are insignificant for the results presented in the earlier work.*** The reason for this is that in the simulated work reported so far, tracer injection always occurred far from the top end zones so that the Danckwerts' boundary conditions approximately hold true. However, these differences could be significant for locations of tracer injections other than the ones used in this study. It is therefore considered important to point out the differences between the correct and incorrect formulations and present example results comparing the two. Table B-1 presents the model equations for the "correct" formulation while Table B-2 does the same for the "incorrect" one.

The partial differential equations describing the species transport in the well-developed zones and presented in Table 6 are not shown here, as they don't change because of the difference in the boundary conditions. However, the formulation of the mass balance in the end zones does change resulting in differences in the model equations as is evident from the two tables. It is noteworthy that the model equations for the end zone CSTs with the physically "correct" boundary conditions have a slightly uncharacteristic form. However, in the limit when the end zone volumes go to zero, the "correct" formulation yields the classical Danckwerts' boundary conditions as can be seen from Tables B-1 and B-2.

Table B-1. Model Equations with "Correct" Boundary Conditions

| **Single Bubble Class Model** |
|---|
| **Gas in the Distributor Zone** |
| $$\frac{dC_{ga}}{dt}=\left\{\begin{array}{l}\frac{U_G}{\bar{\varepsilon}_g\,\phi_{in}\,D_C}C_{g,in}-\frac{U_G}{\bar{\varepsilon}_g\,\phi_{in}\,D_C}C_{ga}+\frac{\bar{\varepsilon}_{g1}}{\bar{\varepsilon}_g\,\phi_{in}\,D_C}\frac{r''^2}{R^2}\overline{D}_{xx_1}\left.\frac{\partial C_{g1}}{\partial x}\right\vert_{x=0}\\ +\frac{\bar{\varepsilon}_{g2}}{\bar{\varepsilon}_g\,\phi_{in}\,D_C}\frac{\left(R^2-r''^2\right)}{R^2}\overline{D}_{xx_2}\left.\frac{\partial C_{g2}}{\partial x}\right\vert_{x=0}-\frac{k_{CST}a_{CST}}{\bar{\varepsilon}_g}\left(HC_{ga}-C_{la}\right)+R_{x,ga}\end{array}\right\}$$ |
| **Liquid in the Distributor Zone** |
| $$\frac{dC_{la}}{dt}=\left\{\begin{array}{l}\frac{U_L}{\bar{\varepsilon}_l\,\phi_{in}\,D_C}C_{l,in}-\frac{U_L}{\bar{\varepsilon}_l\,\phi_{in}\,D_C}C_{la}+\frac{\bar{\varepsilon}_{l1}}{\bar{\varepsilon}_l\,\phi_{in}\,D_C}\frac{r'^2}{R^2}\overline{D}_{xx_1}\left.\frac{\partial C_{l1}}{\partial x}\right\vert_{x=0}\\ +\frac{\bar{\varepsilon}_{l2}}{\bar{\varepsilon}_l\,\phi_{in}\,D_C}\frac{\left(R^2-r'^2\right)}{R^2}\overline{D}_{xx_2}\left.\frac{\partial C_{l2}}{\partial x}\right\vert_{x=0}+\frac{k_{CST}a_{CST}}{\bar{\varepsilon}_l}\left(HC_{ga}-C_{la}\right)+R_{x,la}\end{array}\right\}$$ |
| **Gas in the Disengagement Zone** |
| $$\frac{dC_{gb}}{dt}=\left\{\begin{array}{l}-\frac{\bar{\varepsilon}_{g1}}{\bar{\varepsilon}_g\,\phi_{out}\,D_C}\frac{r''^2}{R^2}\overline{D}_{xx_1}\left.\frac{\partial C_{g1}}{\partial x}\right\vert_{x=L}-\frac{k_{CST}a_{CST}}{\bar{\varepsilon}_g}\left(HC_{gb}-C_{lb}\right)\\ -\frac{\bar{\varepsilon}_{g2}}{\bar{\varepsilon}_g\,\phi_{out}\,D_C}\frac{\left(R^2-r''^2\right)}{R^2}\overline{D}_{xx_2}\left.\frac{\partial C_{g2}}{\partial x}\right\vert_{x=L}+R_{x,gb}\end{array}\right\}$$ |
| **Liquid in the Disengagement Zone** |
| $$\frac{dC_{lb}}{dt}=\left\{\begin{array}{l}-\frac{\bar{\varepsilon}_{l1}}{\bar{\varepsilon}_l\,\phi_{out}\,D_C}\frac{r'^2}{R^2}\overline{D}_{xx_1}\left.\frac{\partial C_{l1}}{\partial x}\right\vert_{x=L}+\frac{k_{CST}a_{CST}}{\bar{\varepsilon}_l}\left(HC_{gb}-C_{lb}\right)\\ -\frac{\bar{\varepsilon}_{l2}}{\bar{\varepsilon}_l\,\phi_{out}\,D_C}\frac{\left(R^2-r'^2\right)}{R^2}\overline{D}_{xx_2}\left.\frac{\partial C_{l2}}{\partial x}\right\vert_{x=L}+R_{x,lb}\end{array}\right\}$$ |
| |
| ***Boundary Conditions for the Well-Developed Flow Zones*** |
| ***Up-Flowing Gas*** |
| $C_{g1}\vert_{x=0}=C_{ga}\qquad C_{g1}\vert_{x=L}=C_{gb}$ |
| ***Up-Flowing Liquid*** |
| $C_{l1}\vert_{x=0}=C_{la}\qquad C_{l1}\vert_{x=L}=C_{lb}$ |
| ***Down-Flowing Gas*** |
| $C_{g2}\vert_{x=0}=C_{ga}\qquad C_{g2}\vert_{x=L}=C_{gb}$ |
| ***Down-Flowing Liquid*** |
| $C_{l2}\vert_{x=0}=C_{la}\qquad C_{l2}\vert_{x=L}=C_{lb}$ |

Table B-2. Model Equations with "Incorrect" Boundary Conditions

| **Single Bubble Class Model** |
|---|
| **Gas in the Distributor Zone** |
| $$\frac{dC_{ga}}{dt}=\left\{\begin{array}{l}\dfrac{\bar{\varepsilon}_{g2}\bar{u}_{g2}}{\bar{\varepsilon}_g\phi_{in}D_C}\dfrac{\left(R^2-r''^2\right)}{R^2}C_{g2}\Big\vert_{x=0}-\dfrac{\bar{\varepsilon}_{g1}\bar{u}_{g1}}{\bar{\varepsilon}_g\phi_{in}D_C}\dfrac{r''^2}{R^2}C_{ga}\\ +\dfrac{U_G}{\bar{\varepsilon}_g\phi_{in}D_C}C_{g,in}-\dfrac{k_{CST}a_{CST}}{\bar{\varepsilon}_g}\left(HC_{ga}-C_{la}\right)+R_{x,ga}\end{array}\right\}$$ |
| **Liquid in the Distributor Zone** |
| $$\frac{dC_{la}}{dt}=\left\{\begin{array}{l}\dfrac{\bar{\varepsilon}_{l2}\bar{u}_{l2}}{\bar{\varepsilon}_l\phi_{in}D_C}\dfrac{\left(R^2-r'^2\right)}{R^2}C_{l2}\Big\vert_{x=0}-\dfrac{\bar{\varepsilon}_{l1}\bar{u}_{l1}}{\bar{\varepsilon}_l\phi_{in}D_C}\dfrac{r'^2}{R^2}C_{la}\\ +\dfrac{U_L}{\bar{\varepsilon}_l\phi_{in}D_C}C_{l,in}+\dfrac{k_{CST}a_{CST}}{\bar{\varepsilon}_l}\left(HC_{ga}-C_{la}\right)+R_{x,la}\end{array}\right\}$$ |
| **Gas in the Disengagement Zone** |
| $$\frac{dC_{gb}}{dt}=\left\{\begin{array}{l}\dfrac{\bar{\varepsilon}_{g1}\bar{u}_{g1}}{\bar{\varepsilon}_g\phi_{out}D_C}\dfrac{r''^2}{R^2}C_{g1}\Big\vert_{x=L}-\dfrac{\bar{\varepsilon}_{g2}\bar{u}_{g2}}{\bar{\varepsilon}_g\phi_{out}D_C}\dfrac{\left(R^2-r''^2\right)}{R^2}C_{gb}\\ -\dfrac{U_G}{\bar{\varepsilon}_g\phi_{out}D_C}C_{gb}-\dfrac{k_{CST}a_{CST}}{\bar{\varepsilon}_g}\left(HC_{gb}-C_{lb}\right)+R_{x,gb}\end{array}\right\}$$ |
| **Liquid in the Disengagement Zone** |
| $$\frac{dC_{lb}}{dt}=\left\{\begin{array}{l}\dfrac{\bar{\varepsilon}_{l1}\bar{u}_{l1}}{\bar{\varepsilon}_l\phi_{out}D_C}\dfrac{r'^2}{R^2}C_{l1}\Big\vert_{x=L}-\dfrac{\bar{\varepsilon}_{l2}\bar{u}_{l2}}{\bar{\varepsilon}_l\phi_{out}D_C}\dfrac{\left(R^2-r'^2\right)}{R^2}C_{lb}\\ -\dfrac{U_L}{\bar{\varepsilon}_l\phi_{out}D_C}C_{lb}+\dfrac{k_{CST}a_{CST}}{\bar{\varepsilon}_l}\left(HC_{gb}-C_{lb}\right)+R_{x,lb}\end{array}\right\}$$ |
| ***Boundary Conditions for the Well-Developed Flow Zones*** |
| ***Up-Flowing Gas*** |
| $$\bar{u}_{g1}C_{g1}\vert_{x=0}-\bar{D}_{xx_1}\left.\frac{\partial C_{g1}}{\partial x}\right\vert_{x=0}=\bar{u}_{g1}C_{ga}\qquad\left.\frac{\partial C_{g1}}{\partial x}\right\vert_{x=L}=0$$ |
| ***Up-Flowing Liquid*** |
| $$\bar{u}_{l1}C_{l1}\vert_{x=0}-\bar{D}_{xx_1}\left.\frac{\partial C_{l1}}{\partial x}\right\vert_{x=0}=\bar{u}_{l1}C_{la}\qquad\left.\frac{\partial C_{l1}}{\partial x}\right\vert_{x=L}=0$$ |
| ***Down-Flowing Gas*** |
| $$\bar{u}_{g2}C_{g2}\vert_{x=L}+\bar{D}_{xx_2}\left.\frac{\partial C_{g2}}{\partial x}\right\vert_{x=L}=\bar{u}_{g2}C_{gb}\qquad\left.\frac{\partial C_{g2}}{\partial x}\right\vert_{x=0}=0$$ |
| ***Down-Flowing Liquid*** |
| $$\bar{u}_{l2}C_{l2}\vert_{x=L}+\bar{D}_{xx_2}\left.\frac{\partial C_{l2}}{\partial x}\right\vert_{x=L}=\bar{u}_{l2}C_{lb}\qquad\left.\frac{\partial C_{l2}}{\partial x}\right\vert_{x=0}=0$$ |

In view of Tables B-1 and B-2, one can understand the pitfalls resulting from the use of the "old" Danckwerts' boundary conditions. To further elaborate on the problem associated with the Danckwerts' boundary conditions similar to that depicted in Figure B-1, let us consider the transport of a non-volatile liquid tracer for the reactor compartmentalization presented earlier in this report. To accentuate the effect of the incorrect boundary conditions on the computed response, let us further assume that there is no cross-flow exchange between the up-flowing and down-flowing liquid zones. Then, based on the imposed old Danckwerts' boundary condition at x = L of $\partial C_{l1}/\partial x = 0$, a liquid tracer injected into the disengagement CST at the top of the column could not propagate into the well developed up-flow region until it is transported through the down-flow region and appears into the up-flow region from the bottom. In reality, however, axial diffusion of the tracer injected into the stirred tank at the top would immediately cause it to diffuse against the flow, since the concentration at the top of the up-flow region is the same as that in the disengagement CST. This is reflected in the correct boundary condition of $C_{l1} = C_{lb}$ at x = L. The effects described above can be clearly seen from Figure B-2 which shows the simulation results computed using the "Old" and the "New" boundary conditions for a hypothetical situation of a liquid tracer injected in the disengagement CST with the operating conditions being those for Run 16.7. It can be shown that for tracer injections close to the bottom of the column, however, both types of conditions lead to almost the same results.

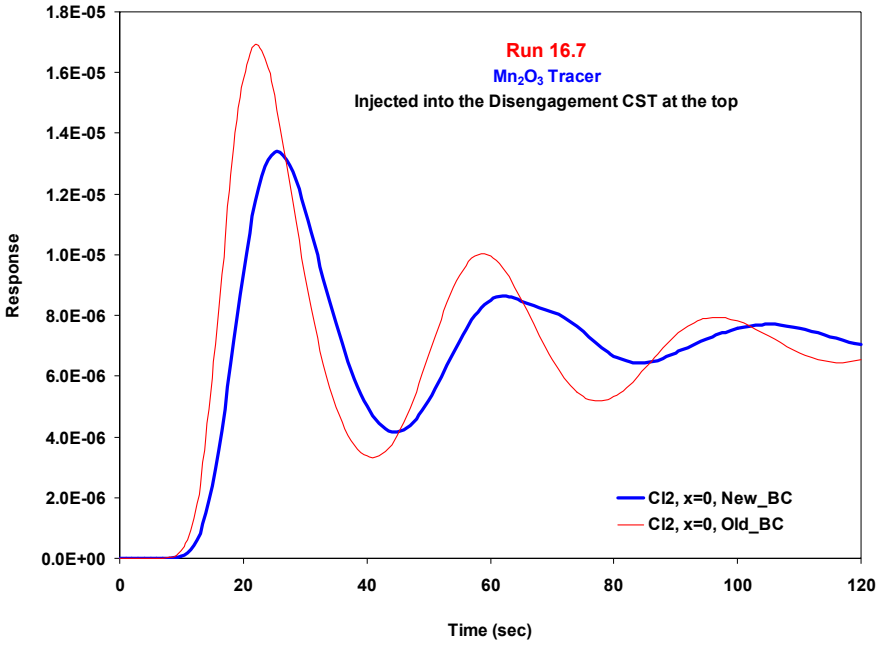


(a)

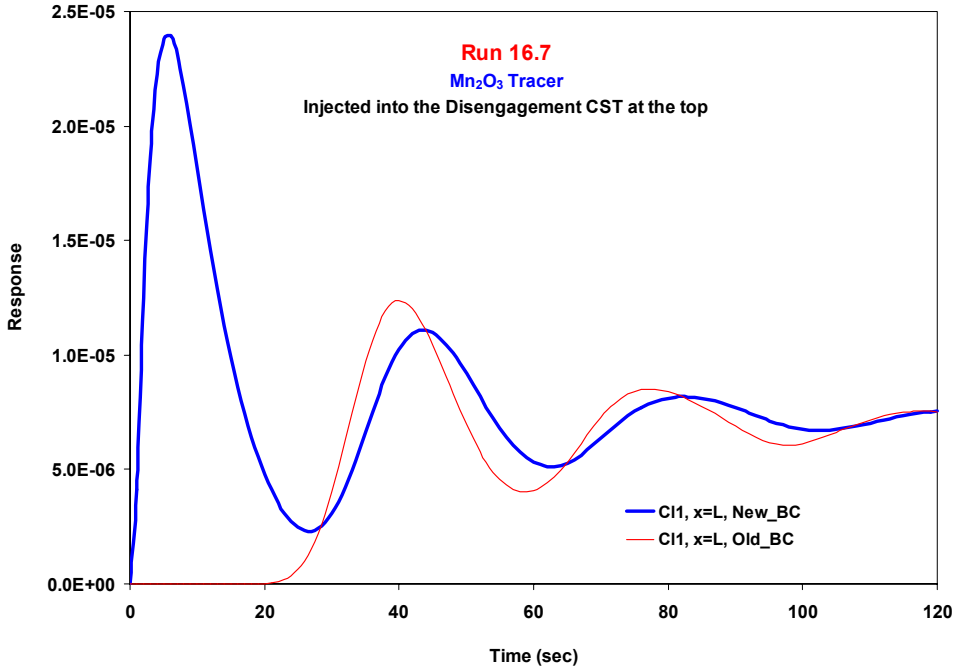


(b)

Figure B-2. Hypothetical case of "liquid-like" ($Mn_2O_3$) tracer injection in the disengagement CST. Tracer concentration a) at the bottom-end of the down-flow zone b) at the top-end of the up-flow zone.

The effect of these two alternate boundary condition formulations on the computed tracer responses is further illustrated in the Figures B-3 and B-4. For the purposes of these demonstrations, the examples chosen are the simulation of the tracer responses for Runs 16.6 and 16.7. Measurement levels "Lev1" (13.5" on outside tape), "Lev4" (116" on outside tape) and "Lev8" (215" on outside tape) as shown in Figure 7 were chosen for the purposes of this examination.

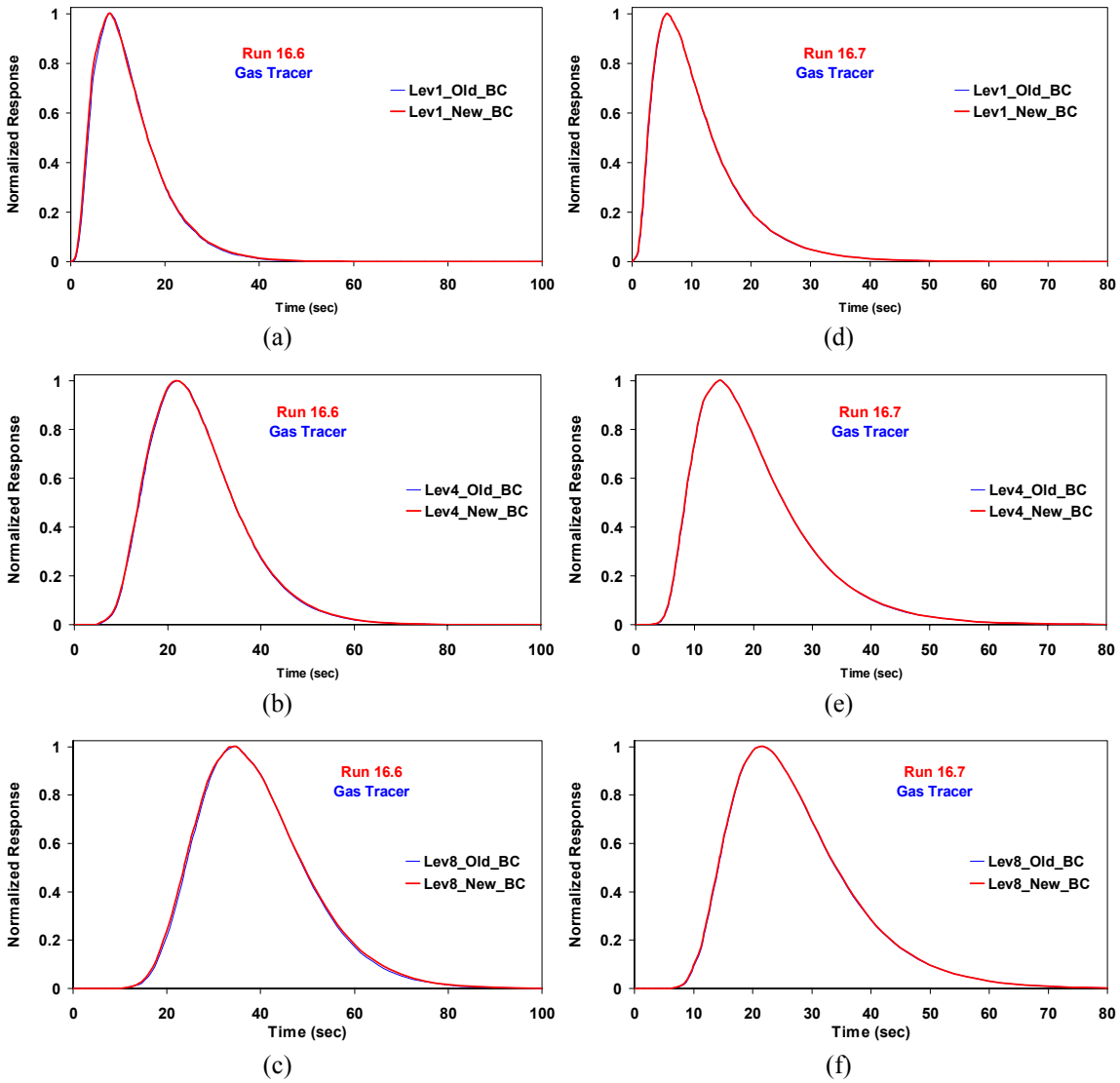


Figure B-3. Effect of alternate boundary conditions on FT-IV gas tracer responses.

In the figures showing this comparison (Figures B-3 and B-4), "Old_BC" refers to the "incorrect" Danckwerts' boundary conditions while "New_BC" refers to the "correct" Dirichlet boundary conditions. It can be concluded from Figure B-3 that the change in boundary conditions has a negligible effect on simulated responses computed from the gas phase mixing model for the experimental conditions of this study.

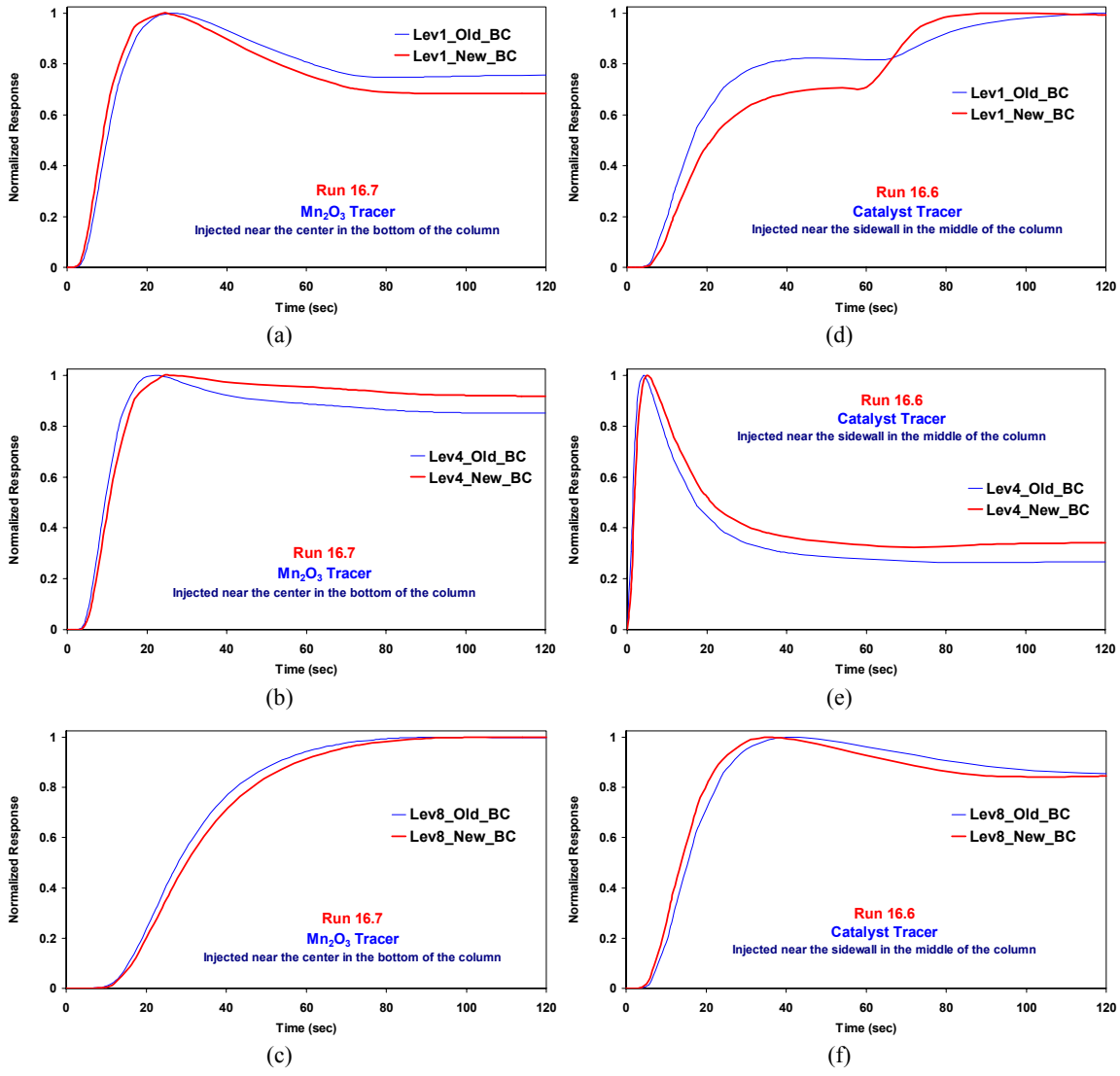


Figure B-4. Effect of alternate boundary conditions on FT-IV "liquid-like" ($Mn_2O_3$) and catalyst tracer responses.

Figure B-4 (a-c) show the effect of the "old" and "new" boundary conditions on the "liquid-like" tracer responses corresponding to Run 16.7 while Figure B-4 (d-f) shows those for the catalyst tracer responses corresponding to Run 16.6. It can be seen from these figures that for the liquid mixing simulations, the difference exists but is not significant except for Level-1 of Run 16.6 for the catalyst where the difference is quite pronounced. Since this was the low superficial gas velocity case, it is not surprising that the effect of improper boundary conditions is magnified due to slower mixing.

In conclusion, it can be seen that it is vital to impose correct boundary conditions at the end of the well-developed zones pertinent to the reactor compartmentalization based on the models developed in this study. The effect of the boundary conditions is insignificant when the tracer is injected into the reactor inlet, as was the case for the gas tracer injections. However, when the tracer injection point is anywhere other than the inlet stream or the inlet CST, the effect of the use of incorrect boundary conditions would be encountered. This effect would increasingly worsen as the tracer injection point is moved closer to the outlet of the well-developed zones. For much of the earlier work reported by Degaleesan (1997) on the liquid and catalyst tracer tests during the methanol runs, since the majority of tracer mixing was due to the recirculatory flow of the liquid/slurry phase, the effect of the incorrect boundary conditions on the computed responses would be minimal. However, for unidirectional flows or recirculatory flows with no cross-mixing and tracer injection close to the exit, major problems would arise as shown in Figure B-2. Thus, realizing the problem with the use of incorrect Danckwerts' boundary conditions, all tracer responses reported in this study were recomputed with the correct "Dirichlet" boundary conditions and contain no artifact originating from the use of Danckwerts' boundary conditions.

# Appendix C. Comparison of FT-IV Experimental Data with Simulation Results from Mixing Models

This appendix presents the comparison of simulation results from mixing models with experimental data ***at every axial level*** for the FT-IV tracer tests conducted at the AFDU. These are being presented here for the sake of completeness since only selected results relevant to the discussion were presented in main body of this report.

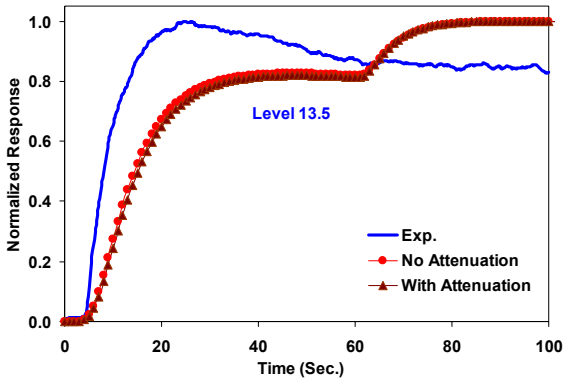

(a)

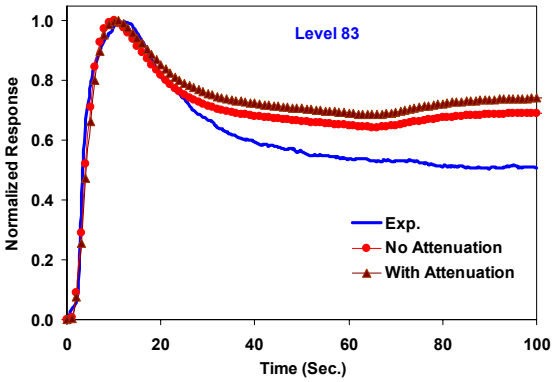

(c)

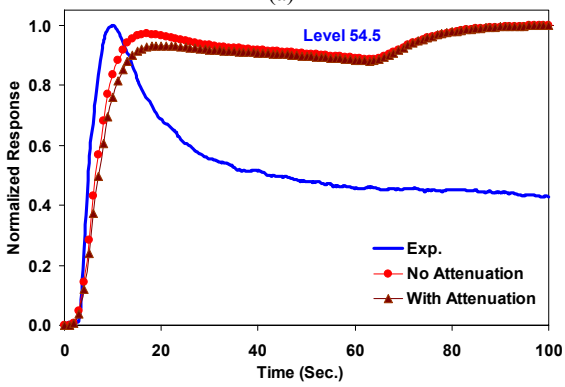

(b)

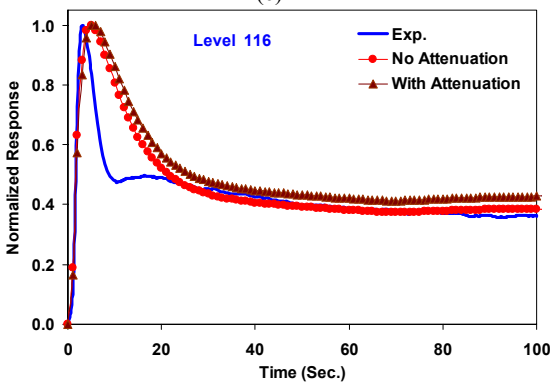

(d)

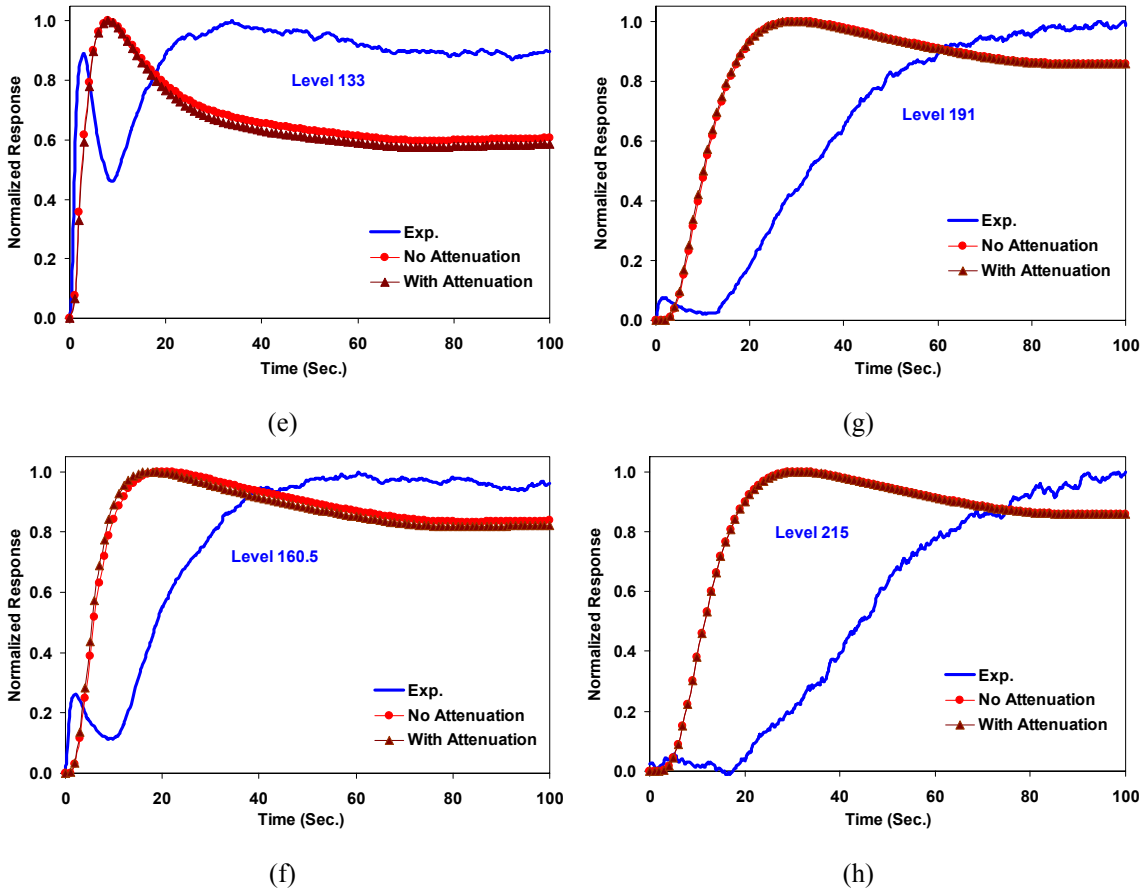


Figure C-1. Comparison of experimental and simulated tracer responses for Run 16.6 (Tracer: - Catalyst; Injection Pt.: - Sidewall-Middle).

In Figure C-1 as well as in all the rest of the figures in this appendix, sub-figures (a)-(h) represent the eight detector levels where measurements were taken and comparison with simulations from mixing models are reported. From Figure C-1, it can be seen that the comparison of the simulations results with data is poor. As mentioned earlier , for the sidewall injection of liquid-like or catalyst tracer and especially for the operating conditions of Run 16.6, the assumptions of mixing models are probably violated severely resulting in poor comparison of simulations with data.

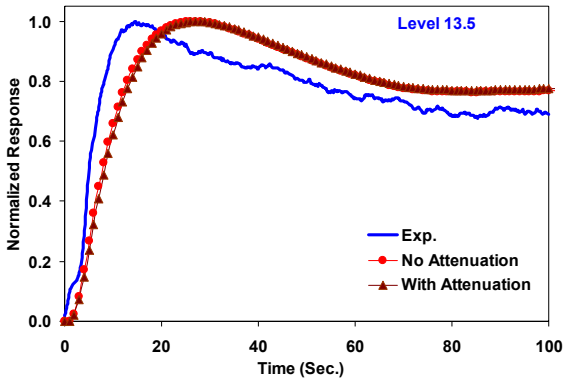
Level 13.5
Normalized Response
Time (Sec.)
Exp.
No Attenuation
With Attenuation

(a)

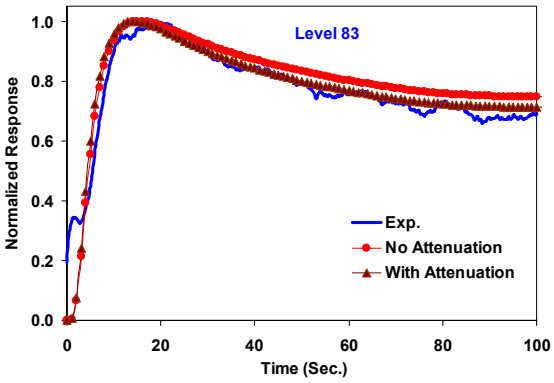
Level 83
Normalized Response
Time (Sec.)
Exp.
No Attenuation
With Attenuation

(c)

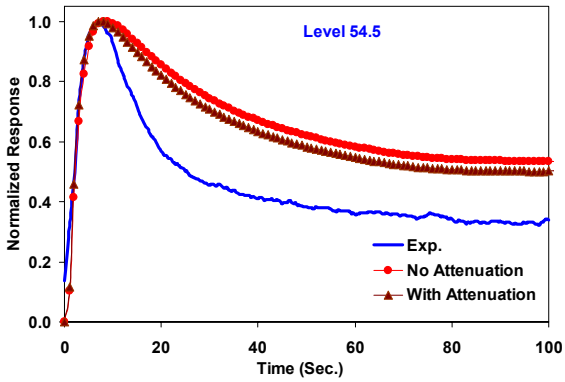
Level 54.5
Normalized Response
Time (Sec.)
Exp.
No Attenuation
With Attenuation

(b)

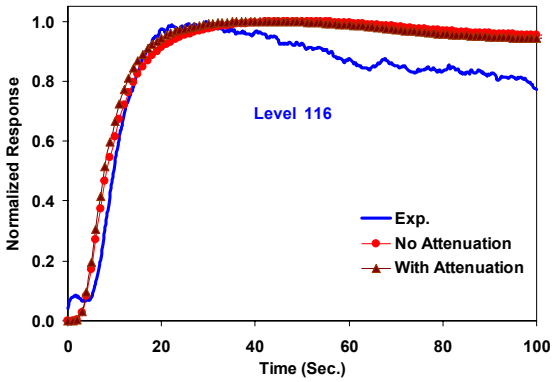
Level 116
Normalized Response
Time (Sec.)
Exp.
No Attenuation
With Attenuation

(d)

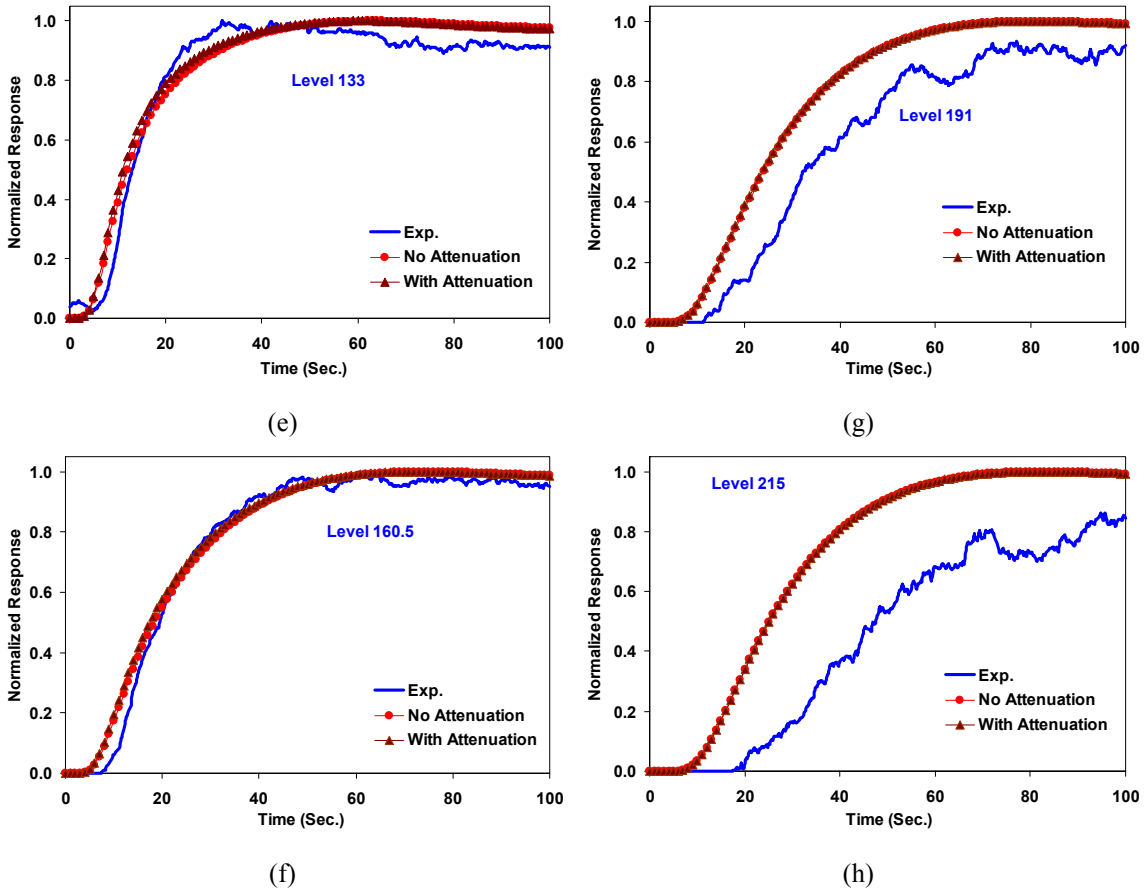


Figure C-2. Comparison of experimental and simulated tracer responses for Run 16.6 (Tracer: - Catalyst; Injection Pt.: - Center-Bottom).

Figure C-2 shows the comparison of experimental and simulated tracer responses for the catalyst tracer injected in the bottom-center location. As mentioned earlier, this is a preferred injection location as it is further away from the slurry exit. Consequently, the model assumptions of axisymmetry are valid to a greater extent, and this is evident from a substantially improved agreement between simulations and data. For the two highest detector-levels (191 and 215 inches as referenced on the outside tape) however, the experimental responses are still much delayed in time compared to simulations. This points to the presence of a foamy two-phase mixture at the very top of the liquid-slurry dispersion with the density of foam increasing from level 191 to level 215.

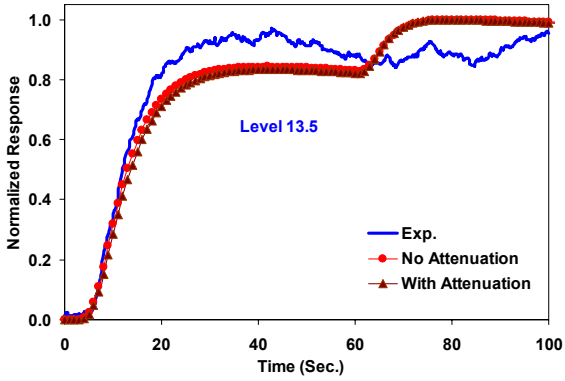
Level 13.5
Exp.
No Attenuation
With Attenuation
Normalized Response
Time (Sec.)

(a)

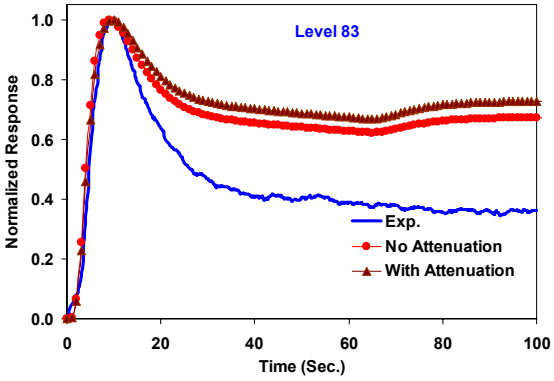
Level 83
Exp.
No Attenuation
With Attenuation
Normalized Response
Time (Sec.)

(c)

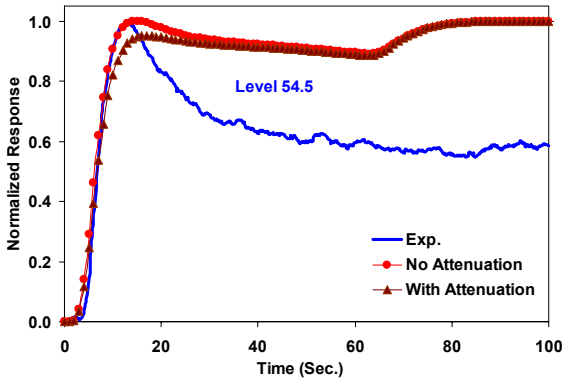
Level 54.5
Exp.
No Attenuation
With Attenuation
Normalized Response
Time (Sec.)

(b)

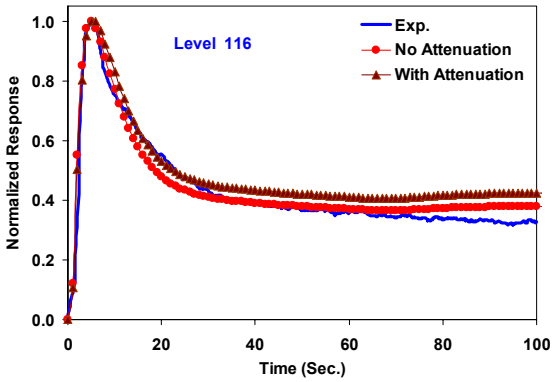
Level 116
Exp.
No Attenuation
With Attenuation
Normalized Response
Time (Sec.)

(d)

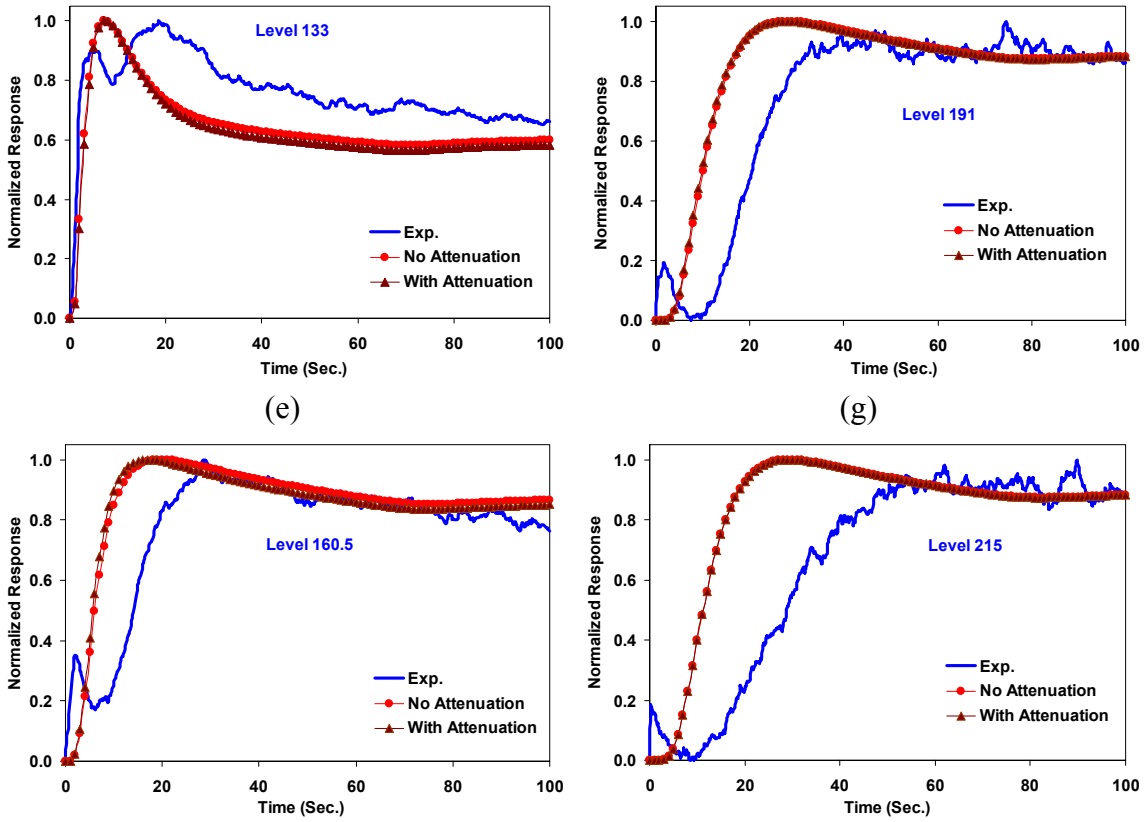


Figure C-3. Comparison of experimental and simulated tracer responses for Run 16.7 (Tracer: - Catalyst; Injection Pt.: - Sidewall-Middle).

Figure C-3 shows the comparison of the experimental as simulated tracer responses for the middle-sidewall injection of the catalyst tracer during Run 16.7. As for Run 16.6, the general agreement between simulated and experimental responses is not good, however it is much better than that for run 16.6. This is due to the higher superficial gas velocity employed during Run 16.7 which results in better radial mixing and consequently better realization of the liquid mixing model assumptions compared to Run 16.6.

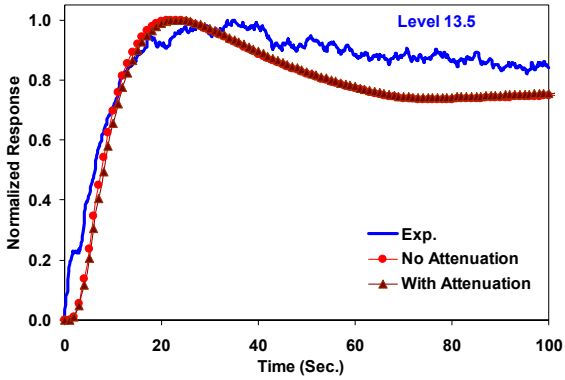
Level 13.5
Normalized Response
Time (Sec.)
Exp.
No Attenuation
With Attenuation

(a)

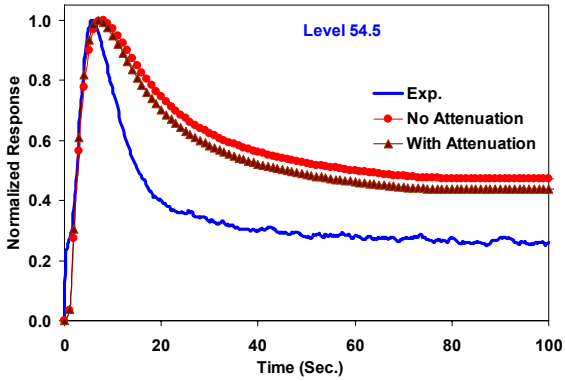
Level 54.5
Normalized Response
Time (Sec.)
Exp.
No Attenuation
With Attenuation

(b)

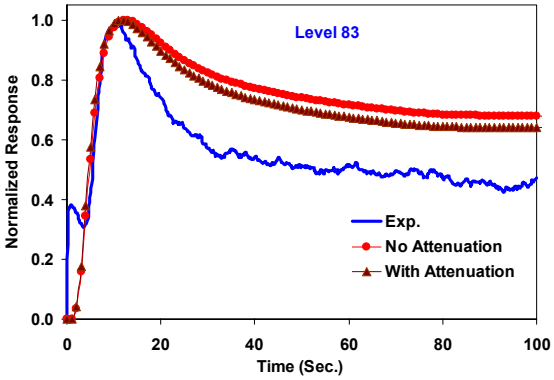
Level 83
Normalized Response
Time (Sec.)
Exp.
No Attenuation
With Attenuation

(c)

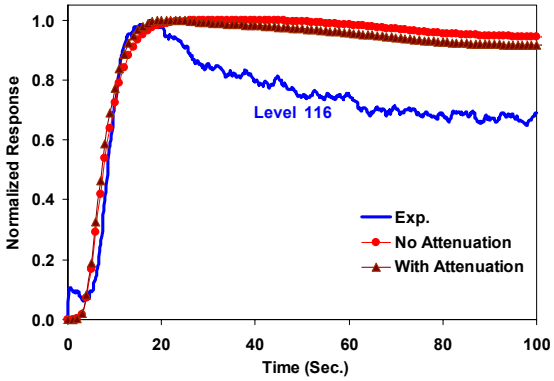
Level 116
Normalized Response
Time (Sec.)
Exp.
No Attenuation
With Attenuation

(d)

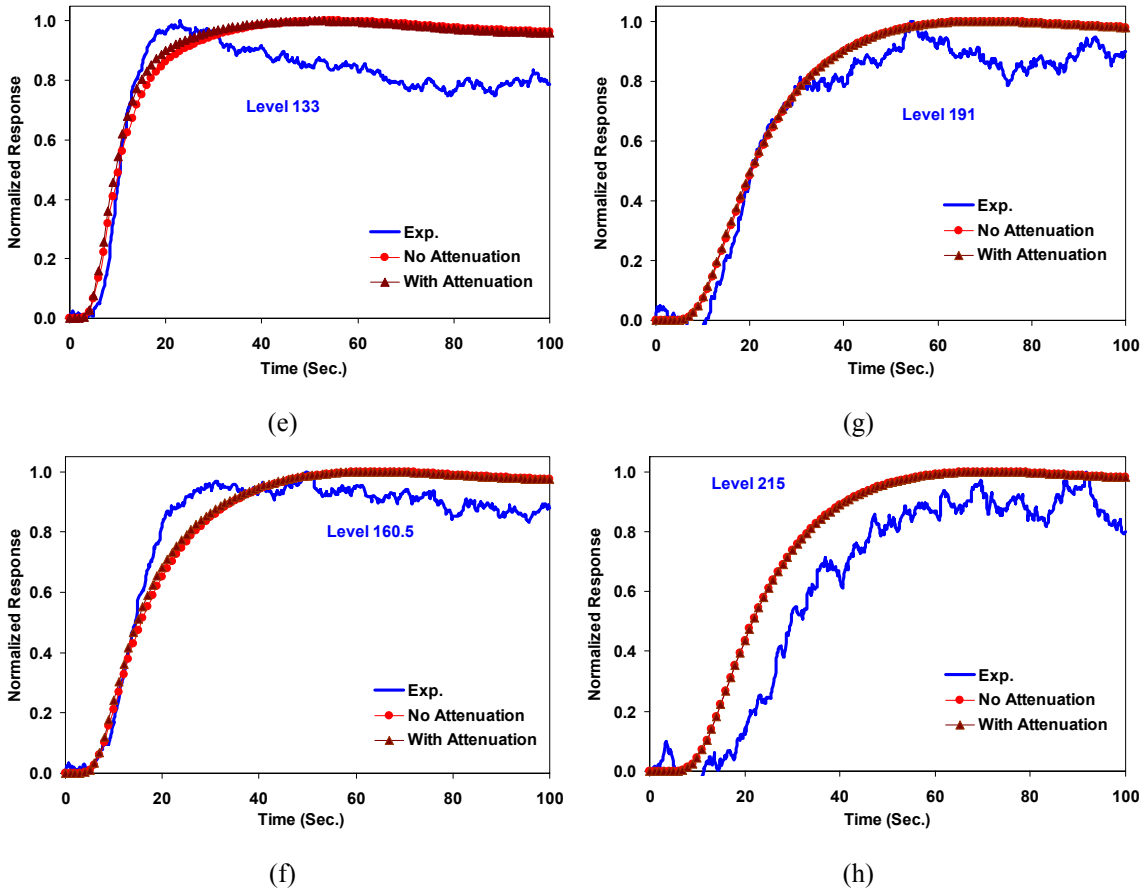


Figure C-4. Comparison of experimental and simulated tracer responses for Run 16.7 (Tracer: - Catalyst; Injection Pt.: - Center-Bottom).

Figure C-4 provides a comparison of the experimental and simulated responses for the catalyst tracer injected into the bottom-center of the reactor. As for Run 16.6, the agreement between simulations and data is much better as compared to the middle-sidewall injection of the tracer. In addition, the higher superficial gas velocity of Run 16.7 also provides for a relatively quicker radial mixing of the tracer than that for Run 16.6. This implies that model assumptions are better satisfied in Run 16.7 than in Run 16.6 and consequently leads to better agreement between simulations and data. Furthermore, since the operating conditions of Run 16.6 may be closer to transition, there exists additional uncertainty with regards to the realization of the model assumption for this case.

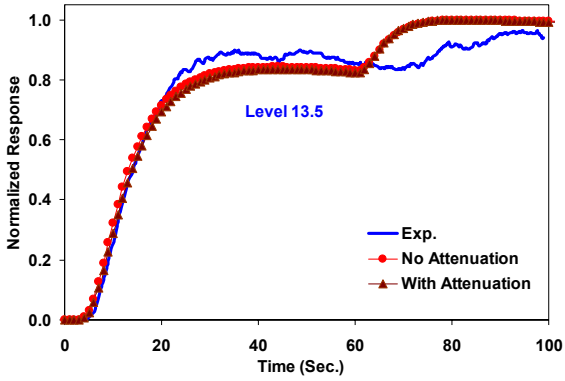
Level 13.5
Exp.
No Attenuation
With Attenuation
Normalized Response
Time (Sec.)

(a)

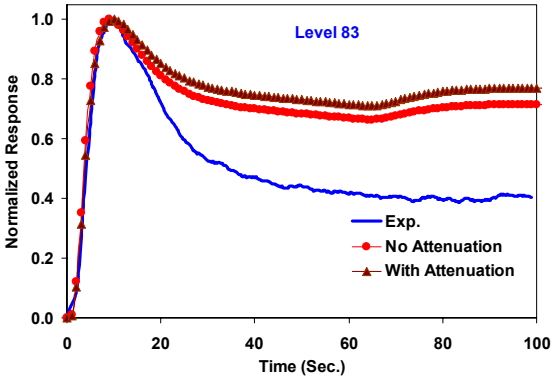
Level 83
Exp.
No Attenuation
With Attenuation
Normalized Response
Time (Sec.)

(c)

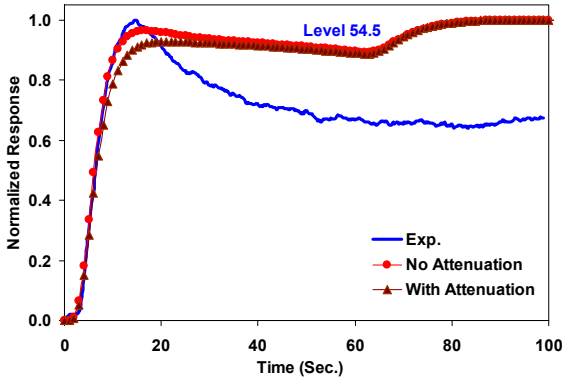
Level 54.5
Exp.
No Attenuation
With Attenuation
Normalized Response
Time (Sec.)

(b)

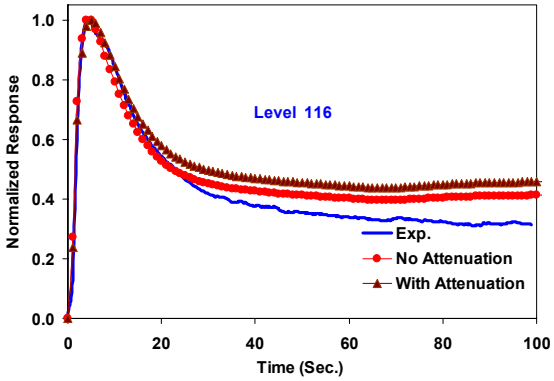
Level 116
Exp.
No Attenuation
With Attenuation
Normalized Response
Time (Sec.)

(d)

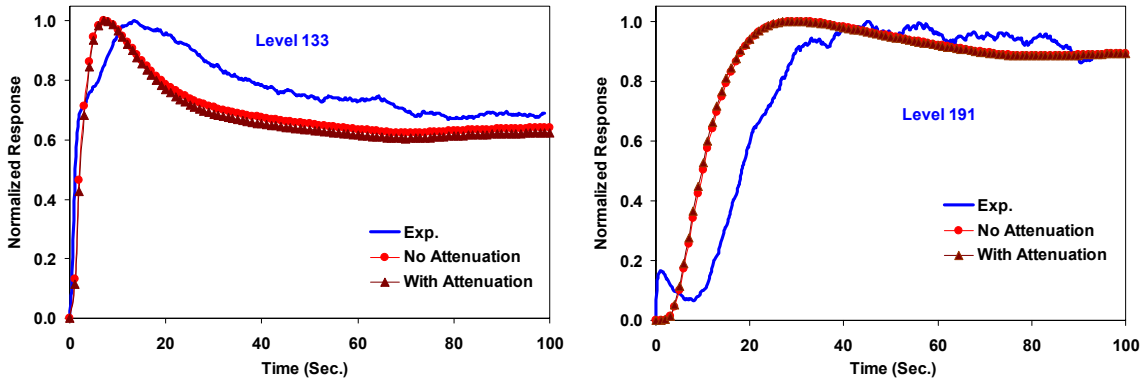


(e)




(g)

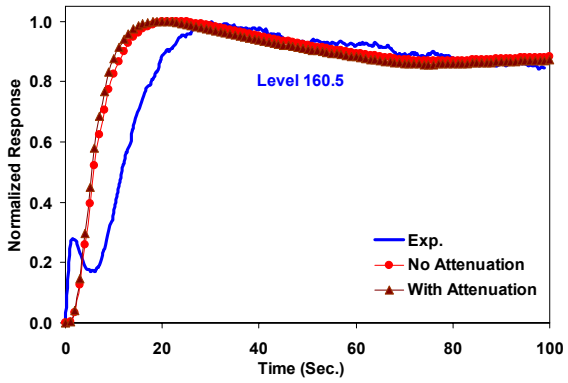


(f)

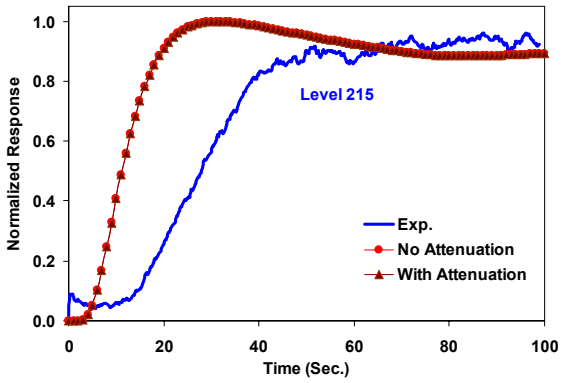


(h)

Figure C-5. Comparison of experimental and simulated tracer responses for Run 16.7 (Tracer: - $Mn_2O_3$; Injection Pt.: - Sidewall-Middle).

The trends in the comparison of experimental responses with simulations in Figure C-5 are a reflection of the trends observed in Figure C-3 for the same operating conditions but using the $Mn_2O_3$ tracer instead of the catalyst tracer. In general, the agreement between simulations and experiments is fair for the lower four levels and deteriorates for the top four levels. This is most likely due to the dynamics originating from the presence of the slurry outlet in the middle of the column as well as the possible existence of a foamy structure near the top of the gas-slurry dispersion.

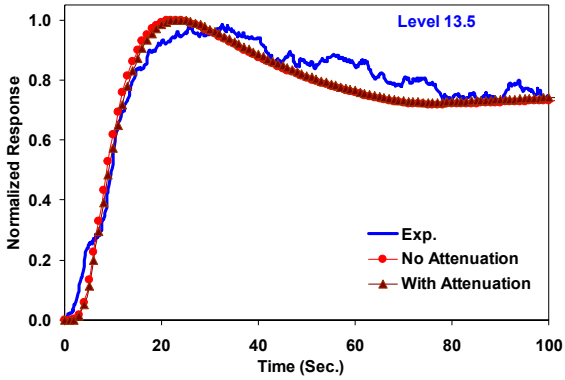
Level 13.5
Normalized Response
Time (Sec.)
Exp.
No Attenuation
With Attenuation

(a)

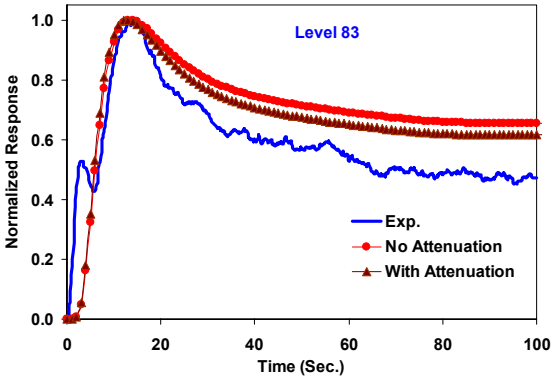
Level 83
Normalized Response
Time (Sec.)
Exp.
No Attenuation
With Attenuation

(c)

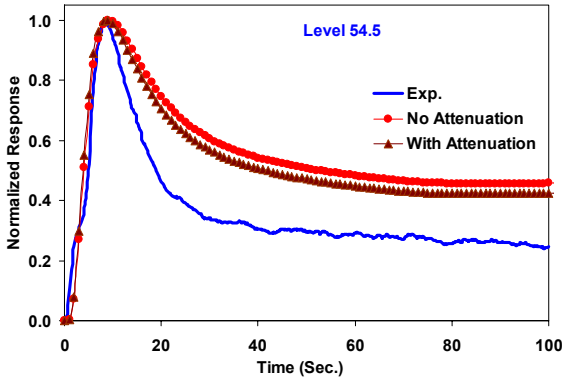
Level 54.5
Normalized Response
Time (Sec.)
Exp.
No Attenuation
With Attenuation

(b)

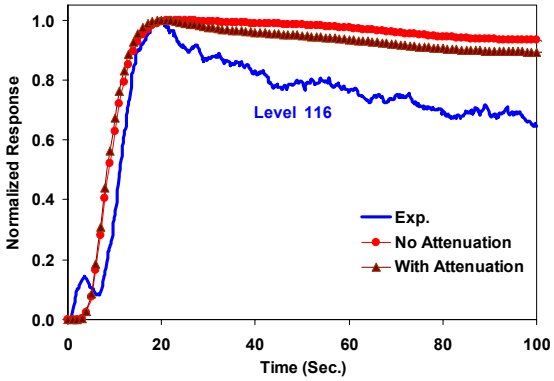
Level 116
Normalized Response
Time (Sec.)
Exp.
No Attenuation
With Attenuation

(d)

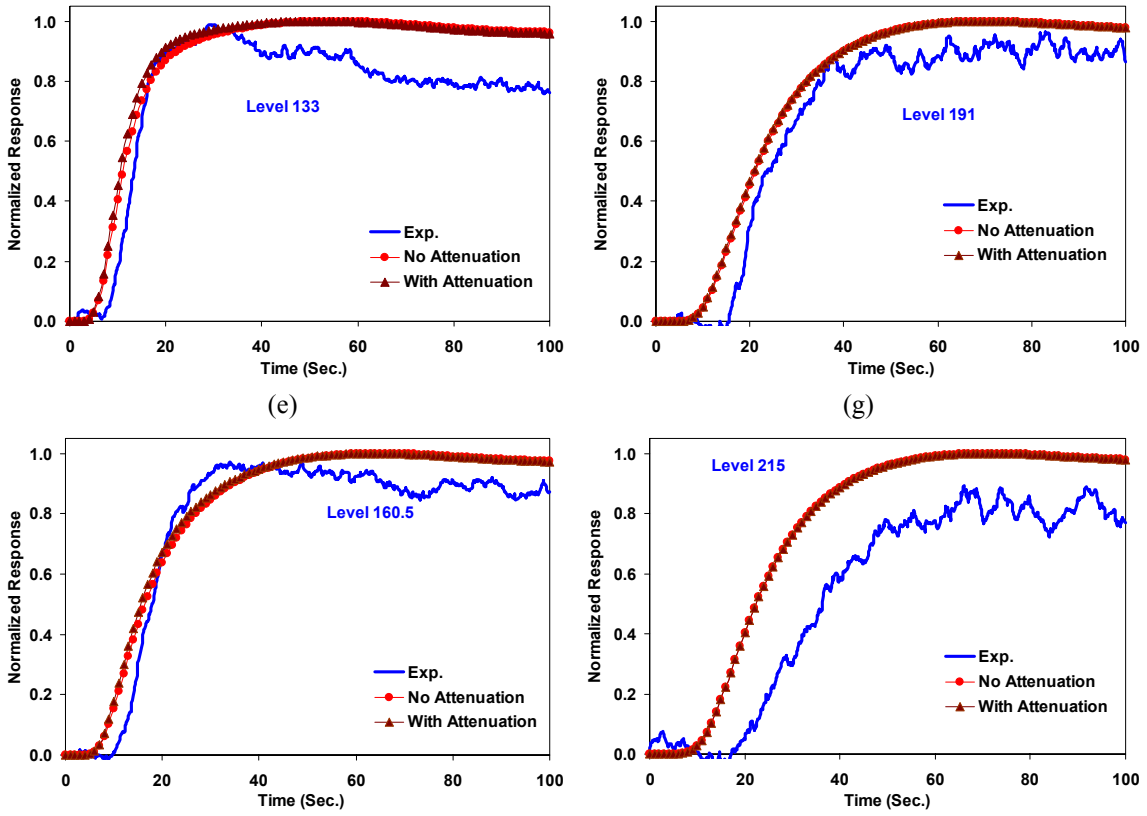


Figure C-6. Comparison of experimental and simulated tracer responses for Run 16.7 (Tracer: - $Mn_2O_3$; Injection Pt.: - Center-Bottom).

Figure C-6 provides comparison of the simulated and experimental responses for the $Mn_2O_3$ tracer injected into the bottom-center of the reactor. Given the nature of the tracer, the point of its injection as well as the operating conditions of Run 16.7, this experiment was most likely to satisfy the maximum number of assumptions of the mixing model among all the liquid/catalyst tracer experiments that were performed. This is evident from the best comparison between experiments and simulations among all the liquid/catalyst tracer tests. Interestingly, even the comparison at level 191 is reasonably good, which was not the case for the catalyst tracer. This points to the better ability of the $Mn_2O_3$ tracer to follow the liquid phase as compared to the catalyst tracer that seems to have difficulties following the liquid/slurry phase as one approaches the top of the gas-

slurry dispersion. As mentioned earlier, this is the result of the larger particle size of the catalyst as compared to $Mn_2O_3$ tracer.

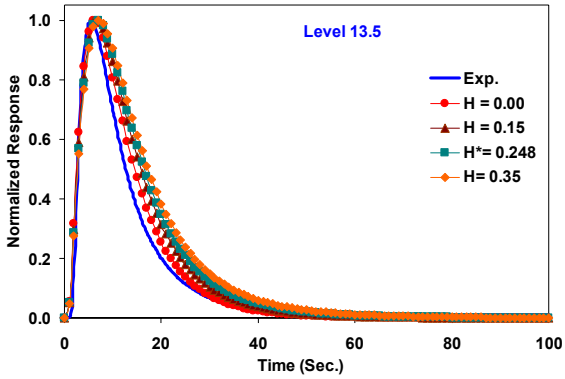


(a)

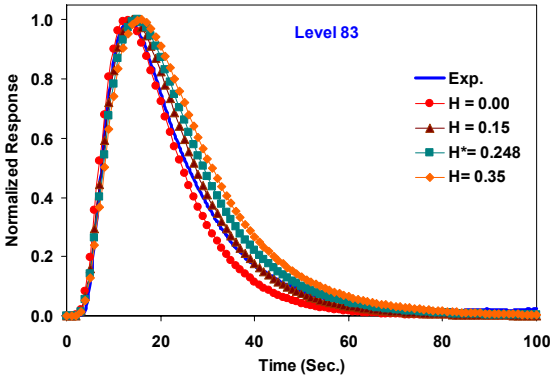


(c)

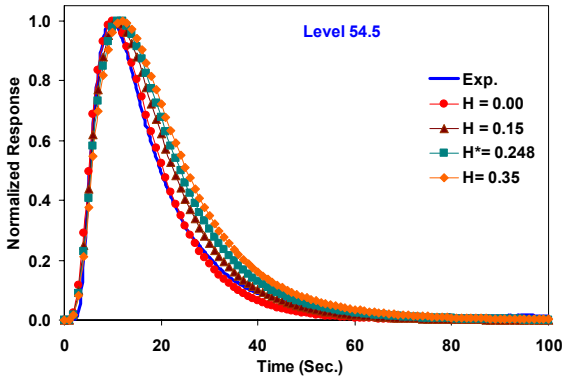


(b)

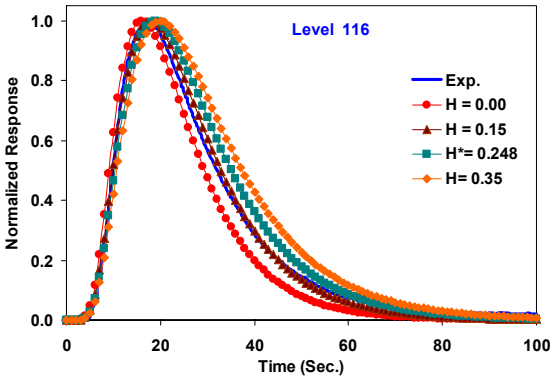


(d)

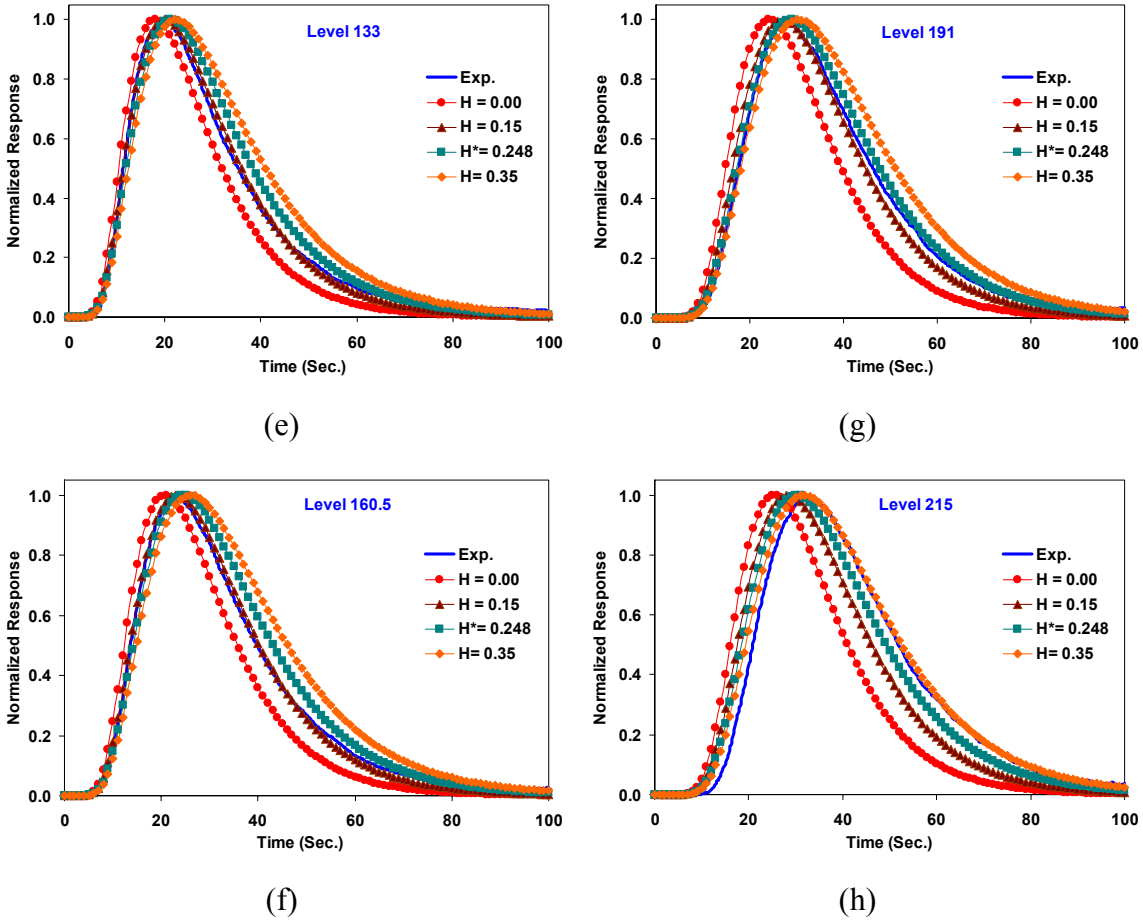


Figure C-7. Comparison of experimental and simulated gas tracer response curves for Run 16.6 for different Henry's constants.

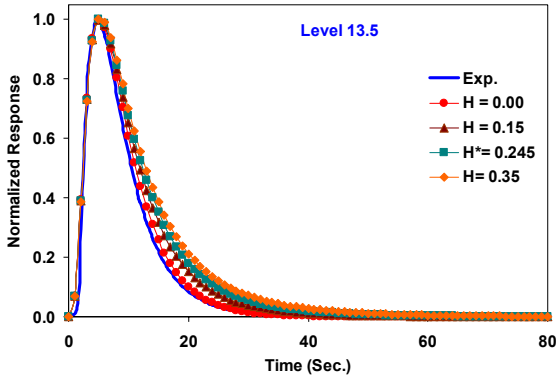
Level 13.5
Exp.
H = 0.00
H = 0.15
H*= 0.245
H= 0.35
Normalized Response
Time (Sec.)
0.0
0.2
0.4
0.6
0.8
1.0
0
20
40
60
80

(a)

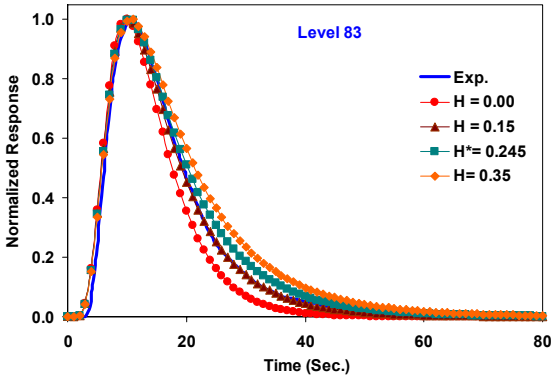
Level 83
Exp.
H = 0.00
H = 0.15
H*= 0.245
H= 0.35
Normalized Response
Time (Sec.)
0.0
0.2
0.4
0.6
0.8
1.0
0
20
40
60
80

(c)

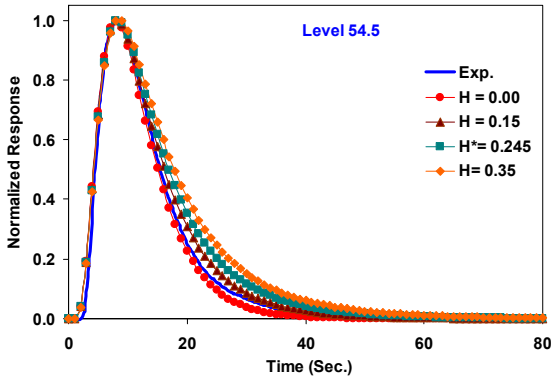
Level 54.5
Exp.
H = 0.00
H = 0.15
H*= 0.245
H= 0.35
Normalized Response
Time (Sec.)
0.0
0.2
0.4
0.6
0.8
1.0
0
20
40
60
80

(b)

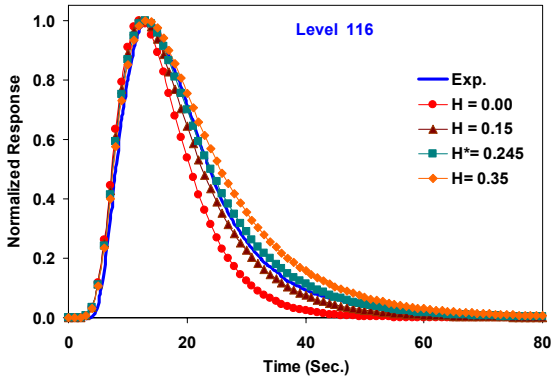
Level 116
Exp.
H = 0.00
H = 0.15
H*= 0.245
H= 0.35
Normalized Response
Time (Sec.)
0.0
0.2
0.4
0.6
0.8
1.0
0
20
40
60
80

(d)

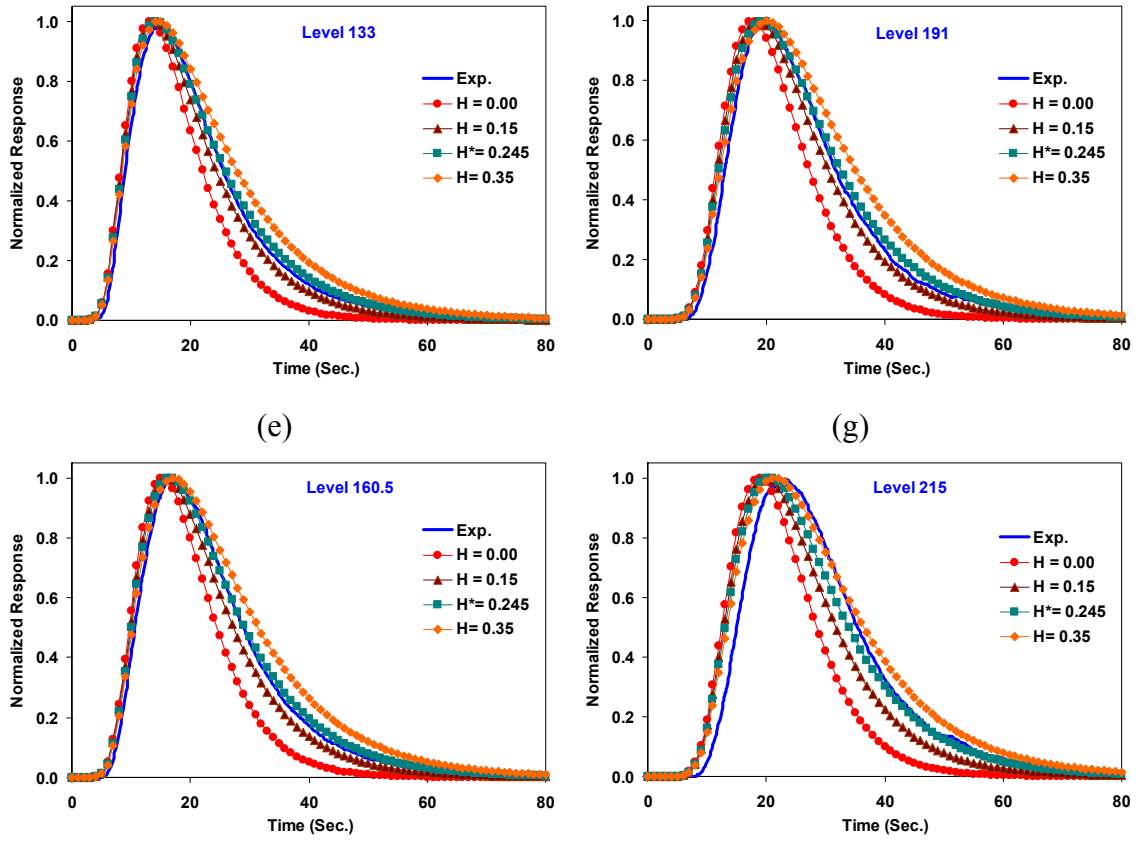


(e) (g)

(f) (h)

Figure C-8. Comparison of experimental and simulated gas tracer response curves for Run 16.7 for different Henry's constants.

Figures C-7 and C-8 provide a comparison of the experimental and simulated gas tracer responses for Runs 16.6 and 16.7 respectively. From the figures one can see that in general, for the thermodynamically estimated Henry's constant (H*), the agreement between experiments and data is very good except for level 215 where the experimental response seems to have been delayed. This is observed in both Runs 16.6 and 16.7, and was also noticed in all the liquid/catalyst tracer tests, all pointing to the presence of a froth at the gas-slurry interface in the free-board region. Additionally, the simulations for Run 16.6 with H=0.15 indicate a better match with experimental data than those computed with H=H*. As was mentioned earlier, this could possibly be the result of the uncertainties associated with the thermodynamic estimation of H given the complex

molecular composition of the FT wax. Nevertheless, the good agreement between data and simulations in terms of the peak arrival time as well as the overall shape of the tracer responses indicates that given reliable inputs, the gas mixing model developed in this study is capable of predicting the dynamics of scalar gas-liquid transport in bubble and slurry bubble column reactors.

# References

Anderson, K. G. and Rice, R.G., 1989, 'Local Turbulence Model for Predicting Circulation Rates in Bubble Column,' *AIChE J*., **35** (3), 514-518.

Bhatt, B. L., 1999, 'Liquid Phase Fischer-Tropsch (III & IV) Demonstration in the LaPorte Alternate Fuels Development Unit', *Topical report for Contract DE-FC22-95PC93052*.

Chen, J., P., Gupta, S., Degaleesan, M. H., Al-Dahhan, M. P., Dudukovic and B. A., Toseland, 1998, 'Gas holdup distributions in large-diameter bubble columns measured by computed tomography', *Flow Measurement and Instrumentation*, **9**(2), 91-101.

Degaleesan, S., M. P. Dudukovic', B. L. Bhatt and B. A. Toseland, 1996[a], 'Slurry Bubble Column Hydrodynamics: Tracer Studies of the LaPorte AFDU Reactor During Methanol Synthesis', *Fourth quarterly report for Contract DOE-FC 2295 PC 95051*.

Degaleesan, S., S. Roy, S. B. Kumar and M. P. Dudukovic', 1996[b], 'Liquid Backmixing Based on Convection and Turbulent Dispersion in Bubble Columns', *Chem. Eng. Sci.*, **51**, 1967-1976.

Degaleesan, S., 1997, *Fluid Dynamic Measurements and Modeling of Liquid Mixing in Bubble Columns*, D.Sc. Thesis, Washington University, Saint Louis, Missouri.

Gupta, P., B., Ong, M. H., Al-Dahhan, M. P., Dudukovic and B. A., Toseland, 2001[a], 'Hydrodynamics of churn turbulent bubble columns: gas-liquid recirculation and mechanistic modeling', *Catalysis Today*, **64**(3-4), 253-269.

Gupta, P., M. H., Al-Dahhan, M. P., Dudukovic and B. A., Toseland, 2001[b], 'Comparison of single- and two-bubble class gas-liquid recirculation models - application to pilot-plant radioactive tracer studies during methanol synthesis', *Chem. Eng. Sci.*, **56**(3), 1117-1125.

Gupta, P., 2002, *Churn-Turbulent Bubble Columns - Experiments and Modeling*, D.Sc. Thesis, Washington University, Saint Louis, Missouri.

Kemoun, A., B. C., Ong, P., Gupta, M. H., Al-Dahhan and M. P., Dudukovic', 2001, 'Gas Holdup in Bubble Columns at Elevated Pressure via Computed Tomography', *International Journal of Multiphase Flows*, **27**(5), 929-946.

Krishna, R., 2000, 'A scale-up strategy for a commercial scale bubble column slurry reactor for Fischer-Tropsch synthesis', *Oil & Gas Science and Technology – Rev. IFP*, **55**, 359-393.

Kumar, S. B., 1994, *Computed tomographic measurements of void fraction and modeling of the flow in bubble columns*, Ph.D. Thesis, Florida Atlantic University.

Kumar, S. B., Moslemian, D., and Dudukovic', M. P., 1995, A Gamma Ray Tomographic Scanner for Imaging Void Fraction Distribution in Bubble Columns, *Flow Meas. Instr.*, **6**(1), 61-73.

Ong, B. C., 1999, *Characterization of Gas-Liquid Churn-Turbulent Flow in Bubble Columns at Elevated Pressure*, D.Sc. Proposal, Washington University, Saint Louis, Missouri.

Sie, S. T. and R. Krishna, 1999, 'Fundamentals and Selection of Advanced Fischer-Tropsch Reactors', *Applied Catalysis A*, **186**, 55-70.

Tomiyama, A., I. Kataoka and T. Sakaguchi, 1995, 'Drag Coefficients of Bubbles (1st report, Drag Coefficients of a Single Bubble in a Stagnant Liquid)', *Trans. JSME Part B*, **61**(587), 2357-2364.

Ueyama, K. and T. Miyauchi, 1979, 'Properties of Recirculating Turbulent Two-Phase Flow in Gas Bubble Columns', *AIChE J*., **25** (2), 258-266.

Wender, I., 1996, 'Reactions of synthesis gas', *Fuel Processing Technology*, **48**, 189-297.

Wu, Y., B. C. Ong and M. H. Al-Dahhan, 2001, 'Predictions of radial gas holdup profiles in bubble column reactors,' *Chem. Eng. Sci*., **56**, 1207-1210.